学 位 論 文

Study of Solar Neutrinos at Super-Kamiokande

スーパー神岡実験における太陽ニュートリノの研究

平成9年3月博士（理学）申請

東京大学大学院理学系研究科

物理学専攻

小 汐 由 介

学 位 論 文

Study of Solar Neutrinos at Super-Kamiokande

スーパー神岡実験における太陽ニュートリノの研究

平成９年３月博士（理学）申請

東京大学大学院理学系研究科
物理学専攻
小汐 由介

Abstract

Super-Kamiokande started taking data on the 1st of April in 1996. The data used for the analysis of solar neutrinos in this paper was obtained from the 31st of May, 1996 to the 23rd of June, 1997 and the total live time is 297.4 days. The energy threshold is 6.5MeV and the fiducial volume is 22.5 ktons.

The observed ^{8}B solar neutrino flux in Super-Kamiokande is

$$2.42 \quad {}^{+0.06}_{-0.06}(stat.) \quad {}^{+0.13}_{-0.09}(sys.) \quad [\times 10^6/cm^2/sec].$$

The observed flux is smaller than the predicted by Bahcall and Pinsonneault (BP95). The ratio is

$$\frac{Data}{SSM(BP95)} = 0.365 \quad {}^{+0.010}_{-0.010}(stat.) \quad {}^{+0.019}_{-0.013}(sys.).$$

Comparing this deficit with the result of the Homestake experiment, the solar neutrino problem is difficult to explain by changing solar models but is more naturally explained by neutrino oscillations.

The solar neutrino flux of daytime and night-time agrees within the experimental errors and the result restricts the allowed neutrino oscillation parameters of the MSW effect. If we assume the large angle solutions to the solar neutrino problem, according to the MSW effect, neutrinos would regenerate through the earth. This analysis, which is independent of the solar models, excludes half of the large angle region which was obtained from the model-dependent analysis of the combined results from the past experiments. Within five years, the data sample from Super-Kamiokande should be large enough to study the whole large angle region.

Seasonal flux differences were not seen but currently, the statistical relevance of the data sample is insufficient. No energy distortion was found within the errors. For the analysis of the energy spectrum, more statistics and smaller systematic errors are needed.

Acknowledgments

First of all, I would like to express my sincere appreciation to my advisor, Prof. Yoichiro Suzuki. He gave me the chance to participate in this great experiment from the first stage of the construction and also supported me on many occasions during my graduate studies. His excellent guidance and suggestions helped me to understand what is important in experimental physics.

I would like to show my appreciation to the leader of the experiment, Prof. Y.Totsuka. His useful advice and continuous encouragement were helpful for this analysis.

This dissertation and the solar neutrino analysis were highly dependent on cooperation with the subgroup members (the low energy group). I am deeply indebted to Prof.M.Nakahata, Dr.K.Inoue, Dr.Y.Fukuda, Dr.Y.Takeuchi and Dr.K.Martens for giving me useful suggestions and for insightful discussions on various occasions. I also wish to thank the graduate students: Dr.T.Yamaguchi, Dr.H.Okazawa, H.Ishino, E.Ichihara, N.Sakurai and M.Nemoto, and the members in USA: Prof.B.Svoboda, Dr.J.Hill, Dr. M.Vagins, Dr.Z.Conner, Dr.M.Smy, Dr.B.K.Kim, R.Sanford and E.Blaufuss, for working together. Without their support and discussions with them, this dissertation would never have been completed.

I am thankful to all the collaborators of Super-Kamiokande for very useful suggestions. Especially, Prof.T.Kajita, Dr.Y.Itow, Dr.M.Miura, M.Shiozawa, T.Hayakawa, S.Kasuga, K.Ishihara, K.Okumura and J.Kameda who are all members of ICRR at Kamioka and with whom I often had useful discussions about the experiment, physics and so on. I must thank to Dr.J.Hill and C.Mauger for reading and checking this manuscript and for some useful comments.

Finally, I gratefully acknowledge the cooperation of Kamioka Mining and Smelting Company and financial support of the Japan Society for the Promotion of Science.

Contents

List of Figures

List of Tables

Chapter 1

Introduction

The origin of the energy in main sequence stars like the sun is the following nuclear fusion reaction,

$$4p \rightarrow \alpha + 2e^{+} + 2\nu_e + 26.73\text{MeV}. \tag{1.1}$$

In the center of the sun, reaction(1.1) is realized through the reaction chains : pp-chains and CNO cycle shown in Fig 1.1 and Fig 1.2. This process makes four protons form an α particle, two positrons, and two neutrinos and generates 27MeV of energy. The CNO cycle was first studied by H.A.Bethe in the 1930s[1]. The neutrino fluxes and spectra in these reactions are predicted by so called Standard Solar Models (SSMs)[2]. The SSMs have been improved over the past decades stimulated by neutrino measurements.

The neutrinos, generated in the center of the sun, go through the sun and appear at the surface of the sun immediately ($\sim$2sec) unlike the other particles like γ-rays. If the neutrinos from the sun are detected, it would be direct evidence that the nuclear fusion reaction is the origin of the sun's energy.

In the late 1960s, the first solar neutrino measurement was started by R.Davis and others in the Homestake Gold Mine at Lead, South Dakota, USA[3]. This experiment detected neutrinos by their interaction with ^{37}Cl, (ν_e+^{37}Cl $\rightarrow$^{37}Ar + e). The number of ^{37}Ar atoms generated by this reaction was counted. This kind of experiment is called a "radiochemical experiment". The flux of neutrinos at the earth can be predicted using SSM, however, the observed flux by the above measurement was significantly less than the expected flux[4].

The second solar neutrino experiment, Kamiokande-II, was operated more than twenty years later in the Kamioka mine in Gifu, Japan. Kamiokande was a water Cherenkov

experiment started in 1983 to search for nucleon decay. The detector was upgraded so that lower energy events could be detected. The solar neutrino measurement started in 1987. Solar neutrinos were detected by observing the Cherenkov light emitted by relativistic electrons produced by neutrino-electron scattering in the detector volume. The first result was reported in 1989, and the flux of measured neutrinos was significantly less than the expected value[5].

After that, two radiochemical experiments were operated in 1990s; those are GALLEX in the Gran Sasso Laboratory in Italy[6] and SAGE in the Baksan Neutrino observatory in Russia[7]. Those experiments detected neutrinos by their interaction with ^{71}Ga, (ν_e+^{71}Ga $\rightarrow$^{71}Ge +e). The number of ^{71}Ge atoms generated by this reaction was counted. An advantage of these experiments was the low energy threshold, so they could detect neutrinos from the basic pp reaction shown in Fig 1.1 (1). The ambiguity in the predicted solar neutrino flux is smaller than for other reactions. In these experiments a solar neutrino deficit was also observed.

The solar neutrino experiments up to now will be explained in Section 2.2 in detail. The newest results from them are summarized in Table 2.6. Compared to the prediction of SSMs, all of the independent solar neutrino measurements observed a solar neutrino deficit. This is called "the solar neutrino problem".

Various explanations of the solar neutrino problem have been proposed. Those approaches are mainly classified (1) the modification of the SSM, and (2) the not-yet resolved properties of neutrinos, especially the MSW effect in neutrino oscillations which will be explained in Section 2.4 in detail. The most effective method to solve the problem is an independent measurement on solar models, because SSMs have been improved but the flux calculation from SSMs has remained ambiguous. Super-Kamiokande, which started in 1996, can measure the energy spectrum and the time dependence of the solar neutrino flux, (day/night or seasonal differences). These are model independent measurements of solar neutrinos. These analyses were studied by Kamiokande[8], but the statistics were not sufficient to completely solve the problem. In Super-Kamiokande, the detector volume is more than ten times larger than that of Kamiokande - the fiducial volume is thirty times larger - so we can get extremely high statistics. Therefore, Super-Kamiokande is expected to provide definitive evidence of any possible new neutrino physics independent of the uncertainties in the solar models.

In this thesis, the first results of solar neutrino observation in Super-Kamiokande from 300days of data are reported in detail. The solar neutrino flux deficit and the daytime and night-time flux difference are discussed. Special emphasis is placed on the analysis of day/night flux difference which is independent of the solar models, sensitive to the MSW effect and has small systematic uncertainties.

In Chapter 2, the current status of the solar neutrino problem is explained. In Chapters 3 and 4, the experimental setup and the calibration are described. After the event reconstruction method and the Monte Carlo simulation are described in Chapter 5 and in Chapter 6, respectively, the method of data analysis and the results are described in Chapter 7. Finally, I discuss the results and make conclusions in Chapter 8.

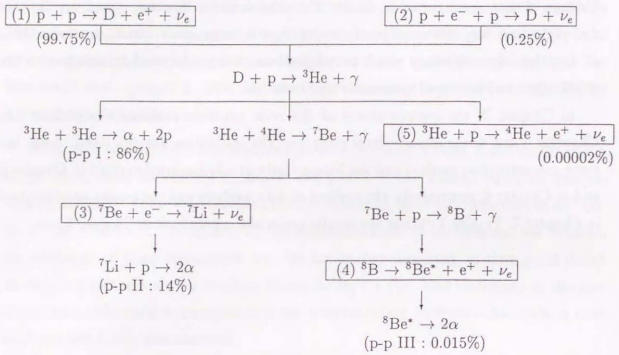

Figure 1.1: Proton-proton chain.

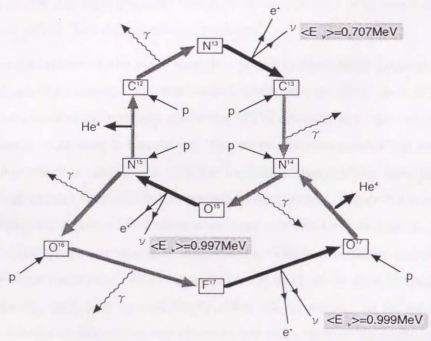

Figure 1.2: CNO cycle.

Chapter 2

The solar neutrino problem

2.1 The standard solar model

In the core of the sun, two reaction chains are occurring to realize the net reaction of Eq(1.1): the pp chain that starts with the direct fusion reaction of two protons; and the CNO cycle that is a circular chain with carbon, nitrogen, and oxygen as catalysts. These reactions are shown in Fig 1.1 and Fig 1.2, respectively. With the current knowledge of the temperature of the sun, the pp chain is believed to be dominant. The neutrinos from each reaction in the pp chain in Fig 1.1 are called: (1) pp neutrinos, (2) pep neutrinos, (3) ^{7}Be neutrinos, (4) ^{8}B neutrinos, and (5) hep neutrinos. As will be explained later, only ^{8}B neutrinos and hep neutrinos can be detected in Super-Kamiokande, but the expected rate from hep neutrinos is very small.

In constructing a solar model, some assumptions are used: the sun is in hydrostatic equilibrium, the transport of energy is caused by radiation or convection, the energy is generated by nuclear reactions. The basic equations representing the above conditions are solved numerically, and as the result of that calculation, we can determine the evolution and inner structure of the sun. The solar models calculated this way are called "Standard Solar Models" ([9][10][11]). In this section, I will mainly describe "BP95", which was published by Bahcall and Pinsonneault in 1995[10] among the several SSMs, and make a comparison with other SSMs will be also made.

The parameters listed in Table 2.1 were used for the input for the SSM calculation. In addition to that, knowledge of the solar radiative opacity is needed. The energy generated in the core is transported to the solar surface by photon radiation. The

photons are absorbed by the following physical processes: photon scattering on free electrons and inverse bremsstrahlung. The photon absorption coefficient, the radiative opacity, appears in the equation of energy transport. It affects the temperature gradient of the solar interior and therefore the neutrino production. The surface abundances of the elements of the sun are measured by an absorption spectrum. The recent measurements of them are consistent with the chemical composition in the meteorites. The effect of the back diffusion of heavy elements is included in BP95.

Parameter	Value
Photon luminosity	$3.844(1 \pm 0.004) \times 10^{33}$ erg/sec
Mass	1.99×10^{33} g
Radius	6.96×10^{10} cm
Age	$(4.57 \pm 0.02) \times 10^{9}$ year

Table 2.1: Some measured solar parameters[10].

Using the above input data, the basic equations are solved numerically. We can determine the solar interior as a function of time and space. Fig 2.1 shows the current temperature and density as a function of the distance from the center. The initial ratio of heavy elements relative to hydrogen is calculated to be 0.0245, and the depth of the convective zone, where the energy transport is caused by convection, is $R = 0.712 R_{\odot}$. ($R_{\odot}$ is the solar radius.) The results from the standard solar model can be checked by helioseismological measurements which provide the sound velocity profile in the solar interior and the depth of the convective zone[12]. Both of these from the SSM agree very well with the recent helioseismological measurements[13].

The solar neutrino flux depends on the solar core temperature as the following power laws[2],

$$\phi(\mathrm{pp}) \sim T_C^{-1.2}, \quad \phi(^7\mathrm{Be}) \sim T_C^{8}, \quad \phi(^8\mathrm{B}) \sim T_C^{18}. \tag{2.1}$$

The temperature is determined mainly by radiative opacity. If it changes, the flux also changes. Particularly, the ^{8}B neutrino flux is very sensitive to the temperature as shown in Eq(2.1). However, the calculated temperature constrained by the helioseismological measurements was in excellent agreement with SSMs[54]. This topic will be discussed in Chapter 8 in detail.

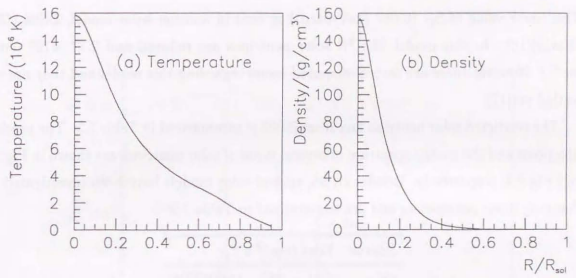

Figure 2.1: Temperature and Density profile in the sun as a function of the distance from the center of the sun.

For calculating the flux and the energy spectrum of solar neutrinos, the nuclear cross sections of the reactions shown in Fig 1.1 are needed. The cross section is conventionally written as follows:

$$\sigma(E) \equiv \frac{S(E)}{E} \exp(-2\pi\eta), \tag{2.2}$$

$$\eta = Z_1 Z_2 (e^2/\hbar v), \tag{2.3}$$

where v is the relative velocity between two particles with charges Z_1 and Z_2. Here, the term $\exp(-2\pi\eta)$ is called the Gamow penetration factor, which shows the effect of the Coulomb potential. $S(E)$, "the astrophysical S-factor", shows only the effect of the nuclear interaction. We need the value of $S(E)$ at zero energy for the calculation of solar neutrino flux and the spectrum. The S-factor of each of the reactions in Fig 1.1 is determined by experiment or calculation in the case of reactions via the weak interaction.

The most important S-factor for solar neutrinos detected in Super-Kamiokande is for the ^{7}Be(p,γ)^{8}B reaction, which is called S_{17}. It is directly proportional to the ^{8}B solar neutrino flux. The value used in BP95 is $S_{17}(0) = 0.0224(1 \pm 0.093)$ (keV·barn). The error comes from the uncertainty in the extrapolation of the cross section in the ^{7}Be(p,γ)^{8}B reaction to zero energy, which is caused by the existence of a resonance at 770keV[14]. Recently, the measurement using another method, which is the indirect measurement using the Coulomb dissociation reaction ^{208}Pb(^{8}B,^{7}Be+p)^{208}Pb, gives a lower value[15].

This lower value of S_{17} (0.017 (keV·barn)) is used in another solar model, DS94 (Dar-Shaviv)[16]. In this model, the ^{8}B solar neutrinos are reduced and 2.77 $\times 10^6$ (cm^{-2} sec^{-1}). However there are several disputed issues regarding this model and they are not settled yet[17].

The predicted solar neutrino flux from BP95 is summarized in Table 2.2. The production point and the energy spectrum of several types of solar neutrinos are shown in Fig 2.2 and Fig 2.3, respectively. Besides BP95, several solar models have been investigated by changing input parameters and are summarized in Table 2.3.

Source	Flux (cm^{-2} s^{-1})	
pp	5.91×10^{10}	$(1.00^{+0.01}_{-0.01})$
pep	1.40×10^{8}	$(1.00^{+0.01}_{-0.02})$
^{7}Be	5.15×10^{9}	$(1.00^{+0.06}_{-0.07})$
^{8}B	6.62×10^{6}	$(1.00^{+0.14}_{-0.17})$
^{13}N	6.18×10^{8}	$(1.00^{+0.17}_{-0.20})$
^{15}O	5.45×10^{8}	$(1.00^{+0.19}_{-0.22})$
^{17}F	6.48×10^{6}	$(1.00^{+0.15}_{-0.19})$

Table 2.2: Total flux of solar neutrinos predicted by BP95.

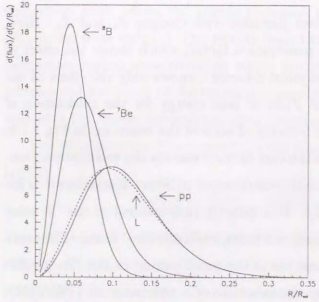

Figure 2.2: The production fraction of solar neutrinos as a function of solar radius. The fraction of solar luminosity is also shown by the dashed line.

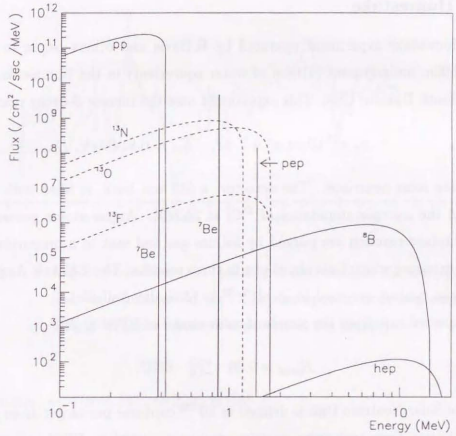

Figure 2.3: Energy spectrum of solar neutrinos.

SSM	S_{17} (keV·barn)	Predicted rate in Homestake	^{8}B neutrino flux (/cm^2/s)
BP92[9]	0.0224	8.0 ± 3.0 (SNU)	$5.69(1\pm0.43) \times 10^6$
TL93[11]	0.0225	6.4 ± 1.4	$(4.44\pm1.1) \times 10^6$
BP95[10]	0.0224	$9.3\ ^{+1.2}_{-1.4}$	$6.62\ ^{+0.93}_{-1.13} \times 10^6$

Table 2.3: Predicted solar neutrino rate in some SSMs.

2.2 Solar neutrino experiments

2.2.1 Homestake

The Homestake experiment operated by R.Davis and others began in 1968. It is located 1500m underground (4100m of water equivalent) in the Homestake Gold Mine at Lead, South Dakota, USA. This experiment uses the inverse β-decay reaction

$$\nu_e + {}^{37}\mathrm{Cl} \rightarrow e^- + {}^{37}\mathrm{Ar}, \quad E_{th} = 0.814\mathrm{MeV}, \tag{2.4}$$

for detecting solar neutrinos. The detector, a 615 ton tank, is filled with pure C_2Cl_4 liquid, and the isotopic abundance of ^{37}Cl is 24.23%. Argon atoms generated by the neutrino capture reaction are purged by helium gas and sent to a proportional counter after each exposure which lasts about one to three months. The 2.82 keV Auger electrons from electron capture are used to identify ^{37}Ar (35.0 day half-life).

The expected rate from the standard solar model of BP95 is [10]

$$R_{pred} = 9.30 \quad {}^{+1.2}_{-1.4} \quad \mathrm{SNU}. \tag{2.5}$$

"SNU", the Solar Neutrino Unit is defined as 10^{-36} captures per target atom per second. The contribution from each solar neutrino source predicted by BP95 is summarized in Table 2.4. The solar neutrinos detected by Homestake experiment are mainly ^{7}Be and ^{8}B neutrinos.

solar neutrino source	expected rate (SNU)
pp	0.00
pep	0.22
^{7}Be	1.24
^{8}B	7.36
^{13}N	0.11
^{15}O	0.37

Table 2.4: The expected flux of each solar neutrino source in the Homestake experiment.

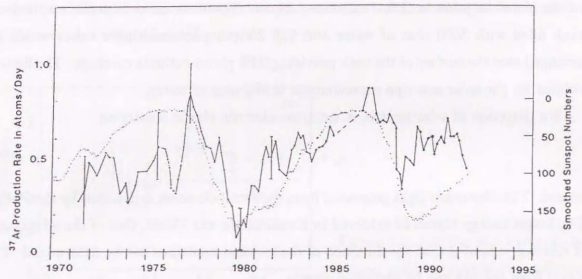

Figure 2.4: Argon production rate (solid line) and sunspot number (dotted line) as a function of time. The sunspot number is plotted inversely. (Higher numbers are lower in the graph.)

The counting rate from 1970 to 1995 is [18]

$$R_{obs} = 2.54 \pm 0.14 \pm 0.14 \quad \mathrm{SNU} \tag{2.6}$$

on average. Compared to the predicted value, the observed value is significantly smaller, and the ratio of data to SSM prediction is $0.273 \pm 0.015 \pm 0.015$.

An anti-correlation between solar activity and the solar neutrino flux is reported by the Homestake experiment. If the 11 year time variation is true, some new property of the neutrino must be considered, for example, finite neutrino mass or magnetic moment, since the neutrino production is expected to be stable on the scale of millions of years. Fig 2.4 shows the Argon production rate and sunspot numbers as a function of time[19]. From this figure, one may note that the anti-correlation is not seen after 1989. This time variation is not seen in Kamiokande as described in the next section.

2.2.2 Kamiokande

The solar neutrino measurement in Kamiokande started in January 1987 and ended in February 1995. Kamiokande is located 1000m underground (2700m of water equivalent)

in the Kamioka mine in Gifu Prefecture, Japan. The detector consists of a cylindrical tank filled with 3000 tons of water and 948 20-inch photomultiplier tubes which are arranged over the surface of the tank providing 20% photo-cathode coverage. The fiducial volume for the solar neutrino measurement is 680 tons of water.

For detection of solar neutrinos, neutrino-electron elastic scattering

$$\nu_e + e^- \rightarrow \nu_e + e^- \tag{2.7}$$

is used. The Cherenkov light generated from the recoil electrons is detected by the PMTs. The lowest energy threshold achieved in Kamiokande was 7MeV. One of the advantages of this experiment is that the direction of the incident neutrinos can be determined. The signal from the sun can be identified clearly.

The total effective live time of Kamiokande was 2079 days[20]. The ^{8}B solar neutrino flux observed is

$$\phi(^8\mathrm{B})_{obs} = 2.80 \pm 0.19(stat.) \pm 0.33(syst.) \quad [\times 10^6/cm^2/sec]. \tag{2.8}$$

The predicted total flux of ^{8}B solar neutrinos from BP95 is

$$\phi(^8\mathrm{B})_{pred} = 6.62 \quad {}^{+0.93}_{-1.13} \quad [\times 10^6/cm^2/sec], \tag{2.9}$$

which is also shown in Table 2.2. The observed value is less than that predicted, and the ratio of data to SSM prediction is $0.423 \pm 0.029 \pm 0.050$.

The period of the solar neutrino measurement in Kamiokande covered the entire period of solar cycle 22. Fig 2.5 shows (a) the solar neutrino flux and (b) sunspot numbers. From this figure, we cannot see any significant correlation within the experimental errors.

The advantage of the Kamiokande experiment is that the energy and the arrival time of the neutrino events are measured. Fig 2.6 shows the energy distribution of the recoil electrons (shown in the ratio of data to SSM prediction). No deviation is observed beyond the errors. Fig 2.7 shows the daytime and night-time solar neutrino flux. No difference between daytime and night-time is observed within the errors.

The shape of solar neutrino spectrum and the short time variation of the flux like daytime and night-time difference does not depend on the solar model. These measurements make it possible to do a solar model independent analysis. If a deviation from prediction is seen in one or both of these measurements, it reflects some new property of neutrinos. In Kamiokande, the statistics were insufficient for this analysis. However,

Super-Kamiokande, which is a larger detector with the same advantages, is expected to observe enough events for this analysis.

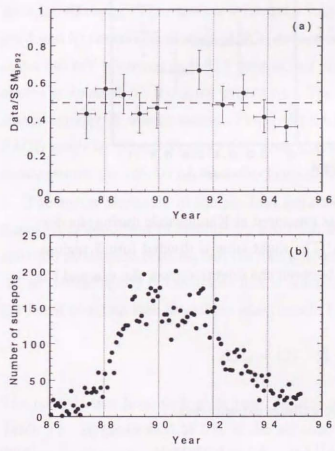

Figure 2.5: (a) The flux ratio of observed solar neutrinos to predicted flux for each 200 day period in Kamiokande; the dashed line is the average ratio for the entire period. (b) The sunspot numbers.

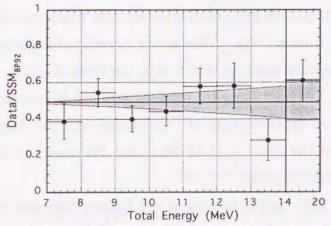

Figure 2.6: The recoil electron energy spectrum in Kamiokande. The flux ratio to SSM is shown. The hatched area shows the systematic uncertainty.

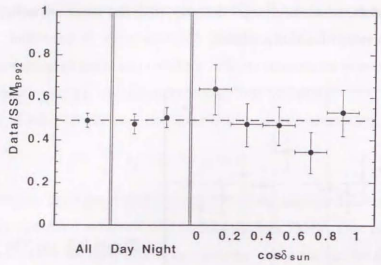

Figure 2.7: The solar neutrino flux measured at Kamiokande during the daytime and night-time. The night-time is divided into 5 regions. δ_{sun} shows the angle between the direction from the sun and the detector axis.

2.2.3 GALLEX and SAGE

The following reaction is used in two gallium experiments,

$$\nu_e + {}^{71}\mathrm{Ga} \rightarrow e^- + {}^{71}\mathrm{Ge}, \quad E_{th} = 0.233\mathrm{MeV}. \tag{2.10}$$

The GALLEX experiment started in 1991 and ended in 1997. It was located in the Gran Sasso Underground Laboratory in Italy, and the depth is 3300m of water equivalent. The ^{71}Ga target is used in the form of a 100-ton gallium chloride solution which contains 30.3 tons of natural gallium, thus 12 tons of ^{71}Ga. After about 3 weeks of exposure, the generated ^{71}Ge by the neutrino capture reaction, which is in the form of $GeCl_4$, is taken out by bubbling nitrogen gas. The final chemical product germane is sent to a proportional counter where the electron capture decay of ^{71}Ge occurs, and the Auger electrons are detected. The half life of the decay is 11.43 days, and the energy of the electron is 10.37keV (K-peak) or 1.17keV (L-peak).

The SAGE experiment started in 1990, and is located at the Baksan Neutrino observatory in Russia, and the depth is 4715m of water equivalent. As the ^{71}Ga target, 55 tons of gallium metal is used, and the temperature is raised to extract ^{71}Ge. (Its melting

temperature is 29.8°C.) The procedure after that is similar to GALLEX. After exposure, the extracted ^{71}Ge atoms are counted by proportional counters.

Both experiments performed "source experiments" in order to check the absolute detector efficiency. They used a man-made ^{51}Cr neutrino source. The source, which is produced by neutron irradiation of ^{50}Cr, decays via electron capture to ^{51}V, and primarily emits 746 keV neutrinos with 27.7 days of half life. The ^{71}Ge generated by ^{51}Cr neutrino source is counted by the same procedure. The ratio of produced ^{71}Ge to the known source activity, R, was measured. The GALLEX result is : $R = 0.93 \pm 0.08$[6], while the SAGE result is : $R = 0.95 \pm 0.12$[7], This kind of measurement is important because it demonstrates the validity of the radiochemical methods for solar neutrino detection.

The energy threshold in the reaction Eq(2.10) is low enough to observe the pp neutrinos. It is important to measure pp neutrinos because it is the most fundamental solar neutrino production reaction and the flux practically depends only on the solar luminosity, so the ambiguity of calculated flux is much smaller than for any of the others. The predicted counting rate in gallium experiments from BP95 is [10]

$$R_{pred} = 137 \ {}^{+8}_{-7} \ \mathrm{SNU}. \tag{2.11}$$

The contribution from each solar neutrino source predicted by BP95 is summarized in Table 2.5. It shows that 50.9% of the all solar neutrinos are from pp neutrinos in a gallium experiment.

solar neutrino source	expected rate (SNU)
pp	69.7
pep	3.0
^{7}Be	37.7
^{8}B	16.1
^{13}N	3.8
^{15}O	6.3

Table 2.5: The expected rate of each solar neutrino source in any gallium experiment.

The observed counting rate for each experiments is [21][7]

GALLEX

$$R_{obs} = 76.2 \pm 6.5(\text{stat.}) \pm 5(\text{syst.}) \quad \text{SNU} \tag{2.12}$$

SAGE

$$R_{obs} = 69 \pm 10(\text{stat.})^{+5}_{-7}(\text{syst.}) \quad \text{SNU} \tag{2.13}$$

The observed value is less than that predicted, and the ratio of data to SSM prediction is $0.556 \pm 0.047 \pm 0.036$ for GALLEX; $0.504 \pm 0.073^{+0.036}_{-0.051}$ for SAGE.

The time variation of the solar neutrino flux observed by the gallium experiments is checked. Fig 2.8 and Fig 2.9 shows the Ge production rate as a function of time. It has very large statistical errors in both experiments, however, from the analysis for time variation in GALLEX, they find no evidence for any time dependence[6].

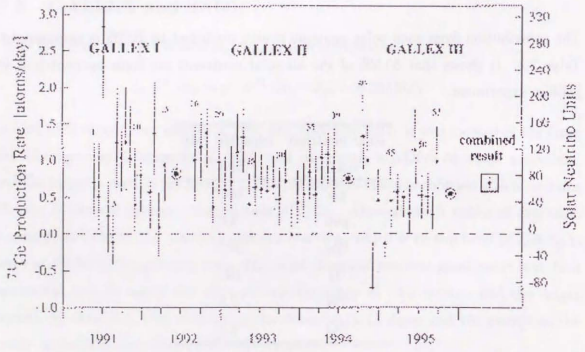

Figure 2.8: Ge production rate in each solar neutrino runs of GALLEX.

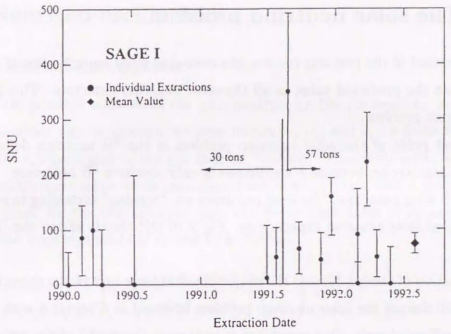

Figure 2.9: Ge production rate in SAGE as a function of time. The last point is the combined 1990-1992 data.

2.2.4 Summary of the results in solar neutrino experiments

In all the solar neutrino experiments up to now, the observed flux is significantly smaller than expected flux. Here, the deficit in the observed flux of solar neutrinos has been summarized.

Experiment	Detection method	Energy threshold	DATA/SSM (BP95)
Homestake	$^{37}\text{Cl}(\nu_e,e^-)^{37}\text{Ar}$	0.814MeV	$0.273 \pm 0.015 \pm 0.015$
Kamiokande	$\nu_e + e^- \to \nu_e + e^-$	7.0MeV	$0.423 \pm 0.029 \pm 0.050$
GALLEX	$^{71}\text{Ga}(\nu_e,e^-)^{71}\text{Ge}$	0.233MeV	$0.556 \pm 0.047 \pm 0.036$
SAGE			$0.504 \pm 0.073^{+0.036}_{-0.051}$

Table 2.6: The summary of several solar neutrino experiments and the result. The deficit from prediction value is also shown.

2.3 The solar neutrino problem

As described in the previous section, the measured solar neutrino flux is significantly smaller than the predicted value in all the solar neutrino detectors. This is called the solar neutrino problem.

The first point of the solar neutrino problem is the ^{8}B neutrino deficit from the result of Kamiokande, because Kamiokande is only sensitive ^{8}B neutrinos. Beyond the deficit of ^{8}B solar neutrinos, ^{7}Be solar neutrinos are "missing" according to results of the radiochemical solar neutrino experiments. Fig 2.10 [22] clearly shows the ^{7}Be neutrino deficit.

Explanation of this problem is the major physical issue and this is the subject of this thesis. I will discuss the solar neutrino problem in detail in Chapter 8 with new results from Super-Kamiokande. One possibility is to change the model of the solar interior to explain the problem; that is called an astrophysical solution. The other is to introduce massive neutrinos which can cause neutrino oscillations. The basic concepts and formula are described in the next section in detail.

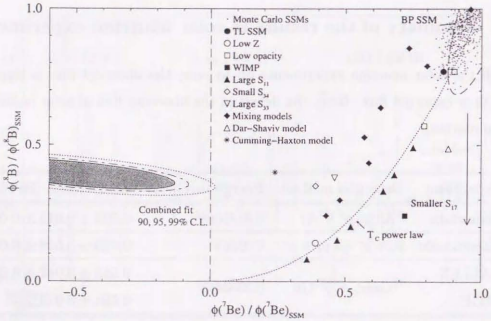

Figure 2.10: The constraint of ^{8}B/^{7}Be ratio from solar neutrino experiments at 90, 95, and 99% C.L. Also shown are the predicted from various SSMs.

2.4 Neutrino oscillations

2.4.1 General description

One of the possible solutions of the solar neutrino problem is neutrino oscillations. If neutrinos oscillate among different neutrino flavors, ν_e, ν_μ, and ν_τ, in flight from the sun to the earth, ν_e's generated in the sun become "missing" when they arrive at the earth. Neutrino oscillations occur when neutrinos have nonzero mass and a nonzero mixing angle[23]. Here, for the two neutrino case, the flavor eigenstates of ν_e and ν_μ are the mixing of the mass eigenstate of ν_1 and ν_2 as follows,

$$\begin{pmatrix} \nu_e \\ \nu_\mu \end{pmatrix} = \begin{pmatrix} \cos\theta & \sin\theta \\ -\sin\theta & \cos\theta \end{pmatrix} \begin{pmatrix} \nu_1 \\ \nu_2 \end{pmatrix} \equiv U \begin{pmatrix} \nu_1 \\ \nu_2 \end{pmatrix}, \tag{2.14}$$

where θ is the mixing angle. We solve the following equation to obtain the time evolution of each neutrino flavor;

$$i\frac{d}{dt}\begin{pmatrix} \nu_e \\ \nu_\mu \end{pmatrix} = H \begin{pmatrix} \nu_e \\ \nu_\mu \end{pmatrix}, \tag{2.15}$$

where H is Hamiltonian, diagonal for the mass eigenstate. In vacuum, the eigenvalue is as follows;

$$E_i = \sqrt{p^2 + m_i^2} \cong E + \frac{m_i^2}{2E} \quad (i = 1, 2), \tag{2.16}$$

where $m_{1,2}$ is the mass of the each mass eigenstate, p is the momentum, it is assumed that the two mass eigenstates have the same momentum and $m_{1,2} \ll E$. The time evolution of the mass eigenstates is represented as follows;

$$\begin{pmatrix} \nu_1(t) \\ \nu_2(t) \end{pmatrix} = \begin{pmatrix} e^{-iE_1 t} & 0 \\ 0 & e^{-iE_2 t} \end{pmatrix} \begin{pmatrix} \nu_1(0) \\ \nu_2(0) \end{pmatrix}. \tag{2.17}$$

From Eq(2.14) and (2.17), the time evolution of the flavor eigenstate becomes

$$\begin{pmatrix} \nu_e(t) \\ \nu_\mu(t) \end{pmatrix} = U \begin{pmatrix} e^{-iE_1 t} & 0 \\ 0 & e^{-iE_2 t} \end{pmatrix} U^{-1} \begin{pmatrix} \nu_e(0) \\ \nu_\mu(0) \end{pmatrix}. \tag{2.18}$$

The probability that the state which was generated as ν_e at $t = 0$ is ν_e or ν_μ at the time t is calculated from Eq(2.18) and (2.16) as follows;

$$P(\nu_e \to \nu_e; L) = 1 - \sin^2 2\theta \sin^2 \frac{\Delta m^2 L}{4E}$$

$$= 1 - \sin^2 2\theta \sin^2\left(1.27\frac{\Delta m^2(\mathrm{eV}^2)L(\mathrm{m})}{E(\mathrm{MeV})}\right), \quad (2.19)$$

$$P(\nu_e \to \nu_\mu; L) = \sin^2 2\theta \sin^2 \frac{\Delta m^2 L}{4E}$$
$$= \sin^2 2\theta \sin^2\left(1.27\frac{\Delta m^2(\mathrm{eV}^2)L(\mathrm{m})}{E(\mathrm{MeV})}\right), \quad (2.20)$$

where L is the distance traveled at the time t, and $\Delta m^2 = m_2^2 - m_1^2$ is the difference between the squared masses.

Neutrino oscillations in vacuum can be applied to the solar neutrino problem. In the case of $\Delta m^2/E \ll L$, the probability is averaged over time so that $P(\nu_e \to \nu_e) = 1 - \frac{1}{2}\sin^2 2\theta$[24]. Even in case of the full mixing ($\sin^2 2\theta = 1$), the probability becomes 0.5 and should be uniform in all the experiments. However, the results in Homestake and Kamiokande are much less than 0.5, and the probability obtained by all the experiments is not constant as shown in Table 2.6. It is difficult to solve the solar neutrino problem by the above explanation.

The vacuum oscillation parameters can be fine tuned by the results of solar neutrino deficit. The parameter ranges are calculated to be $\sin^2 2\theta > 0.7$ and $\Delta m^2 \sim 10^{-10}(\mathrm{eV}^2)$, which implies that the oscillation length is order of the distance from the sun to the earth. This fine-tuned solution is called "just-so" oscillations[25]. The effect could be seen by flux variation with the seasonal difference of the distance between the sun and the earth. Kamiokande and Super-Kamiokande are real time measurement of solar neutrinos. Therefore, the possible parameter region of just-so oscillation can be checked by the seasonal difference of the observed solar neutrino flux[26].

2.4.2 MSW effects

When neutrinos propagate in matter, they acquire additional potential energy from their forward scattering amplitude. The effect was first pointed out by Wolfenstein[27]. Mikheyev and Smirnov applied the effect to the solar neutrino problem and found the possibility of resonant enhancement of oscillations in the matter of the sun[28]. Therefore, it is called the MSW effect.

The potential of ν_e is different from the other types of neutrinos because of its charged current interaction of ν_e-e. This additional potential energy is calculated to be

$$V_e = \sqrt{2} G_F N_e, \quad (2.21)$$

where G_F is the Fermi coupling constant and N_e is the electron number density. In the case of neutrino propagation in matter, Eq(2.15) can be written

$$i\frac{d}{dt}\begin{pmatrix}\nu_e\\ \nu_\mu\end{pmatrix} = \left[U\begin{pmatrix}E_1 & 0\\ 0 & E_2\end{pmatrix}U^{-1} + \begin{pmatrix}V_e & 0\\ 0 & 0\end{pmatrix}\right]\begin{pmatrix}\nu_e\\ \nu_\mu\end{pmatrix}. \quad (2.22)$$

Taking out a common diagonal phase factor, the above equation can be rewritten

$$i\frac{d}{dt}\begin{pmatrix}\nu_e\\ \nu_\mu\end{pmatrix} = \begin{pmatrix}-\cos 2\theta \cdot \frac{\Delta m^2}{2E} + V_e & \frac{1}{2}\sin 2\theta \cdot \frac{\Delta m^2}{2E}\\ \frac{1}{2}\sin 2\theta \cdot \frac{\Delta m^2}{2E} & 0\end{pmatrix}\begin{pmatrix}\nu_e\\ \nu_\mu\end{pmatrix}. \quad (2.23)$$

Here, the eigenvector of the above matrix, which is analogous to vacuum oscillations, is defined as follows,

$$\begin{pmatrix}\nu_1^m\\ \nu_2^m\end{pmatrix} = \begin{pmatrix}\cos\theta_m & -\sin\theta_m\\ \sin\theta_m & \cos\theta_m\end{pmatrix}\begin{pmatrix}\nu_e\\ \nu_\mu\end{pmatrix}, \quad (2.24)$$

where ν_1^m and ν_2^m are considered as mass eigenstates of neutrinos in matter, and θ_m is the neutrino mixing angle in matter which is

$$\tan 2\theta_m = \frac{\sin 2\theta \cdot \frac{\Delta m^2}{2E}}{\cos 2\theta \cdot \frac{\Delta m^2}{2E} - V_e}. \quad (2.25)$$

The above two equations mean that if the following condition;

$$\cos 2\theta \cdot \frac{\Delta m^2}{2E} - V_e = 0 \quad (\theta_m = \frac{\pi}{4}), \quad (2.26)$$

is satisfied, oscillation can be amplified greatly even with a small vacuum mixing angle. This is the resonance condition. From Eq(2.24) and (2.25), we can qualitatively trace the state of $|\nu_1^m\rangle$ and $|\nu_2^m\rangle$ as follows;

$$\begin{cases} |\nu_2^m\rangle \sim |\nu_e\rangle & \text{at the very high density region,}\\ |\nu_2^m\rangle \sim (|\nu_e\rangle + |\nu_\mu\rangle)/\sqrt{2} & \text{at the resonance region,}\\ |\nu_2^m\rangle \sim \cos\theta|\nu_e\rangle + \sin\theta|\nu_\mu\rangle & \text{at the surface of the sun.}\end{cases}$$

If the resonance condition is met and the electron density varies slowly enough (adiabatic condition), the mass eigenstate $|\nu_2^m\rangle$, which is generated at the core of the sun, changes from $|\nu_e\rangle$ to $|\nu_\mu\rangle$ adiabatically, as is illustrated in Fig 2.11. The adiabatic condition is as follows;

$$\frac{\sin^2 2\theta}{\cos 2\theta} \cdot \frac{\Delta m^2}{E} \geq 2\pi\left(\frac{|dN_e/dr|}{N_e}\right)_{res}. \quad (2.27)$$

The survival probability of ν_e in the adiabatic condition is shown in Fig 2.12. The explanation of the solar neutrino problem using it is called "the adiabatic solution".

From Eq(2.26), the critical energy to have an MSW resonance for given parameters is

$$E_{crit} = \frac{\cos 2\theta \cdot \Delta m^2}{2\sqrt{2} G_F N_e^{max}} \tag{2.28}$$

where N_e^{max} is the maximum electron density in the sun. Therefore, the neutrino spectrum is suppressed in the region of energies higher than E_{crit}.

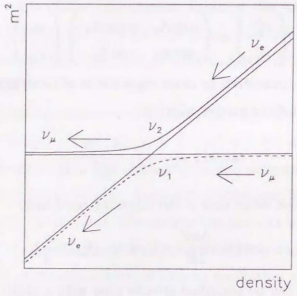

Figure 2.11: The MSW effect in the sun. The flavor eigenstate ν_e at the high density is approximately the same as the higher mass eigenstate ν_2. As the electron density decreases slowly, the flavor eigenstate remains close to ν_2. Therefore, the flavor eigenstate at the surface of the sun is close to ν_μ.

If the electron density varies rapidly, "level jumping" from $|\nu_2^m\rangle$ to $|\nu_1^m\rangle$ occurs. The jumping probability is[29]

$$P_{jump} = \exp\left[\frac{-\pi \Delta m^2 \sin^2 2\theta}{4E \cos 2\theta} \left(\frac{N_e}{|dN_e/dr|}\right)_{res}\right] \tag{2.29}$$

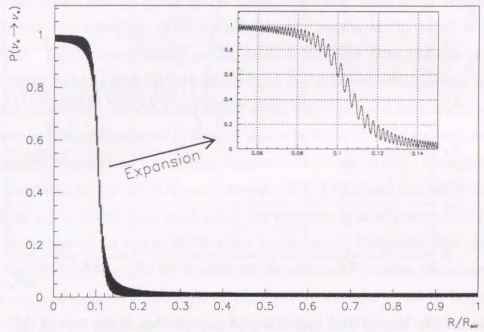

Figure 2.12: The survival probability of ν_e generated in the core of the sun at R=0, when $E/\Delta m^2 = 10^5$ and $\sin^2 2\theta = 0.01$.

As a result of level jumping, the conversion from $|\nu_e\rangle$ to $|\nu_\mu\rangle$ is suppressed. The explanation of the solar neutrino problem using this is called the "non-adiabatic solution". The behavior in this parameter region is shown in Fig 2.13.

From Eq(2.29), when the energy is higher, P_{jump} becomes higher and the probability of the conversion becomes smaller. Hence, the neutrino spectrum is suppressed in the lower energy region for the non-adiabatic condition.

The survival probability of ν_e as a function of energy in several MSW parameters, which include both the adiabatic region and the non-adiabatic region, are shown in Fig 2.14.

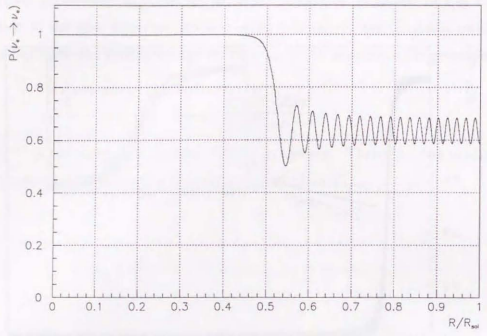

Figure 2.13: The survival probability of ν_e generated in the core of the sun, when $E/\Delta m^2 = 6 \times 10^6$ and $\sin^2 2\theta = 0.01$.

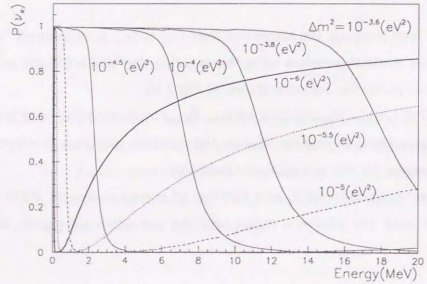

Figure 2.14: The survival probability of ν_e state by MSW effect as a function of Energy, when $\sin^2 2\theta = 0.01$ and for several values of Δm^2.

2.4.3 Regeneration in the earth

As in the above discussion, the MSW effect would also occur when neutrinos propagate through the earth[30]. The electron density profile of the earth is shown in Fig 2.15[31]. Because the density in the earth is different from the one of the sun, the survival probability of ν_e state in the earth is also different with the case in the sun. For typical parameters for which the MSW effect would cause a measurable day/night flux difference, the probability of ν_e state is shown in Fig 2.16. The example shows that the probability of detecting ν_e increases because of the regeneration through the earth from ν_μ generated by the oscillation in the sun. Fig 2.17 shows the MSW effect with and without going through the earth when the equation is solved numerically. We can also see the enhancement of the MSW effect by the earth. Therefore, the possible parameter region of MSW might be checked by the difference between the observed solar neutrino rate in the daytime and night-time. The flux at night would be larger than in the day. This kind of the observation can be performed only by real time measurements like Kamiokande or Super-Kamiokande. The analysis of the MSW effect in the earth is one of the main topics of this thesis.

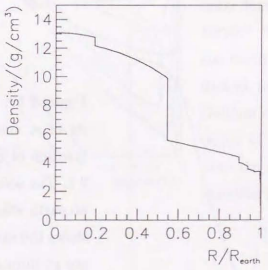

Figure 2.15: Density profile of the earth.

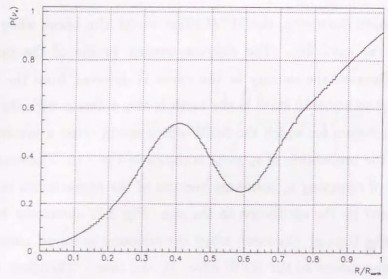

Figure 2.16: The probability of ν_e state regenerated in the earth, when $E/\Delta m^2 = 2 \times 10^6$, $\sin^2 2\theta = 0.1$, and neutrinos go through the core of the earth. The horizontal axis is the ratio of the path length to the diameter of the earth.

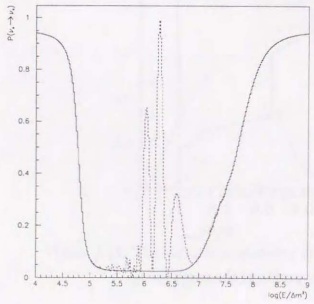

Figure 2.17: The expected probability of ν_e state by MSW effect as a function of $E/\Delta m^2$, when $\sin^2 2\theta = 0.1$. The solid line shows the case of no earth effect, and the dashed line shows the earth effect, where neutrinos go through the core of the earth.

2.4.4 The allowed parameter regions of the MSW effects

From the results of the past four solar neutrino experiments, the allowed region of the MSW effect has been studied and estimated. The combined result of all the experiments gives an allowed region is shown in Fig 2.18. As shown in the figure, two parameter regions are allowed: "the small angle solution" and "the large angle solution".

In the small angle solution, the deficit of neutrinos depends on its energy as shown in Fig 2.14. Around this parameter region, almost all ^{7}Be neutrinos and about 40% of ^{7}B neutrinos have converted such that the results of all the experiments are matched.

The large angle region is sensitive to the solar neutrino flux difference between daytime and night-time because the electron-neutrino regeneration through the earth occurs in this parameter region. From the result of the daytime and night-time flux difference in Kamiokande, the region shown in Fig 2.18 was excluded.

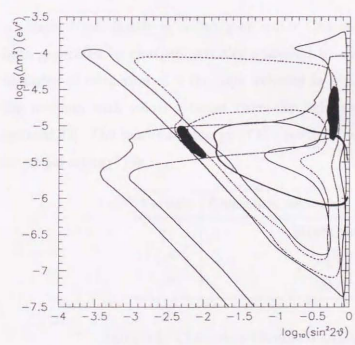

Figure 2.18: The contour of 95% C.L. allowed region of current four experiments. (filled area) The thin line shows the allowed region which is calculated by the deficit of the absolute solar neutrino flux in Kamiokande from BP95. The dotted line shows the result of Homestake and the dashed line shows the result of Gallium experiments. The inside region of a thick line is excluded from the result of day/night flux variation in Kamiokande.

Chapter 3

The Super-Kamiokande Detector

3.1 Detection method

3.1.1 Imaging water Cherenkov detector

Super-Kamiokande is an imaging water Cherenkov detector. It detects Cherenkov light generated by charged particles scattered by neutrinos in water. In a medium with an index of refraction of n the light velocity is c/n. When a charged particle traverses the medium with velocity larger than the light velocity, so called Cherenkov light is emitted[32]. The minimum energy of the particles with this velocity (called "Cherenkov threshold energy") is,

Particle	Cherenkov threshold in total Energy
$e^{\pm}$	0.768(MeV)
$\mu^{\pm}$	158.7
$\pi^{\pm}$	209.7

Table 3.1: Cherenkov threshold energy of various particle.

Cherenkov light is emitted in a cone of half angle θ from the direction of the particle track:

$$\cos\theta = \frac{1}{n\beta}, \tag{3.1}$$

where $\beta = v/c$, and θ is 42° for $\beta = 1.0$ in water. For example, the typical 20MeV electron simulation event is shown in an exploded view of the cylindrical water tank in

Fig 3.1.

The spectrum of the Cherenkov light as a function of the wavelength λ is

$$\frac{dN}{d\lambda} = \frac{2\pi\alpha x}{c}\left(1 - \frac{1}{n^2\beta^2}\right)\frac{1}{\lambda^2}, \tag{3.2}$$

where $\alpha \simeq 1/137$ (fine structure constant) and x is the length of the electron trajectory. A charged particle emits about 390 photons per 1cm of path length in the water in the wavelength region, 300nm $\sim$ 700nm, where the photo multiplier tubes are sensitive.

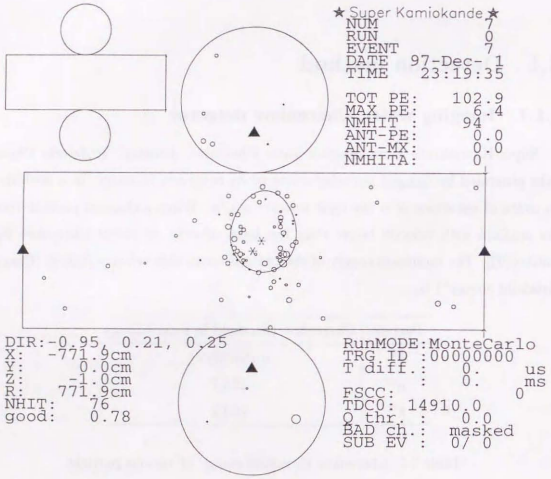

Figure 3.1: Typical expected event to be observed in Super-Kamiokande. This is a 20MeV electron simulation. The generated vertex and direction are (-800,0,0)cm and (-1,0,0), respectively.

3.1.2 Solar neutrino interactions in the detector

Solar neutrinos in Super-Kamiokande are measured through the following reaction;

$$\nu + e^- \rightarrow \nu + e^-. \tag{3.3}$$

The advantage of an experiment using this interaction is that we are able to obtain information on

(1) the direction of the incident neutrinos because the recoil electrons in Eq(3.3) are scattered to almost same direction as the neutrinos,

(2) the exact arrival time of the incident neutrinos and

(3) the energy distribution of the recoil electrons which reflects the energy spectrum of the incident neutrinos.

The cross section for this scattering can be calculated using standard electroweak theory, and the differential cross section is[33]

$$\frac{d\sigma}{dT_e} = \frac{G_F^2 m_e}{2\pi}\left[A_0 + B_0(1 - \frac{T_e}{E_\nu})^2 + C_0\frac{m_e}{E_\nu}\frac{T_e}{E_\nu}\right], \tag{3.4}$$

where G_F,m_e,E_ν,T_e are the Fermi coupling constant, the electron mass ,the incoming neutrino energy and the kinetic energy of the recoil electron, respectively. The parameters A_0, B_0 and C_0 are defined by

$$\begin{aligned} &A_0 = (g_V + g_A)^2, B_0 = (g_V - g_A)^2, C_0 = (g_A^2 - g_V^2), \\ &g_V = 2\sin^2\theta_W + \frac{1}{2}, \quad g_A = +\frac{1}{2} \quad \text{for} \quad (\nu_e, e), \\ &g_V = 2\sin^2\theta_W - \frac{1}{2}, \quad g_A = -\frac{1}{2} \quad \text{for} \quad (\nu_\mu, e)(\nu_\tau, e), \end{aligned}$$

where θ_W is the Weinberg angle. From Eq(3.4), the overall factor in the differential cross section is

$$\frac{G_F^2 m_e}{2\pi} = 4.31 \times 10^{-45} \quad (cm^2/\text{MeV}). \tag{3.5}$$

We also consider radiative corrections for the one-loop electroweak and QCD in the interaction Eq(3.3). A QED radiative correction is also considered. These corrections reduce the relative probability of observing recoil electrons by about 4% in our energy region for $\sin^2\theta_W = 0.2317$ [34].

The cross section as a function of neutrino energy including radiative corrections is shown in Fig 3.2. This cross section can be calculated by integrating Eq(3.4) between 0 and the maximum value, T_{max}, of the electron kinetic energy. Here T_e for given E_ν is limited by kinematics as follows,

$$T_{max} = \frac{E_\nu}{1 + m_e/2E_\nu}. \tag{3.6}$$

As shown in the figure, when E_ν is 10MeV, which is a typical energy of ^{8}B solar neutrinos, the cross section of ν-e scattering is:

$$\sigma_{total} = 8.96 \times 10^{-44} \quad (cm^2) \quad \text{for} \quad (\nu_e, e), \tag{3.7}$$

$$1.57 \times 10^{-44} \quad (cm^2) \quad \text{for} \quad (\nu_\mu, e)(\nu_\tau, e). \tag{3.8}$$

The differences of the cross section between ν_e and $\nu_{\mu,\tau}$ is because the scattering of $\nu_{\mu,\tau}$ on an electron can take place only through the neutral current interaction, while in case of ν_e, both neutral and charged current interactions take place. The $(\nu_{\mu,\tau}, e)$ cross section is approximately six times less than (ν_e, e) cross section.

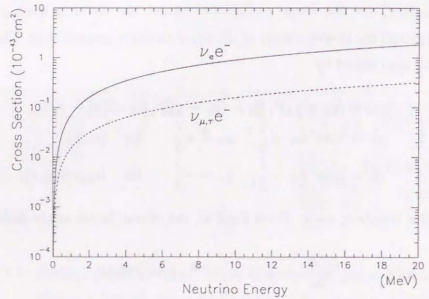

Figure 3.2: The cross section of the interaction for ν_e, ν_μ, ν_τ with electron as a function of neutrino energy.

The energy distribution of recoil electrons scattered by solar neutrinos is given by

$$F(T_e)dT_e = \left[\int_0^{E_{\nu,max}} \phi(E_\nu)\frac{d\sigma}{dT_e}dE_\nu\right] dT_e, \tag{3.9}$$

where $\phi(E_\nu)$ is the solar neutrino spectrum at earth (described in Section 2.1 in detail), and $E_{\nu,max}$ is the maximum energy of solar neutrinos. Fig 3.3 shows the energy distribution of recoil electrons with only ^{8}B and hep solar neutrinos considered.

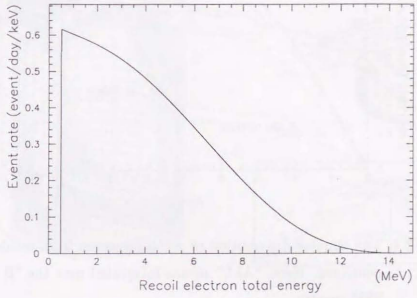

Figure 3.3: The spectrum of recoil electrons scattered off by ^{8}B and hep solar neutrinos.

The angle, θ, between the direction of a recoil electron and an incoming neutrino is given by

$$\cos\theta = \frac{1 + m_e/E_\nu}{\sqrt{1 + 2m_e/T_e}}. \tag{3.10}$$

The angular distribution of recoil electrons is given by

$$F(\theta)d\theta = \left[\int_0^{E_{\nu,max}} \phi(E_\nu)\frac{d\sigma}{dT_e}\frac{dT_e}{d\theta}dE_\nu\right] d\theta. \tag{3.11}$$

Fig 3.4 shows the angular distribution of recoil electrons with total energy greater than 0, 5, 7 and 10MeV. From this figure, the scattering angle is less than 20° if the threshold energy is greater than 5MeV. For a larger threshold energy, the angular distribution

becomes much more strongly forward peaked. The angular dispersion defined by the value which includes 68% of the distribution, is 12.3°, 9.1° and 5.7° for the electrons with total energy greater than 5, 7 and 10MeV, respectively

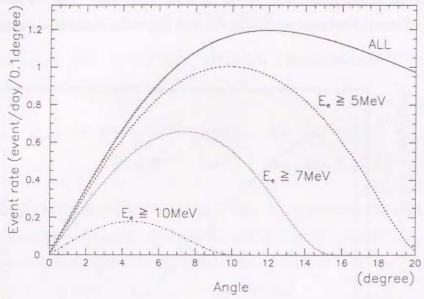

Figure 3.4: The angular distribution of recoil electrons from incident solar neutrinos. Here, "ALL" means integrated over the ^{8}B and hep SSM spectra.

3.2 Detector

3.2.1 Detector outline

The Super-Kamiokande detector consists of about 50000 tons of pure water filled in a cylindrical water tank (diameter 39.3m and height 41.4m), a water and air purification system, photomultiplier tubes (PMT), electronics and online data acquisition system, and offline computer facilities. Fig 3.5 shows a schematic view of the detector. It is located 1000m underground (2700m of water equivalent) in the Kamioka mine in Gifu Prefecture, Japan. Its latitude and longitude are 36° 25' N and 137°18' E, respectively.

The reason that the detector is underground is to shield against cosmic ray muons.

Compared to ground level, the intensity of muons is reduced by about 10^{-5} at the depth of the Super-Kamiokande detector. The muon rate in Super-Kamiokande is 1.88Hz. (See Section 7.2.3)

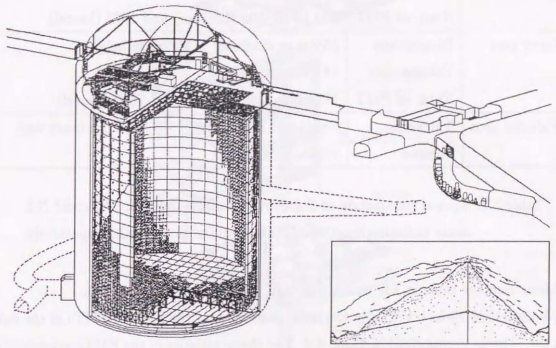

Figure 3.5: The detector appearance. Inset at bottom right shows the location within the mountain. (cutaway view)

The wall of the cave is covered by "Mineguard", a polyurethane material made by the Canadian company Urylon, which prohibits the radon emanating from the rock.

The water tank is made of stainless steel, and it is divided into an inner part and an outer part. These are summarized in Table 3.2. The reason for the division is mainly to identify remaining muon events from outside the tank and to reject gamma rays and neutrons from the rock.

The tank is sealed tightly to keep the mine's radon rich air from entering. Radon gas is the most serious background for the solar neutrino analysis as described in Section 7.2.7. The concentration of radon gas in the dome is about 1500 Bq/m^3 in summer time and 30 Bq/m^3 in winter time. This large difference is caused by the flow of air in the mine.

Tank	Dimensions	39.3m in diameter × 41.4m in height
	Volume	50 kton
Outer part	Thickness	2.6m (7.2 R.L. and 4.3 N.L.) on top and bottom
		2.75m (7.6 R.L. and 4.6 N.L.) on barrel
	Volume	32 kton
	Num. of PMT	302 (top), 308 (bottom) and 1275 (barrel)
Inner part	Dimensions	33.8m in diameter × 36.2m in height
	Volume	18 kton
	Num. of PMT	1748 (top and bottom) and 7650 (barrel)
Fiducial area	Thickness	2m (5.5 R.L. and 3.3 N.L.) from the inner wall
	Volume	22kton

Table 3.2: Several parameters of Super-Kamiokande detector. R.L and N.L mean radiation length and nuclear interaction length, respectively.

Air blows into the mine in the winter and out of the mine in the summer.

We use 11146 20-inch PMTs in the inner detector and 1885 8-inch PMTs in the outer detector. This is summarized in Table 3.2. The characteristics of the PMTs are described in Section 3.2.3.

In the inner detector, PMTs are placed at intervals of 70 cm, and the ratio of PMT area to all area (photo coverage) is 40.41%. The wall of the tank is covered with black polyethylene terephthalate sheets (called "black sheet") behind the inner PMTs.

In the outer detector, there are 2 outer PMTs in the region behind each 12 inner PMTs, and they face outward from the support structure. Around each outer PMT, there is wave length shifter to increase photo coverage. In order to increase the light detection efficiency, all surfaces of the outer detector are covered with white tyvek sheets with a reflectivity of above 80%.

The inner part and outer part are optically isolated using black sheets and tyvek sheets. There are complicated stainless steel frames for supporting the PMTs and so on in this optically insensitive region. The schematic view of these structures is shown in Fig 3.6.

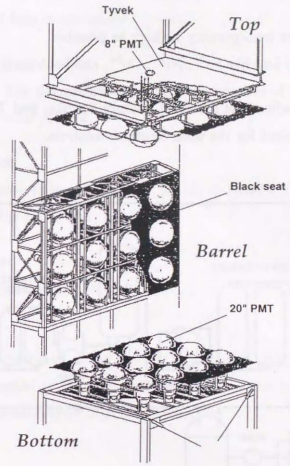

Figure 3.6: The schematic view of the frame which supports PMTs.

Construction started in 1991. First, the cavity was excavated until the middle of 1994. After that, water tank construction started, and it finished in the middle of 1995. From June of 1995, we installed PMTs and set the electronics system simultaneously. This continued until the end of 1995. Water filling was from January to March in 1996. After a 1 month test run, we started normal data taking from April 1st in 1996.

3.2.2 Water and air purification

Water purification system

In the Kamioka mine, there is clean water flowing near the detector and it can be used freely in large quantities. This water is circulated through the water purification

system. The purpose of this water purification system is:

1. To keep the water transparency as high as possible.
   Small dust, metal ions like Fe^{2+}, Ni^{2+}, Co^{2+}, and bacteria in the water are removed.

2. To remove the radioactive material, mainly Rn, Ra, and Th. Especially, radon is a serious background for the solar neutrino analysis.

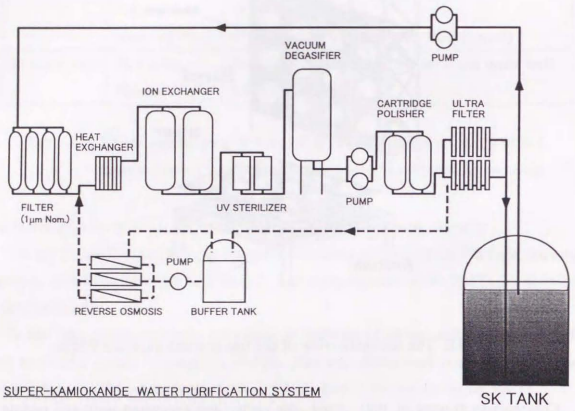

Figure 3.7: The water purification system.

Fig 3.7 shows the water purification system. The water purification system consists of the following components,

- 1 μm Filter
- Heat exchanger:
  The water temperature rises due to the heat generated by pumps and PMTs. The temperature is kept at around 14°C to suppress bacteria growth.

- Ion exchanger:
  To remove metal ions in the water.
- Ultra-Violet sterilizer:
  To kill bacteria. The documentation states the number of bacteria can be reduced to less than $10^3 \sim 10^4/100ml$.
- Vacuum degasifier:
  To remove gas resolved in the water. It is able to remove about 99% of the oxygen gas and 96% of the radon gas
- Cartridge polisher:
  This is a high performance ion exchanger.
- Ultra filter (UF)
  To remove small dust even of the order of nanometers. Fig 3.8 shows the resistance of the water sampled at the inlet and the outlet of the Ultra filter. This can be compared the chemical limit of 18.24 $M\Omega cm$.

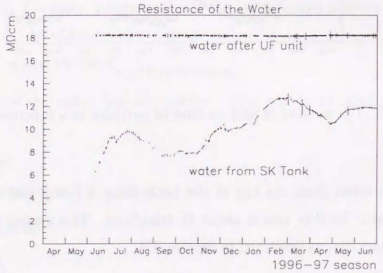

Figure 3.8: The resistance of the water sampled at inlet and outlet of the Ultra filter as a function of time.

Fig 3.9 shows the number of particles after the UF. After the Ultra filter, the water is returned to the detector. The UF removes 10% of the water passed through. That water is recirculated through the water purification system again via the following equipment, which is shown by the dashed line in Fig 3.7.

- Buffer tank
- Reverse osmosis

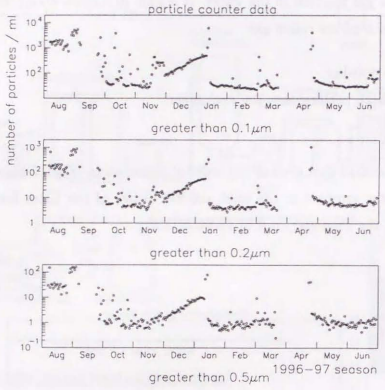

Figure 3.9: The number of various sizes of particles as a function of time.

The water is taken from the top of the tank using a pump and returned to the bottom of the tank. Its flow rate is about 50 tons/hour. This system keeps the water transparency above 70m as described in Section 4.4.

Radon free air system

There is ~60cm space between the surface of the water and the top of the water tank. Radon gas contaminated in the air in the gap could dissolve in the water. Radon free

air is sent to this region. The concentration of radon in the air is shown in Fig 3.10. It is of the order of $10 \sim 10^3$ Bq/m^3. It changes seasonally because the flow of air in the mine changes.

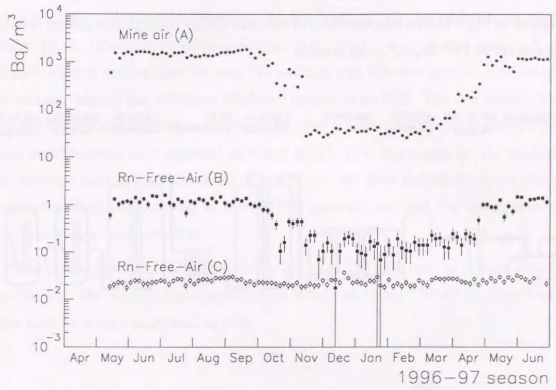

Figure 3.10: The radon concentration in the air of various position as a function of time.

Fig 3.11 shows the radon free air system. This system consists of the following components.

- Compressor:
  Air is compressed to $7.0 \sim 8.5$ atm.
- 0.3 μm air filter
- Buffer tank
- Air drier:
  To remove moisture in the gas to improve the efficiency of removing radon. This system can remove CO_2 in the gas as well.

- Carbon column:
  To remove radon gas.

- 0.1 μm and 0.01 μm air filter

As shown in Fig 3.10, the concentration of radon in the air through this system is reduced to the order of 10^{-2} Bq/m^3 in all seasons.

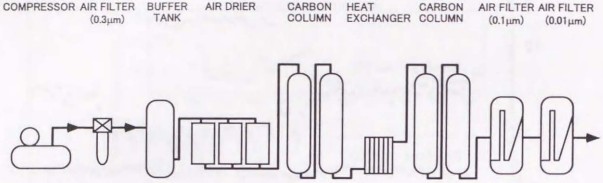

Figure 3.11: The radon free air system.

3.2.3 Photomultiplier tubes

The photomultiplier tubes (PMTs) used in the inner part of Super-Kamiokande are 20-inch diameter PMTs developed by Hamamatsu Photonics K.K. in cooperation with members of Kamiokande[35]. The PMTs used in Super-Kamiokande have some improvement over those used in Kamiokande. The size and shape of this PMT is shown in Fig 3.12. The photo-cathode is made of bialkali (Sb-K-Cs) that matches the wave length of Cherenkov light. The quantum efficiency (Q.E.) is shown in Fig 3.13. As can be seen from this figure, the value of Q.E. at the typical wave length of Cherenkov light (λ = 390nm) is 22%. A Venecian-blind type dynode is used for this PMT because of

its large photosensitive area. However, this large photosensitive area makes the transit time longer (about 100nsec at 1 photo electron (p.e.) light level) and transit time spread becomes worse. This type also has a smaller collection efficiency for secondary electrons compared to other types. The bleeder-chain was optimized in order to achieve good timing response and collection efficiency. As the result of this optimization, an 11-stage voltage divider (the ratio of voltage division is $8 : 3 : 1 : \cdots : 1$) was used, and three types of focusing mesh-plates between the cathode and the first dynode were adopted. The average value of the collection efficiency is more than 70%. The one photo electron peak can be seen clearly as shown in Fig 3.14. The transit time spread is about 2.2nsec. These measurements were reported in detail in[36]. It is important for the analysis of solar neutrino data to have the ability to see 1 p.e. and good timing resolution, because the number of photons arriving at the PMT is generally one and the timing resolution affects the vertex reconstruction.

If the geo-magnetic field is reduced to be less than 100 mG, the PMTs have a uniform response[36]. The residual geo-magnetic field is kept less than 100 mG in every position of the tank by using compensation coils.

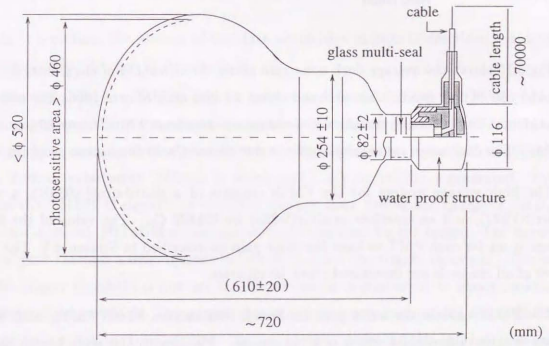

Figure 3.12: The schematic view of the PMT used in Super-Kamiokande.

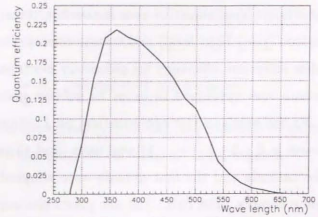

Figure 3.13: The quantum efficiency of the PMTs used in Super-Kamiokande as a function of the wave length of incident light.

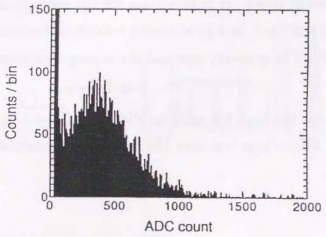

Figure 3.14: One photo electron peak of the PMTs used in Super-Kamiokande.

Fig 3.15 shows the average dark noise rate above the threshold of electronics for the first one year of operation. It is stable and about 3.1 kHz after May of 1996. The number of accidental hits caused by the dark noise is estimated about 2 hits in any 50nsec time window. The dark noise rate is considered in our Monte Carlo simulation program.

The high voltage system for the PMTs consists of a distributor(A933K), a controller(SY527), and an interface module(V288) by CAEN Co. The value of the high voltage is set for each PMT to have the same gain as described in Section 4.1. The HV values of all channels are monitored every 10 minutes.

The PMTs used in the outer part are 8-inch Hamamatsu R1408 PMTs, each with a wave length shifter plate which is 60cm square. Photons in the wave length range between 300 nm and 400nm are absorbed by the wave length shifter and about 55% of the photons isotropically re-emitted with a longer wave length.

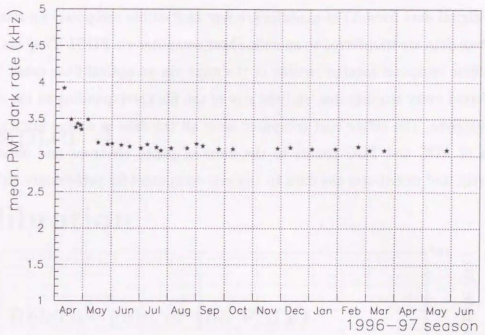

Figure 3.15: The dark noise rate of the PMT used in Super-Kamiokande as a function of time.

3.2.4 Electronics and Data acquisition

In this section, the essence of the data acquisition system is described. A detailed explanation can be seen in Appendix A.

The signal from a PMT is sent to a front end module called an "ATM" (Analog Timing Module)[37]. We use 934 ATM modules. The signals from 12 PMTs are handled in each ATM module. If the signal exceeds the threshold value, equivalent to about 0.32 p.e., a rectangular pulse (200nsec in width and 11mV in height) is generated. This is called the "HITSUM signal". In the ATM module, both timing and charge of the signal are also digitized. HITSUM signals are summed and used for the trigger. The summing signal goes through a discriminator which determines the trigger threshold. The value of the trigger threshold is now set to 320 mV which is equivalent to about 29 hits, or approximately 5∼6 MeV. This means that a global trigger is generated when 29 PMTs are hit in any 200nsec time window. The trigger rate is about 11Hz and has been stable during the course of the experiment as shown in Fig 3.16. The trigger efficiency will be described in Section 4.6.

The digital data from ATM modules are sent to 8 online computers for data acquisition. These data are transferred to an online host computer via FDDI. They are then sent to the offline computer located outside of the mine via an optical fiber cable. The data is transferred every ten minutes, and the size of the file corresponding to ten minutes is about 70MByte. The offline host computer saves all the data in a tape library, converts the data of ADC and TDC counts to the units of photo electrons and nano-seconds, respectively, and distributes the data to analysis computers for preliminary reduction.

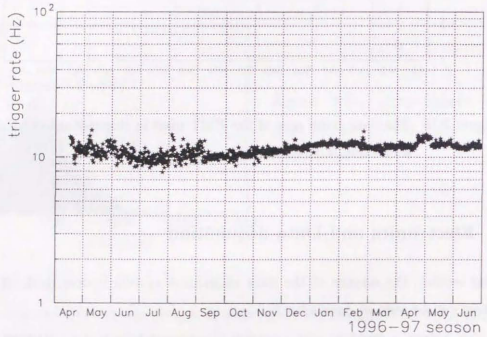

Figure 3.16: The trigger rate in Super-Kamiokande as a function of time.

Chapter 4

Calibration

4.1 Relative gain of the PMTs

The high voltage of each PMT is set in order to make the gain of each PMT the same. Each PMT has a standard high voltage value supplied from Hamamatsu Co. which was measured just after its production by using three methods: DC light source; Xe light source; single photo-electron distribution, However, we have re-calibrated the gain of all PMTs by ourselves in Super-Kamiokande, because a possible long term drift of the calibration system at Hamamatsu may have caused a systematic gain difference.

The relative gain was measured by the system shown in Fig 4.1. The light generated by a Xe-lamp is passed through an ultraviolet (U.V.) filter and injected into a scintillator ball via an optical fiber. The scintillator is an acrylic ball with BBOT scintillator (wavelength shifter) and MgO powder. This BBOT scintillator absorbs U.V. light and emits light the wavelength of which is near that of Cherenkov light. MgO powder is used for diffusing light in the ball. The intensity of the primary U.V. light is monitored by a monitoring system, and one of the outputs is used for a trigger, as shown in Fig 4.1.

In this system, the high voltage value of each PMT is set so that the corrected Q of each PMT is same as for all others. Here the "corrected Q" is pulse height corrected for light attenuation, acceptance, and uniformity of the scintillator ball. It is further normalized by Xe monitor pulse height. This measurement is done at various positions of the scintillator ball, and settings of the high voltage value. Fig 4.2 shows the corrected Q distribution of all PMTs after the adjustment. The relative gain spread is 7%. This remaining difference is later corrected in software.

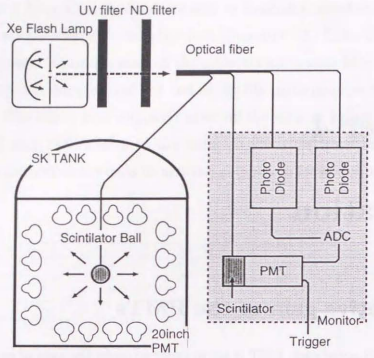

Figure 4.1: The relative gain measurement system.

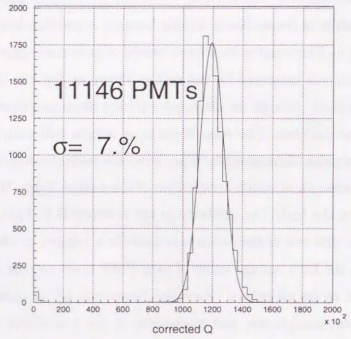

Figure 4.2: The corrected Q distribution of all PMTs in the relative gain calibration.

4.2 Single photo-electron distribution

In the previous section, only the relative gain of PMTs is discussed. In this section, we describe how to measure the absolute gain, particularly at single photo-electron level. We get only the charge information from the electronics output, in units of pico coulombs. We have to know how to get the number of photo-electron from this charge value. The single photo-electron distribution is used for this purpose.

The method is the same as the Nickel calibration, because the number of photon-electrons observed in each PMT is almost one in Nickel calibration. Fig 4.3 shows the charge distribution of each hit-PMT in units of pico coulombs. The mean value in this distribution is 2.055 pico coulomb, which is equivalent to single photo-electron.

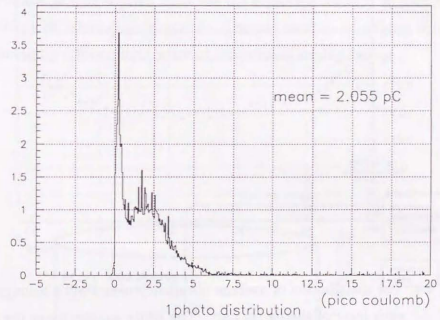

Figure 4.3: The charge distribution of each hit-PMT in Nickel calibration. The large spike near 0 is caused that the photoelectron go through the first dynode.

The "occupancy", which is hit rate of getting a single photo-electron signal as defined by Eq(B.2), is used in order to check the up-down symmetry of the detector. Fig 4.4 shows the distribution of average occupancy over PMTs belonging to each layer of the barrel part. From this figure, occupancy appears higher in the top and bottom layers than the

middle layers because of reflections from the surface of PMTs, however, the distribution is symmetric. Further, we checked that real data and Monte Carlo data were consistent. This result is crucial for analysis of the day-night effect of solar neutrinos.

Note that there are the layers with high occupancy in Fig 4.4. This occurs because PMTs belonging to these layers are made older than others and the quality is different. These PMTs have different single photo-electron detection efficiency even if the relative gain is adjusted to be same. The difference is 20% on average, and this is corrected for in energy determination as described in Section 5.3.

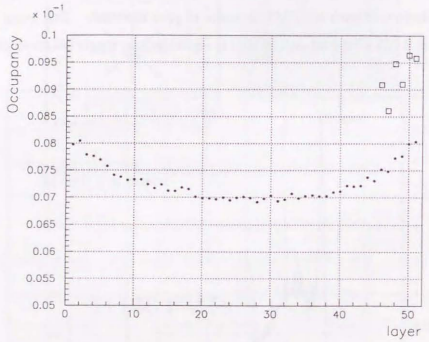

Figure 4.4: The distribution of average occupancy over PMTs belonging to each layer of the barrel part. The white squares show the older PMTs. Their quality is different with others.

4.3 Timing of PMTs

The relative timing of each hit-PMT is important for determination of the vertex. (ref. Section 5.1) This relative timing depends on observed charge because of the discriminator slewing effect. The timing difference caused by pulse height has to be measured precisely

in each PMT. The timing resolution also depends on pulse height and can be measured at the same time.

Fig 4.5 shows the system for measuring the relative timing of hit-PMTs. The N_2 laser light source can emit intense light of wavelength 337nm within a very short time (less than 3 nano seconds). The wavelength is converted to 384 nm which is near the Cherenkov light wavelength by a dye laser module. The light intensity is changed using an optical filter, and the measurement of PMT timing at various pulse heights is made. After going through the optical filter, the light is split into two, one goes to the diffuser ball in the water tank through an optical fiber, and the other signal is used for monitoring and making trigger signals. The schematic view of the diffuser ball is also shown in Fig 4.5. The diffuser tip which is located at the center of the ball is made from TiO_2 suspended in optical cement. Light emitted from the tip is further diffused by LUDOX, which is silica gel made with 20nm glass fragments. The combination of diffuser tip and LUDOX can make modestly diffused light without introducing timing spread.

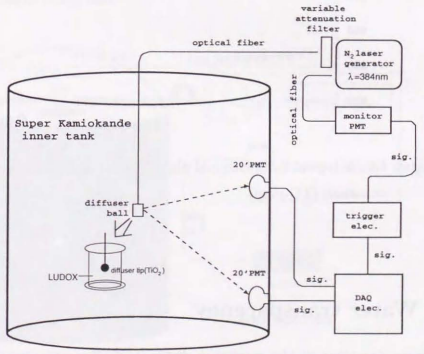

Figure 4.5: The system of the measurement of the relative timing of hit-PMT.

A typical 2-dimensional plot of timing and pulse height is shown in Fig 4.6, which we call a "TQ-map". Each PMT has its own TQ-map, because the character each PMT is unique. The vertical axis of this figure shows the hit timing; larger values indicate earlier hit timing. As shown in the figure, higher charge hits have earlier timing and better resolution. The typical timing resolution at the single p.e. level, which is important for the solar neutrino analysis, is 3nsec.

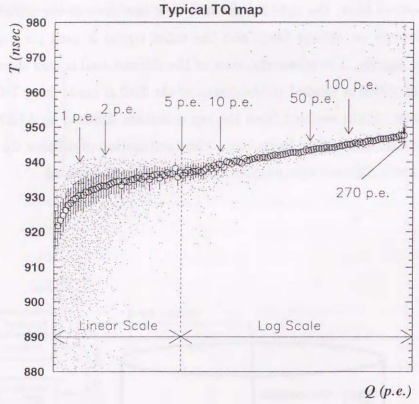

Figure 4.6: A typical 2-dimensional plot of timing and pulse height distribution. (TQ-map)

4.4 Water transparency

In Super-Kamiokande, the maximum distance of Cherenkov light traversal reaches 60m. The attenuation of Cherenkov light in water must be measured precisely, because the energy determination is affected by the water transparency.

The water transparency is measured two ways: direct measurement using laser and CCD camera, used for finding the absolute value of the water transparency; and using the decay electron events from stopping muons, or using penetrating muons observed in Super-Kamiokande to check the time variation of water transparency on an $\mathcal{O}$(1week) time scale.

4.4.1 Direct measurement

Fig 4.7 shows the system for the direct water transparency measurement, which consists of laser, diffuser ball, and CCD camera. For the light source, a N_2 laser and a dye module are used[38]. This dye module is able to produce mono chromatic laser output ranging from 337 nm to 600 nm. The light is split, one goes to a 2-inch PMT for monitoring the light intensity and another goes to an acrylic diffuser ball via an optical fiber. MgO is used for diffusing light in the ball. The light from the diffuser ball is received by a CCD camera, Fig 4.8 shows the picture of the light from the diffuser ball taken by CCD camera. The advantage of using CCD camera is that the effect of the scattering light is removed if only the region of the ball on a CCD view is used for measuring pulse height of the ball.

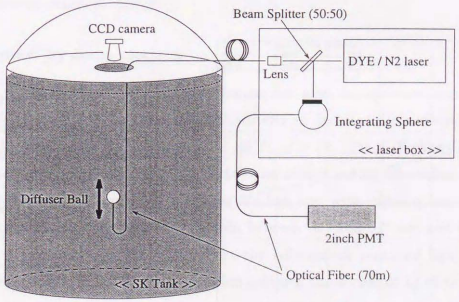

Figure 4.7: The system of the direct water transparency measurement.

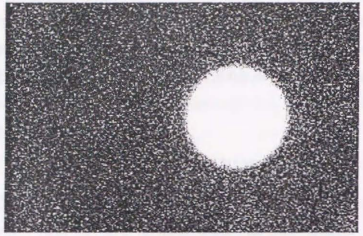

Figure 4.8: The picture of the light from the source taken by CCD camera.

The total number of received photos by CCD camera is measured in various positions, and it is normalized by the monitoring PMT data. For example, Fig 4.9 shows the result for 400nm wavelength light. The derived water transparency is 72.09m. This measurement is applied to various wavelength light, and the result is summarized in Table 4.1.

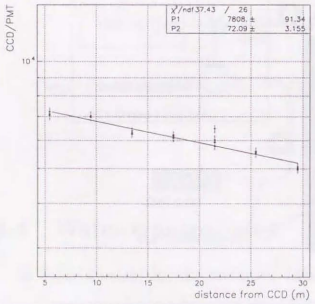

Figure 4.9: The result of the direct water transparency measurement. The horizontal axis is the distance between the diffuser ball and CCD camera, and the vertical axis is the normalized charge detected by CCD. The wavelength is 400nm.

Wavelength (nm)	Water transparency (m)
337	67.1
400	103.1
500	34.25
580	10.32

Table 4.1: The water transparency obtained by the direct measurement in various wavelength light.

4.4.2 Measurement using real data in Super-Kamiokande

There are two methods to measure the water transparency using real data in Super-Kamiokande; decay electron events from stopping muon and penetrating muon events. Unlike the direct measurement described above, we can not measure the water transparency dependent on light wave length in these methods. It can not directly be compared with the direct measurement, but these measurements can be done in real time and continuously. The value obtained by these methods is defined as the parameter which indicates the water condition. From these methods, the stability of water quality can be checked, and the time variation of water transparency measured by decay electron is used for determination of energy.

Measurement by decay electron

Decay electron events from stopping muons are used for the measurement of the average water transparency. The selection criteria of decay electron events is that it follow a stopping muon by 1.5~8μsec and its $N_{eff} > 70$. Fig 4.10 shows the typical event pattern of a decay electron event, and we can clearly see the Cherenkov ring. Only the hit-PMTs with hit timing in a 50nsec window and with opening angle from the reconstructed direction of the decay electron between 32° and 52° are used for getting the water transparency in order to neglect the reflected or scattered light. We can get the water transparency from the relation between the corrected Q of the each hit-PMT and the distance from the vertex to each hit-PMT. Here, corrected Q is a pulse height corrected for acceptance. (ref. Section 5.2) Fig 4.11 shows the relation, and the water transparency is calculated to 8518cm. Fig 4.12 shows the water transparency as

a function of time. After October in 1996, it is higher and higher, because we clean up the filter. This value is used for the correction of the energy reconstruction as described in Section 5.3.

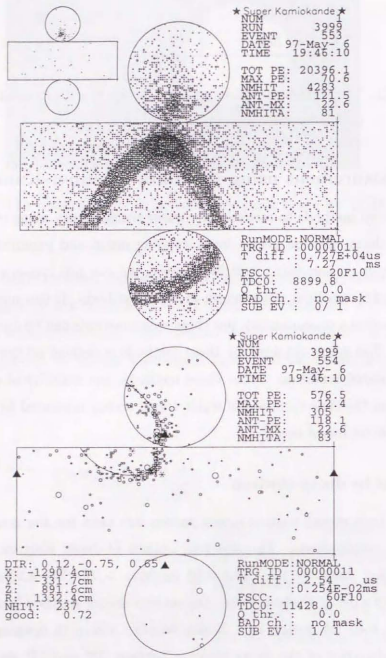

Figure 4.10: The typical event pattern of a parent muon event (upper), and decay electron event (lower). The time difference between these two events is 2.54μsec.

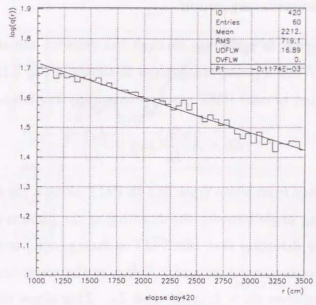

Figure 4.11: The relation between the corrected Q of the each hit-PMT and the distance from the vertex to each hit-PMT. The calculated water transparency is 8518cm. ($\chi^2/\nu = 108.584/49$)

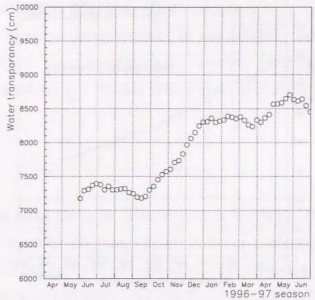

Figure 4.12: The water transparency as a function of time. The decay electron events from stopping muon are used for this calculation.

Measurement by penetrating muon

Cosmic ray muons which penetrate through the detector are also used to check the water transparency. When a penetrating muon as shown in Fig 5.13 traverses the detector, the charge observed in each PMT has approximately the following relation;

$$Q_i = A\frac{a(\theta_i)}{L_i}\exp\left[-\frac{L_i}{\lambda}\right], \tag{4.1}$$

where, L_i is the distance from muon track to i-th PMT along a ray at 42° from the muon track, θ_i is the opening angle between the direction of the photon on the surface of i-th PMT and the relative direction that this PMT is facing, $a(\theta_i)$ is the PMT acceptance function, A is a constant parameter, and λ indicates the water transparency. Fig 4.13 shows the relation between $Q_i \times L_i/a(\theta_i)$ and L_i. This slope in the figure indicates $1/\lambda$, and the water transparency is calculated to 5615cm. Fig 4.14 shows the water transparency as a function of time calculated by this method, and the time variation is consistent with the method using stopping muon event.

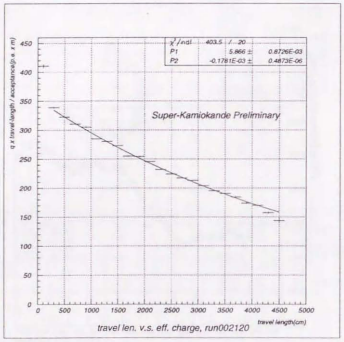

Figure 4.13: The relation between $Q_i \times L_i/a(\theta_i)$ and L_i. The calculated water transparency is 5615cm.

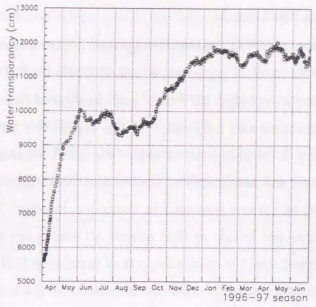

Figure 4.14: The water transparency as a function of time. The through going muon events are used for this calculation.

4.5 Energy calibration

Precise energy calibration is an important characteristic of Super-Kamiokande and is essential for solar neutrino measurement. In this section, three methods of energy calibration are described: using monoenergetic electrons from the LINAC; using a radioactive source for what we call "Nickel calibration"; and using decay electron events from stopping muons.

4.5.1 LINAC

For MSW analysis using the solar neutrino energy spectrum, the systematic error of absolute energy scale must be less than 1%.[39] In Super-Kamiokande, "LINAC calibration" is used for precise absolute energy calibration. The advantage of the LINAC is that the electron energy is monochromatic and can cover the full energy range relevant for solar neutrinos, 5~15MeV. Another advantage compared to the Nickel calibration, which is described in the next section, is that a direct calibration is available using electrons. Note that solar neutrinos are observed using electron signals from $\nu e \rightarrow \nu e$ scattering. In addition, more precise position calibration and direction calibration is available using a

collimated beam from the LINAC.

The schematic view of LINAC calibration system is shown in Fig 4.15. The LINAC, which was originally for medical purposes, is a model ML-15MIII from Mitsubishi. The beam pipe is evacuated to less than 10^{-4} torr, and the desired beam size and momentum are obtained by collimators and magnets. On the top of the Super-Kamiokande tank holes are welded every 2.1m along the -x-axis. We insert vertical beam pipe into the detector through these, and the length of the vertical beam pipe is variable, so we can do LINAC calibration at various positions in the inner detector. The beam intensity is adjusted to 0.1 electron per bunch so that almost all events are single electron events. The bunch width is 2μsec, and the maximum rate of bunches is 60Hz. Plastic scintillators acting as a trigger counter and veto counters are placed at the end of the beam pipe as shown in Fig 4.15.

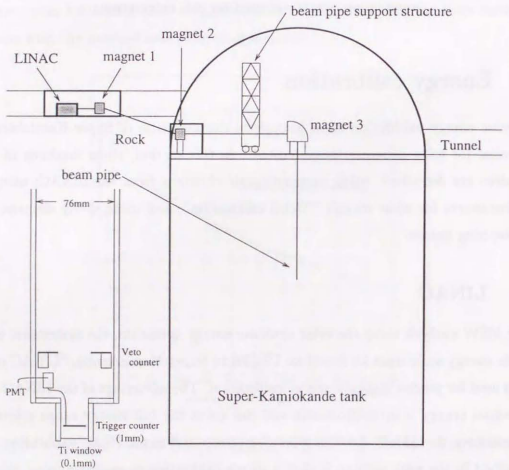

Figure 4.15: The schematic view of LINAC calibration system.

The energy of electrons which travel through the beam pipe is measured by a Ge detector[40]. For estimating the systematic error of the beam energy determination in the LINAC, the relation of observed momentum by Ge detector to the magnet field of magnet 1 is used, as shown in Fig 4.16. The observed momentum can be fitted by a line, and the deviation from that line is less than $\pm 0.3\%$.

The specifications of the LINAC are summarized in Table 4.2. The results of LINAC calibration, the position, angular, and energy calibrations, are described in Chapter 5.

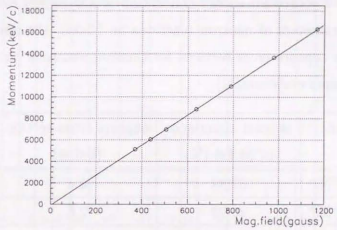

Figure 4.16: The relation of observed momentum by the Ge detector to the magnetic field of magnet 1. The observed momentum can be fitted by a line.

energy range	5~16MeV
intensity	~ 0.1 electrons / bunch
	(adjusted by the intensity of electron gun)
number of bunches	up to 60 bunches/sec, typical 10~30 bunches/sec
beam energy spread	$\leq \pm 0.3\%$
beam size	1~2cm at end cap
vacuum	$\sim 10^{-7}$ torr in accelerator tube
	$\leq 10^{-4}$ torr in beam pipe

Table 4.2: LINAC specification.

4.5.2 Nickel calibration

The very precise energy calibration is available in LINAC calibration, however, the setting of LINAC is a hard task and the beam direction is only downward. In addition to LINAC, we use Nickel calibration. It is so portable that we can do it easily. The direction of Nickel calibration is uniform. It is possible to reduce the several systematics using Nickel calibration in addition to LINAC.

The gamma rays emitted from the thermal neutron capture reaction on Nickel are used as a radioactive source for energy calibration of low energy event. Table 4.3 summarizes nuclear parameters of neutron reactions on Nickel, the natural abundances of Nickel isotopes, the capture cross sections for thermal neutrons, and the total released energy through gamma emissions[41].

Reaction	natural abundance of Nickel (%)	capture cross section (barns)	γ energy (MeV)
^{58}Ni(n,γ)^{59}Ni*	67.88	4.4	9.000
^{60}Ni(n,γ)^{61}Ni*	26.23	2.6	7.820
^{62}Ni(n,γ)^{63}Ni*	3.66	15	6.838
^{64}Ni(n,γ)^{65}Ni*	1.08	1.52	6.098

Table 4.3: The nuclear parameter concerned with the Nickel calibration.

Each isotope of the Ni(n,γ)Ni* reaction has many branches of transition. Fig 4.17 shows the transition diagram of the ^{58}Ni(n,γ)^{59}Ni* reaction[41][43]. As shown in the figure, 52.7% of the decays give an energy release via a single gamma ray of 9 MeV. The intensity of this gamma ray is the maximum of all branches of any isotope.

For the neutron source, ^{252}Cf fission is used. Its half life is 2.65 years, and it decays through α-decay (96.9%) and spontaneous fission (3.1%). When the fission occurs, an average of 3.76 neutrons with an average energy of about 2 MeV each and 10.8 γ rays with energy of about 8 MeV in total are emitted per one fission. The intensity of the ^{252}Cf source used is 1.7 μCi.

The reaction Ni(n,γ)Ni* occurs essentially only for thermal neutrons. The moderator for thermalizing a neutron with 2MeV energy is water. Neutrons are thermalized by protons in water through about 18 elastic scatterings on average. It takes a few micro

sec to thermalize. If the thermal neutron is captured by Nickel, a gamma ray with the energy as shown in Fig 4.17 is emitted. If the thermal neutron is not captured by Nickel, it is captured by a proton or oxygen in water. The cross section for these is 0.332barn and 0.178mbarn, respectively. The calculated mean capture time in water is 205μsec. The energy of emitted gamma rays via H(n,γ)D is 2.2 MeV, this gamma ray is the main background in this energy calibration.

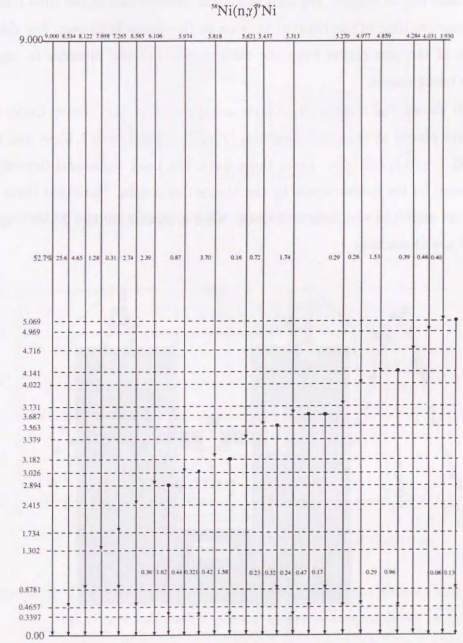

Figure 4.17: The transition diagram of the ^{58}Ni(n,γ)^{59}Ni* reaction.

Fig 4.18 shows the schematic view of the Nickel calibration system. As shown in the figure, the cylindrical polyethylene container, the diameter and height of which are each 20cm, is filled with 2.84kg Nickel wire of 0.1 mmϕ and pure water. At the center of the container, a proportional counter, in which the ^{252}Cf source is painted on an electrode, is located. The proportional counter is used for tagging fission and gives a precise trigger signal of the occurrence of a fission ("fission trigger"). The data is taken only for 500 μsec after each fission trigger. Fig 4.19 shows the distribution of the time intervals, and the mean capture time of the emitted neutron in this setup is 85μsec. For this analysis, subtraction of the late region from the early region is done in order to suppress the continuous backgrounds.

Fig 4.20 shows N_{50} distribution of the measured and the Monte Carlo data with the Ni source placed at the center position $(x, y, z) = (35.3, -70.7, 0)cm$ and at the top position $(35.3, -70.7, 1200)cm$. From these data, the peak value and resolution of N_{50} are reproduced for the measurement by the Monte Carlo data. Note that there is a bump in the low hit region in the measured data. This is caused by the 2.2MeV gamma ray from the H(n,γ)D reaction.

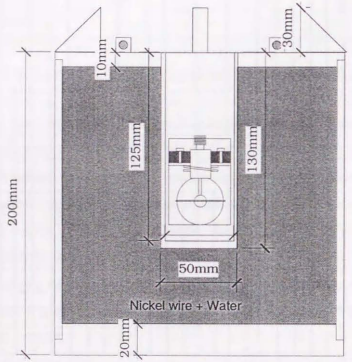

Figure 4.18: The schematic view of Nickel calibration system.

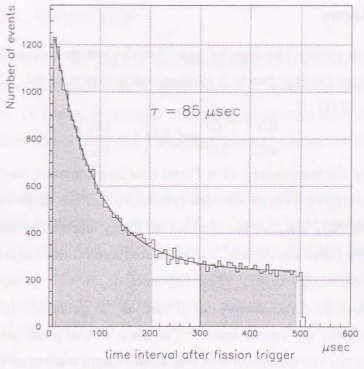

Figure 4.19: The distribution of the time intervals from the fission trigger.

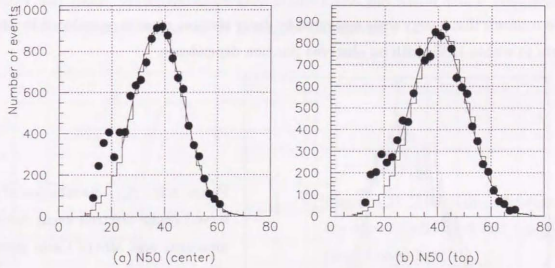

Figure 4.20: The N_{50} distribution of the measured and the Monte Carlo data of Nickel calibration placed at (a) center position $(x, y, z) = (35.3, -70.7, 0)cm$, and (b) top position $(35.3, -70.7, 1200)cm$.

4.5.3 μ-e decay

Decay electron events can also be used for the energy calibration. The selection criteria for the decay electron events is as described in Section 4.4.2. The energy spectrum of decay electron is[44]

$$\frac{dN}{dE_e} = \frac{G^2}{12\pi^3} m_\mu^2 E_e^2 \left(3 - \frac{4E_e}{m_\mu}\right), \tag{4.2}$$

where E_e is decay electron energy, G is Fermi coupling constant, and m_μ is muon mass. The maximum energy of a decay electron is 53MeV, and the mean energy is 37MeV.

Fig 4.21 shows N_{eff} distribution of observed decay electron events both in measurement and in Monte Carlo simulation. The measured and Monte Carlo data are consistent except for very low energy region. The difference of low energy region is caused by a gamma ray emission from radioactive nuclei such as ^{16}N generated by capture of a stopping μ^- to an oxygen nucleus in water. The ratio of the peak positions of the N_{eff} distributions between the measured and the Monte Carlo data is as follows,

$$\frac{\text{Monte Carlo}}{\text{measured data}} = \begin{cases} 0.982 \pm 0.002 & \text{22.5kton fiducial} \\ 0.984 \pm 0.002 & \text{11.7kton fiducial} \\ 0.986 \pm 0.003 & \text{distance from the wall is } 2 \sim 5\text{m}. \end{cases}$$

This confirms that energy scale measured by decay electron event is reproduced by Monte Carlo to within 1.2%, with no observed position dependence.

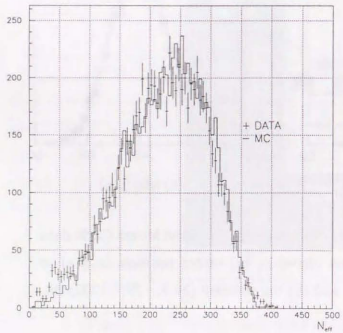

Figure 4.21: N_{eff} distribution of observed decay electron event both in measured and Monte Carlo simulation.

4.6 Trigger efficiency

The trigger efficiency of the Super-Kamiokande detector is also important for getting a precise solar neutrino flux. Note that "trigger efficiency" means the detection efficiency in each energy region. Of course, because of the energy resolution, the analysis efficiency is 50% at the threshold energy, however, "trigger efficiency" means the detection efficiency hereafter.

For the measurement of the trigger efficiency, Nickel calibration is used. In addition to the normal trigger mentioned as Section 3.2.4, the special trigger whose threshold is very low (150 mV) is applied at the same time. This is called the "super low trigger". The trigger efficiency is defined by the ratio at the each energy point of events passing the normal trigger threshold to those triggering the super low trigger. Fig 4.22 shows the trigger efficiency at the center and top position. The N_{eff} at which the trigger efficiency is 50 % at the center position is 38 hits, which corresponds to 5.8MeV.

As mentioned later (Chapter 7), the energy threshold for solar neutrino analysis is 6.5MeV. The trigger efficiency above 7MeV is almost 100% at all positions in the fiducial volume both Monte Carlo and Nickel data. However, in the energy region between 6.5MeV and 7MeV, the difference between Monte Carlo and Nickel data is calculated to 1.2%. This difference is corrected for in flux measurements.

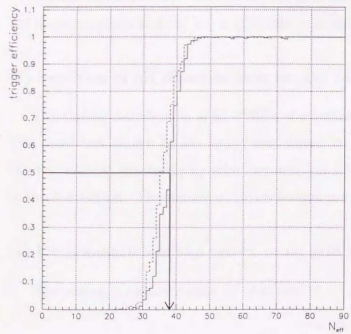

Figure 4.22: The trigger efficiency at the center (solid line) and top position (dashed line).

Chapter 5

Event reconstruction method

5.1 Vertex reconstruction

The vertex is determined by using timing information of the Cherenkov photons detected by PMTs. The energy of events important to analysis is around 10MeV. We call this class of event "low energy events". Fig 3.1 shows the event pattern of a typical low energy event. The track length of these events is 10cm at most. Compared to the vertex resolution of 90cm at 10MeV, the track length is negligible and the vertex can be assumed to be a point.

Vertex reconstruction of the event has 2 steps: (1) select hit channels to be used for the reconstruction and (2) use a grid search method to find the vertex.

(1) Selection of hit channels used for the vertex reconstruction

The timing distribution of hit-PMTs of a typical low energy event is shown in Fig 5.1. The noise hits shown in the figure are caused by PMT dark current. These noise hits can be removed effectively by selecting only hit-PMTs in a narrow timing window to use in reconstruction. The details of this selection are described in Appendix B.1.

(2) Determination of the vertex using grid search method

The vertex is reconstructed by minimizing

$$T^2 = \sum_{i=1}^{N_{hit}} t_{res,i}^2 \tag{5.1}$$

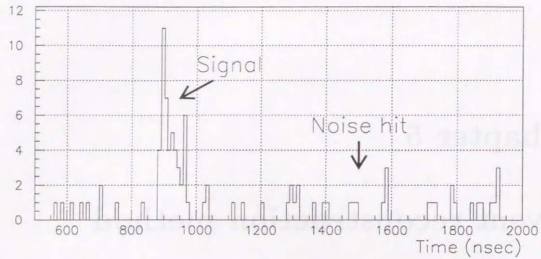

Figure 5.1: The timing distribution of hit-PMTs in one event. The time, which is horizontal axis, is the relative timing of the each hit-PMT obtained from ATM data.

In this equation, N_{hit} is number of hit-PMTs, and $t_{res,i}$ is the residual time of i-th hit-PMT after subtracting the time of flight from the arrival time of the photon:

$$t_{res,i} = t_i^0 - (n/c) \times \sqrt{(x-x_i)^2 + (y-y_i)^2 + (z-z_i)^2} - t_c, \tag{5.2}$$

where

t_i^0 : arrival time of the photon in the i-th PMT,
n : index of water,
c : light speed in vacuum,
(x, y, z) : vertex position,
(x_i, y_i, z_i) : position of the i-th PMT,
t_c : the central value of t_i,

and the detector coordinate used in Super-Kamiokande is defined shown in Fig 5.2. We define the following value, "*goodness*" for vertex reconstruction,

$$goodness = \frac{1}{\sum \frac{1}{\sigma_i^2}} \times \sum_i \frac{1}{\sigma_i^2} \exp\left[-\frac{t_{res,i}^2}{2\sigma_i^2}\right], \tag{5.3}$$

where σ_i is timing resolution of the PMT (here 5nsec). The range of this *goodness* is from 0 to 1. A grid search method is used in order to find the vertex where the *goodness*

becomes maximum. The search starts on a coarse grid covering the whole inner detector (but 1m away from the surface of the PMTs):

8 divisions in X,Y axis (the step size is 397.5 cm),
9 divisions in Z axis (the step size is 380.0 cm).

The resultant position at each iteration is used as the initial value for the next, more precise step. The step size is 150cm at first and goes down to 5cm finally.

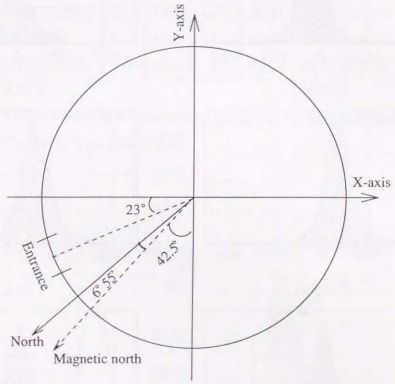

Figure 5.2: Coordinate of the Super-Kamiokande detector.

The quality of this vertex reconstruction method was estimated by the Nickel and LINAC data. Fig 5.3 shows the reconstructed vertex distribution for the Nickel source placed close to the middle of the detector. Table 5.1 shows the vertex shift and resolution at various positions. The vertex shift is defined the distance between the Nickel position and the mean value of the distribution shown in Fig 5.4 (a). The vertex resolution is defined as the sigma of the distribution. A systematic vertex shift may be present, but is 16cm at most.

For these figure, the vertex position and resolution are well reproduced by the Monte Carlo calculation.

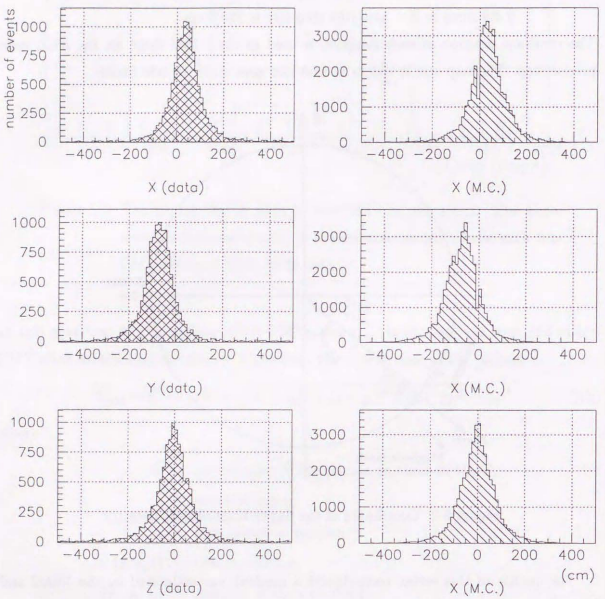

Figure 5.3: The reconstructed vertex distribution for the Nickel source placed at $(x, y, z) = (35.3, -70.7, 0.0)cm$. The left 3 figures show the real data and the right three are Monte Carlo.

Position (x,y,z)	$\triangle x$	$\triangle y$	$\triangle z$	σ_x	σ_y	σ_z	σ_r
(35.3,-70.7,-1200)	-0.3	-2.7	-3.0	47.98	49.28	47.66	115.8
(35.3,-70.7,0)	0.7	-0.5	-1.9	47.11	49.23	52.80	114.2
(35.3,-70.7,1200)	-1.0	-0.7	-1.0	46.87	48.17	47.88	113.6
(35.3,-70.7,1600)	-0.6	-2.8	-10.0	46.98	46.40	44.67	111.6
(35.3,-1201,-1200)	-3.4	7.0	-7.0	46.91	47.65	47.40	110.7
(35.3,-1201,0)	-1.1	16.0	-1.1	42.70	43.16	50.08	113.0
(35.3,-1201,1200)	0.6	10.0	2.0	43.74	44.92	48.74	109.4

Table 5.1: The vertex shift and resolution at the various positions of Nickel source. The unit is (cm).

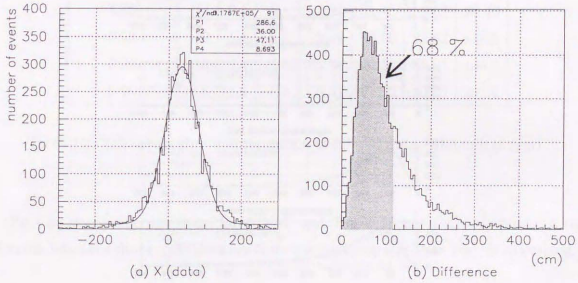

Figure 5.4: (a) The reconstructed X distribution of Nickel data placed at x=35.3cm. (b) The distribution of the distance between the Nickel position and the reconstructed position. The vertex resolution is defined by the value which includes 68%.

LINAC calibration was performed at 2 pipe positions and 7 beam energy points. Fig 5.5 shows the distance between the pipe position and the reconstructed vertex. This figure shows that the distribution of the data is reproduced well by the Monte Carlo calculation. Table 5.2 shows the vertex shift and resolution.

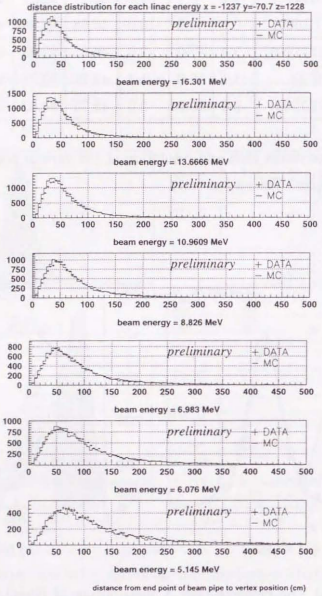

Figure 5.5: The distribution of the distance between the pipe position and the reconstructed vertex at 7 energy points in LINAC data and Monte Carlo. The position of the end point of the beam pipe is (-1237,-70.7,1228)cm.

Position:(-1237,-70.7,1228)cm

Energy(MeV)	$\triangle x$	$\triangle y$	$\triangle z$	σ_x	σ_y	σ_z	σ_r
16.3	14	2.1	-6	22.38	20.18	42.56	59.89
13.7	14	1.6	-4	23.55	21.91	43.83	63.24
11.0	12	1.8	-3	27.73	25.86	49.14	70.49
8.83	12	2.7	-1	33.16	31.07	56.39	83.02
6.98	9	1.5	-1	41.73	37.96	69.01	104.6
6.08	8	3.3	0	47.12	43.87	80.76	124.7
5.15	5	2.1	2	56.66	51.19	102.2	161.5

Position:(-1237,-70.7,27)cm

Energy(MeV)	$\triangle x$	$\triangle y$	$\triangle z$	σ_x	σ_y	σ_z	σ_r
16.3	16	1.7	-8.1	21.31	20.88	43.96	62.22
13.7	15	0.4	-6.7	23.18	22.95	46.84	66.28
11.0	15	1.0	-5.5	27.12	26.30	52.46	75.81
8.83	14	0.7	-5.8	32.27	31.75	59.89	90.46
6.98	12	1.1	-5.2	39.42	39.03	72.62	116.8
6.08	10	2.4	-5.3	45.34	44.24	85.71	144.8
5.15	8	1.9	-5.5	55.33	51.60	105.3	207.6

Table 5.2: The vertex shift and resolution of LINAC data. The unit is (cm).

Finally, the vertex resolution for 10MeV and 7MeV Monte Carlo electrons in the 22.5kton fiducial volume, (the distance from the wall is grater than 2m), is calculated.

Energy(MeV)	σ_x	σ_y	σ_z	σ_r
10.0	43.12	42.31	43.71	88.22
7.0	54.63	53.52	53.93	117.6

Table 5.3: The vertex resolution in Monte Carlo. The unit is (cm).

5.2 Directional reconstruction

Directional reconstruction is very important for solar neutrino analysis because the recoil electron keeps the direction of the solar neutrino. This characteristic is used to extract the solar neutrino signal in Super-Kamiokande. A maximum likelihood method using the Cherenkov ring pattern is adopted to determine the direction. The likelihood function is

$$L(\vec{d}) \equiv \sum_i \log(f(\cos\theta_{dir}))_i \times \frac{\cos\theta_i}{a(\theta_i)}. \tag{5.4}$$

Here, $f(\cos\theta_{dir})$ is the function that represents the distribution of the opening angle between the direction of the generated particle and the vector from reconstructed vertex to the hit-PMT position. A plot of $f(\cos\theta_{dir})$ for 10MeV electrons is shown in Fig 5.6(a). The distribution is broad with the peak at 42° because of the effects of electron multiple scattering and Cherenkov light scattering in water. θ_i is the opening angle between the direction of the vector from reconstructed vertex to the position of i-th hit-PMT and the direction that hit-PMT is facing, and $a(\theta_i)$ is acceptance of the photo-cathode of PMTs as a function of θ_i, as shown in Fig 5.6(b).

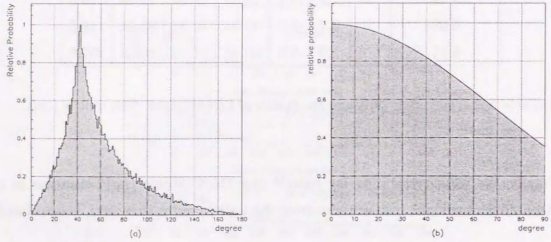

Figure 5.6: (a) The distribution of the opening angle between the direction of the generated particle and the vector from reconstructed vertex to the hit-PMT position. This plot is made for 10MeV electron Monte Carlo. (b) The acceptance of hit-PMTs as a function of angle of incidence. This is made by Monte Carlo simulation.

The direction is $\vec{d}$ determined by maximizing Eq(5.4) using grid search method which

step sizes are $20°, 9°, 4°, 1.6°$.

The quality of the directional reconstruction is estimated by Nickel and LINAC data. The uniformity of the directional reconstruction is checked by Nickel data. The direction cosine distribution is shown in Fig 5.7. This figure shows Nickel data for a center position. This is checked at various position and is almost flat in every position.

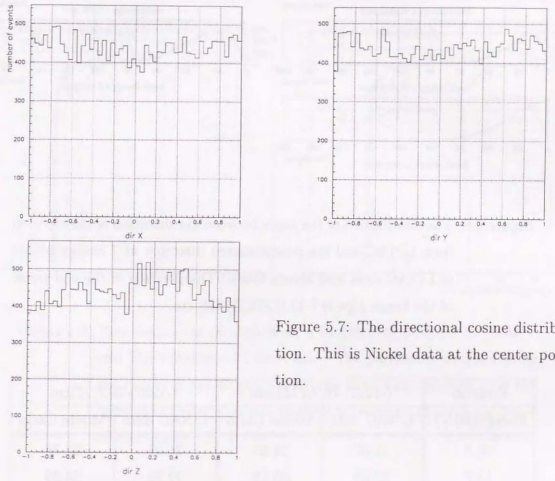

Figure 5.7: The directional cosine distribution. This is Nickel data at the center position.

Fig 5.8 shows the distribution of the angle between the known direction of the electron from LINAC and the reconstructed direction. Fig 5.8 also shows Monte Carlo distributions for the same circumstances. In this figure, the directional reconstruction of Monte Carlo is reproduced by the measured data. The directional resolution is defined by the value which includes 68% in these figures. The directional resolution for each energy of LINAC data is shown in Table 5.4.

The directional resolution was also calculated by Monte Carlo at various positions

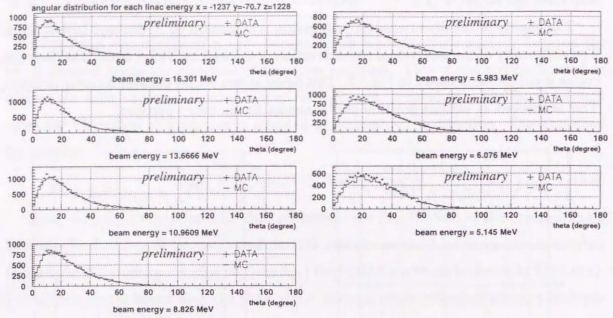

Figure 5.8: The distribution of the angle between the direction of the electron from LINAC and the reconstructed direction at 7 energy points in LINAC data and Monte Carlo. The position of the end point of the beam pipe is (-1237,-70.7,1228)cm.

Position	(-1237,-70.7,1228)cm		(-1237,-70.7,27)cm	
Energy(MeV)	LINAC data	Monte Carlo	LINAC data	Monte Carlo
16.3	21.37	21.03	21.07	21.78
13.7	22.50	23.69	22.79	24.39
11.0	24.90	26.66	25.72	27.08
8.83	28.48	29.71	28.76	31.43
6.98	31.69	33.35	32.24	35.75
6.08	33.87	35.48	34.60	38.43
5.15	35.62	38.18	36.89	41.94

Table 5.4: The directional resolution of LINAC data. The beam direction is (0,0,-1). The unit is degree.

and energies. Fig 5.9 shows that when the distance from the wall is less than 2m, the resolution is dramatically worse. The fiducial volume for solar neutrino analysis is used within 2m from the wall, which is 22.5kton, as described in Section 7.2.

The directional resolution was calculated to 26.7° at 10MeV electron Monte Carlo when the generated vertex is random in 22.5kton fiducial volume.

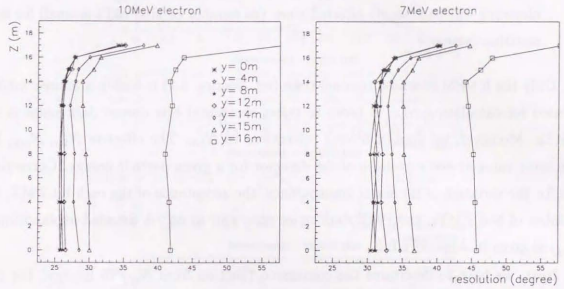

Figure 5.9: The directional resolution as a function of position for 10MeV and 7MeV electron Monte Carlo. The parameter distinguishing the curves is the distance from the tank axis. In each case the right most curve is outside the fiducial volume, as is the top point of each curve.

5.3 Energy reconstruction

The energy of a charged particle is approximately proportional to the number of Cherenkov photons, and thus also proportional to the total number of photo-electrons in hit-PMTs. For analysis of the solar neutrino events in Super-Kamiokande, however, the number of hit-PMTs (N_{hit}) with some corrections is used for energy determination instead of the total photo-electrons. The reason is

(1) for low energy events, the mean number of Cherenkov photons in each hit-PMT is almost one, so the total number of photo-electrons and the number of hit-PMTs are almost the same,

(2) the charge resolution at the one photon level is not good enough,

(3) PMT or electronics noise can give high p.e. per tube, so the total number of photo-electrons will be strongly affected since the number of hit-PMTs is small for solar neutrino events.

Only the hit-PMTs whose residual time (ref. Section 5.1) is within a 50nsec window is used for calculating N_{hit}, in order to reject accidental hits due to dark noise in the PMTs. Moreover, we applied several corrections to N_{hit}. The effective N_{hit}, N_{eff}, has the same value at every position of the detector for a given particle energy. Corrections are for the variation of the water transparency, the acceptance of the each hit-PMT, the number of bad PMTs, the PMT dark noise rate, and so on. A detailed explanation of N_{eff} is given in Appendix B.2.

Next, we have to determine the conversion function from N_{eff} to Energy. For this purpose, a Monte Carlo simulation, in which several parameters are tuned with the 10 points of LINAC data with the energy grater than 6.5MeV, is used. The energy distributions using this tuned Monte Carlo are well reproduced by the LINAC data at each energy. These are shown in Fig 5.10. The greatest difference of the peak value between Monte Carlo and LINAC data at 7 energy points is $\pm 1.3\%$. The greatest difference in resolution is $\pm 4.7\%$. These are summarized in Table 5.5.

One of the most significant uncertainties of Monte Carlo is water transparency. Therefore, we check the position dependence of the energy scale using Nickel data in addition to LINAC data. Nickel calibration was done at more positions than LINAC. [1] (The distance of the Nickel source position from the wall is 2.1m, 4.9m, 6.1m and 16.2m. The height of the source is ± 16m, ± 12m and 0m.) The difference of the energy scale at each position between Nickel data and Monte Carlo is at most 1.4%.

Fig 5.11 shows the N_{eff} distribution of 10MeV Monte Carlo electron events. The mean value is 69.72 in this figure, so events with $N_{eff} = 69.72$ are taken to be 10MeV

[1] The position measured by LINAC is recently increased[40]. The position dependence calculated by recent LINAC measurement is described in Appendix B.3.

electrons. Fig 5.12(a) shows the relation of mean N_{eff} to generated energy. The energy resolution as a function of the energy is shown in Fig 5.12(b). This was calculated using Monte Carlo events. The energy resolution for 10MeV electrons is 14.8%.

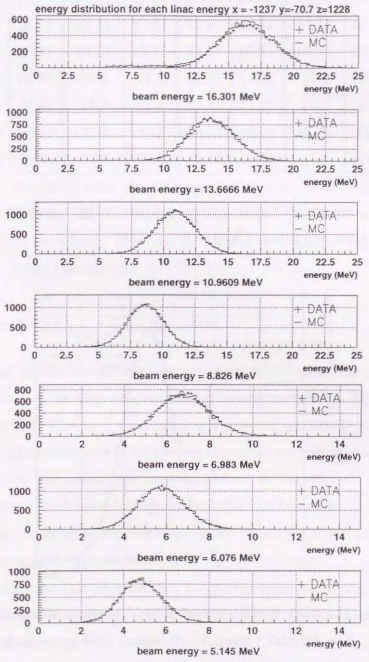

Figure 5.10: The reconstructed energy distribution at 7 energy points in LINAC data and Monte Carlo. The position of the end point of the beam pipe is (-1237,-70.7,1228)cm.

Position:(-1237,-70.7,1228)cm				(-1237,-70.7,27)cm			
reconstructed energy (MeV)		resolution (%)		reconstructed energy (MeV)		resolution (%)	
data	M.C.	data	M.C.	data	M.C.	data	M.C.
16.35	16.57	13.26	12.26	16.51	16.45	13.04	12.26
13.73	13.78	13.32	13.27	13.78	13.72	13.32	12.72
10.93	11.00	14.38	14.12	11.04	10.92	14.54	14.18
8.66	8.71	16.17	16.25	8.74	8.72	16.34	15.58
6.73	6.75	18.15	18.13	6.73	6.74	18.15	17.21
5.72	5.75	19.00	18.96	5.76	5.75	19.06	19.01
4.75	4.79	21.70	20.13	4.77	4.77	20.97	20.19

Table 5.5: The reconstructed energy and the energy resolution of LINAC data and Monte Carlo.

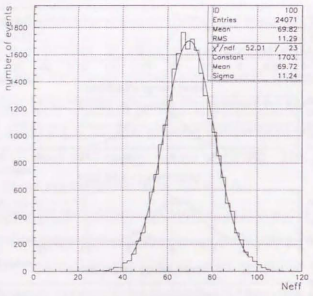

Figure 5.11: The N_{eff} distribution of 10MeV electron Monte Carlo events. The fiducial volume is 22.5kton. The generated vertices are uniformly distributed in this volume. The fit parameters are for a Gaussian.

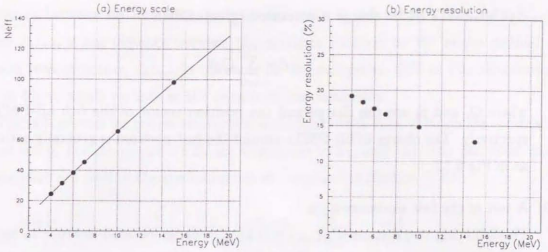

Figure 5.12: (a) The relation of the mean of N_{eff} to the generated energy. Each point is calculated by Monte Carlo as in Fig 5.11, where the mean from the fit is used here. The fit is to a 4-th order polynomial. (b) The energy resolution ($\frac{\sigma_E}{E} \times 100\%$) as a function of the energy. This uses the same Monte Carlo samples and the same Gaussian fits as Fig 5.11.

5.4 Muon track

In Super-Kamiokande, cosmic ray muon events which show up as through going muons, stopping muons, or edge clipping muons happen at 1.88Hz. This is described in Section 7.2.3 in detail. The typical energetic muon event pattern is shown in Fig 5.13. Most are through going muons. Fig 5.14 shows the event pattern of other types of muon events. The rates for each muon type are summarized in Table 5.6.

Spallation events, which are a background for the solar neutrino analysis, are caused by energetic muons. In order to eliminate spallation events from this analysis, the tracks of energetic muons must be reconstructed well.

The entrance and the exit positions for the penetrating muon track must be found for the reconstruction. Two reconstruction methods are applied in sequence. The logical flow of muon track reconstruction is described below.

(1) Fast reconstruction

The entering position is defined by the position of the earliest hit-PMT with more than two neighboring hit-PMTs. The exit position is defined by the center position

$\vec{c}$ of hit-PMTs whose charge is saturated (greater than 231p.e.),

$$\vec{c} = \sum_{i=1}^{N_{hit}} Q_i \vec{p}_i$$

where Q_i and $\vec{p}_i$ are the charge and the position vector of the i-th hit-PMT, respectively. The charge of hit-PMTs around the exit position is generally saturated as in Fig 5.13.

(2) A test of the fast reconstruction

The following two distances, (L_{ent}) and (L_{exit}), are calculated in order to test the result of the fast reconstruction. For each saturated PMT L_{ent} (L_{exit}) is its distance from the putative entrance (exit) point. It is required that at least one saturated PMT which satisfies 1) $L_{ent} > 300$cm and 2) $L_{exit} < 300$cm exists. Criteria 1) is for identification of stopping muons, and 2) is for multi bundle muons.

(3) Precise reconstruction

If an event does not satisfy the criteria described in (2), a precise re-determination of the exit position is done. A grid search method is applied in order to find the maximum goodness. The goodness for the search is:

$$goodness = \frac{1}{\sum \frac{1}{\sigma_i^2}} \times \sum_i \frac{1}{\sigma_i^2} \exp\left[-\frac{1}{2}\left(\frac{t_i - T}{1.5\sigma_i}\right)\right]$$

$$t_i = T_i - \frac{l_\mu}{c} - \frac{n}{c} l_{ph}$$

where T is the entering time of muon, σ_i is the PMT timing resolution, which is uniformly 3nsec, T_i is time of i-th hit-PMT, c is light velocity, n is the index of refraction of water, and l_μ and l_{ph} are the distances shown in Fig 5.15.

(4) A test of the precise reconstruction

The same criteria as described in (2) is applied first. In addition, we also require $goodness > 0.88$. If an event does not satisfy these conditions, it is regarded as an unfitted event. The track reconstruction parameters are not used.

The quality of muon track reconstruction is estimated by comparison of the above method and manual reconstruction. The manual reconstruction is the method which determines the entering and exit position using event pattern by eye. Fig 5.16 shows the

difference between two methods, and the difference is defined by $(\Delta L_{ent} + \Delta L_{exit})/2$, where ΔL_{ent} is the distance between the entrance position by the above method and manual reconstruction, ΔL_{exit} is the same for the exit point. 68% in this distribution is within 67cm, which we take as the reconstruction resolution.

The failure rates for the reconstruction methods in each type of muon are summarized in Table 5.6. For the events which are impossible to fit, only the time and total charge information are used in the spallation cut as described in Section 7.2.4.

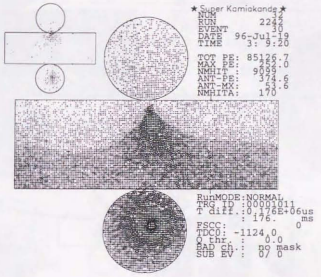

Figure 5.13: The typical event pattern of an energetic muon.

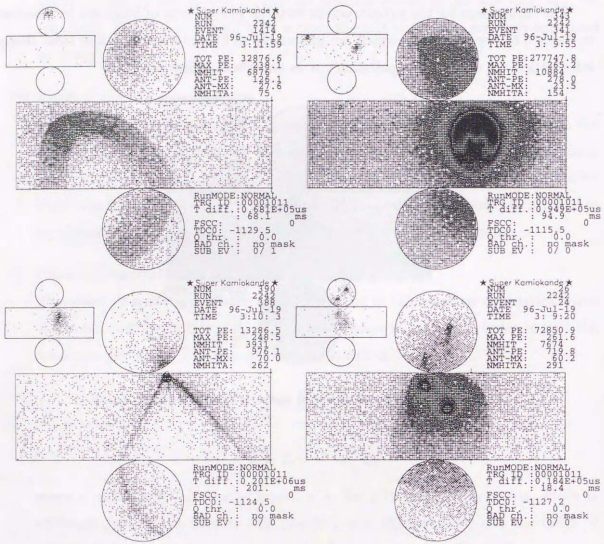

Figure 5.14: Representative event patterns for various muon types. (a) stopping μ, (b) hard interaction μ, (c) edge clipping μ, (d) bundle of multiple μ

muon type	number of events	impossible to fit
normal	835	5
stopping	10	8
hard	41	2
edge clipper	58	19
multi bundle	56	28
Total	1000	62

Table 5.6: The event rate of each muon types and the failure rate of the reconstruction are summarized. This represents approximately 15minutes of data. Human scanning was done on each event to determine the event type.

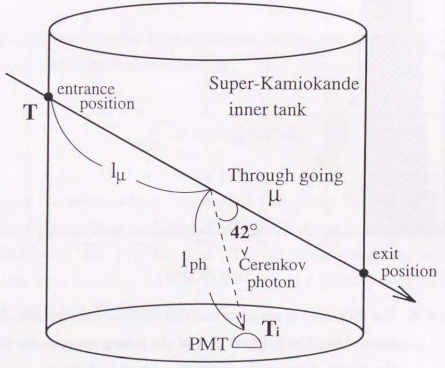

Figure 5.15: The definition of l_μ and l_{ph} for the muon track reconstruction. For a given photon, l_μ is the distance the muon travels from the detector entrance to the emission point, and l_{ph} is the distance traveled by the photon from there to the detection point.

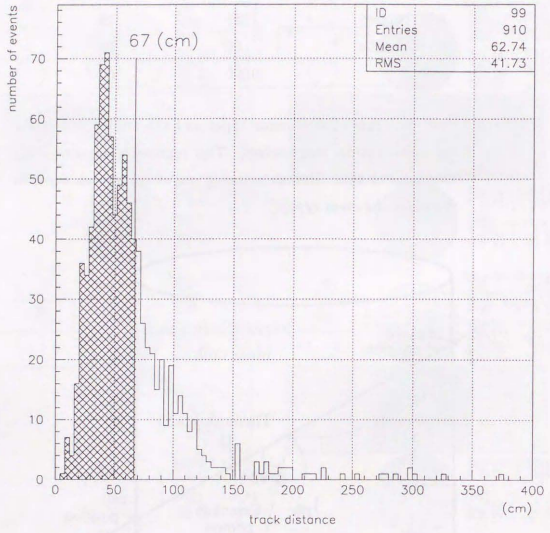

Figure 5.16: The difference of entrance and exit position between auto fit and manual fit. The hatched part of the histogram contains 68% of the events, defining the distance resolution of the automatic fit.

Chapter 6

Monte Carlo simulation

6.1 Solar neutrino event generation

The expected total number of recoil electrons from solar neutrinos in the inner detector of Super-Kamiokande is calculated by

$$\int_0^\infty \phi(E_\nu)\sigma_{total}N_e T dE_\nu, \tag{6.1}$$

where $\phi(E_\nu)$ is the solar neutrino flux at earth (here, only ^{8}B and hep), σ_{total} is total scattering cross section, N_e is total number of target electrons in the detector (1.086×10^{34} electrons/34481tons), and T is live time. The calculated event rate from Eq(6.1) is 55.8events/day for a total flux of 1×10^6 (cm^{-2} s^{-1}), so if BP95 is taken as the standard solar model, the rate is 369.7events/day.

However, many more events for Monte Carlo simulation are needed to reduce the statistical error of the calculation. The generated event rate is 20 per minute for the full operation time. For this analysis, the total number of generated events is 4428360 events.

The generated position is uniform in the whole volume, and the energy and the direction of recoil electrons are determined according to the distribution in Eq(3.9) and Eq(3.11), respectively.

6.2 Detector simulation

6.2.1 Framework of the simulation program

The detector simulation program consists of the following three steps:
(1) particle tracking and Cherenkov photon emission in the water,
(2) propagation of Cherenkov photons,
(3) response of the PMT and electronics.

Particle Tracking

GEANT 3.21[45] was used for detector simulation in Super-Kamiokande. It was developed at CERN, used generally in high energy physicists, and checked by many physicists. GEANT is able to simulate the electromagnetic processes which occur in the energy range from 10keV up to 10TeV.

The electromagnetic interaction in GEANT was also tested against EGS. For example, Fig 6.1 shows the number of generated Cherenkov photons, in electron and gamma events with 9MeV in GEANT and EGS. These are quite consistent. With several comparisons, it was checked that GEANT was accurate enough to use in Super-Kamiokande[46].

Fig 6.2 shows tracks of twenty 10MeV electrons in water using GEANT. The dominant processes for this energy region are multiple scattering, ionization loss, δ-ray production, bremsstrahlung and annihilation of positrons for electrons, and pair creation, Compton scattering and photoelectric effect for gammas.

The number of generated Cherenkov photons, the direction of the each photon and its wavelength are calculated using Eq(3.1) and Eq(3.2). The dependence of the refractive index on wavelength was used as shown in Fig 6.3[47]. The Cherenkov photons are only generated between 300nm and 700nm because PMTs are only sensitive to this region as shown in Fig 3.13. Fig 6.4 shows the total number of emitted Cherenkov photons from electrons in water as a function of electron kinetic energy. It is approximately proportional to the electron energy, and this proportionality constant is a good scale for energy as described in Section 5.3.

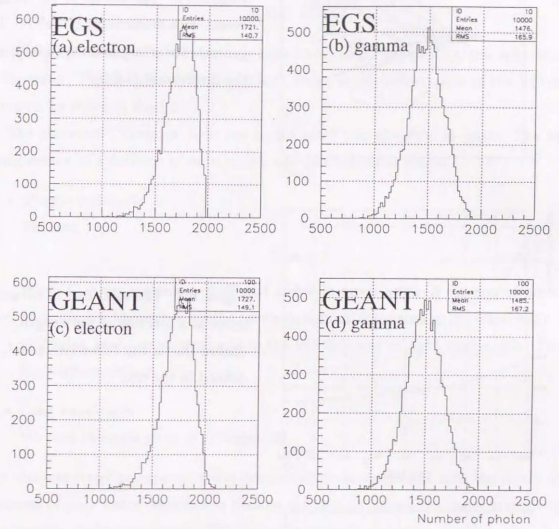

Figure 6.1: The distribution of the number of generated Cherenkov photons. (a) 9MeV electron events in EGS, (b) 9MeV gamma events in EGS, (c) 9MeV electron events in GEANT, (b) 9MeV gamma events in GEANT.

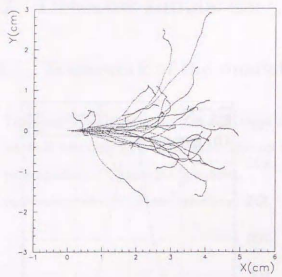

Figure 6.2: The tracks of 20 electron events with momentum 10MeV/c. The generated starting point is (0,0,0), and the direction is (1,0,0).

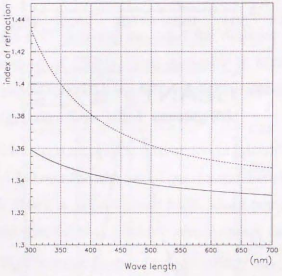

Figure 6.3: The solid line is refractive index as a function of wavelength. The dashed line is the "effective index", as defined in the text.

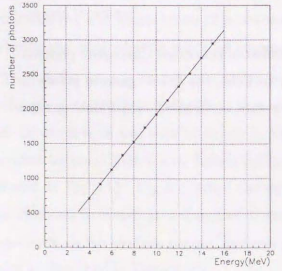

Figure 6.4: The number of generated Cherenkov photons as a function of generated electron energy in Monte Carlo simulation. The curve is a linear fit to the points.

Tracing Cherenkov light in water

We have taken into account the dispersion of the refractive index. The group velocity

$$v_g = \frac{c}{n(\lambda) - \lambda \dfrac{\partial n(\lambda)}{\partial \lambda}}, \tag{6.2}$$

where c is light velocity in vacuum, λ is light wavelength, was used for the light velocity in the water. The so-called "effective index", which is the denominator of this equation, is shown for water in Fig 6.3.

The generated Cherenkov light can be scattered and absorbed in water. The water transparency as a function of wave length was determined as follows.

- Short wavelength
  We used
  $$C \propto \lambda^{-4}$$
  where C is the scattering coefficient and λ is wavelength. If the size of particles with which a Cherenkov photon interacts is small compared to the wavelength, the scattering length is proportional to the fourth power of light wavelength. This is Rayleigh scattering.

- Long wavelength
  We used the data given in reference[48].

The absolute water transparency was determined to be consistent with the direct measurement of pure water described in Section 4.4. Fig 6.5 shows the water transparency as a function of the wave length. This ratio of scattering and absorption is a tunable parameter in the Monte Carlo. This has not been measured directly yet, so the parameter is tuned using LINAC and other calibration data.

When the Cherenkov light arrives at the surface of a PMT or black sheet, reflection on the surface is possible. The reflection of the PMT glass as a function of the incoming angle is calculated as shown in Fig 6.6(a)[49]. We also measured it. The calculated value (including the polarization) is used for the simulation.

The reflection by black sheet is calculated and measured in water, and the result is shown in Fig 6.6(b). The measured value is consistent with the calculated one. We have used the calculated value. The polarization is also considered.

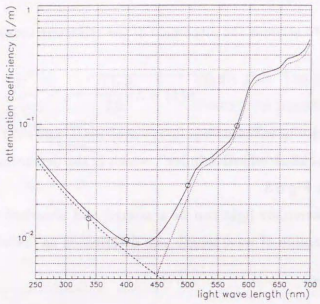

Figure 6.5: The attenuation coefficiency which put in Monte Carlo. The circle is the direct measurement data.

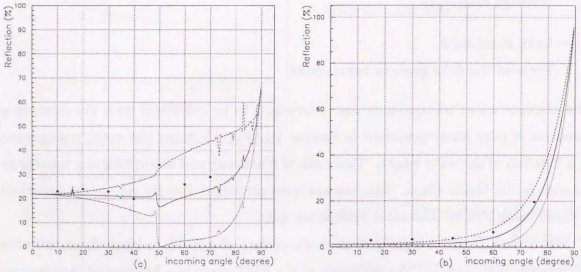

Figure 6.6: The reflection probability on the surface of a PMT (a) and a black sheet (b) as a function of incoming angle. The lines are calculations: the dashed line is S-wave, the dotted line is P-wave, the solid line is averaged value. Points show the measured values.

response of the PMT and electronics

The quantum efficiency of the PMTs (see Section 3.2.3) is shown in Fig 3.13. Fig 6.7 shows (1) the Cherenkov light spectrum generated, (2) upon arrival on the surface of PMT, and (3) after convolution of Q.E. for 10MeV electrons generated through entire volume.

The average value of the collection efficiency of PMT, which is more than 70%, is also treated as a tunable parameter. This is used for the final adjustment of the energy scale.

Charge and timing resolution of PMT are considered. (see also Chapter 4) Fig 4.3 shows charge distribution for one photon. The charge value of each hit-PMT in Monte Carlo is determined by random number distributed as shown in that figure. The timing distribution dependent on charge is measured using a laser as described in Section 4.3. Fig 4.6 shows the timing resolution at various charge. In the Monte Carlo, the timing of each PMT is a Gaussian random variable with the sigma shown in Fig 4.6.

Finally, trigger simulation is applied. The details of the trigger were described in Section 3.2.4. A comparison of trigger efficiency in Monte Carlo and the real data was described in Section 4.6.

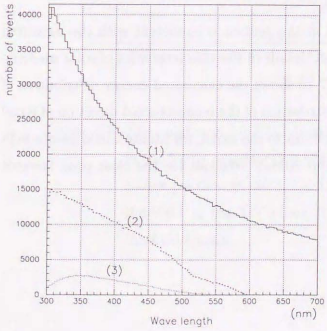

Figure 6.7: The Cherenkov light spectrum at various steps: (1) generated, (2) arrival on the surface of PMT, (3) included Q.E. This is output from Super-Kamiokande Monte Carlo simulation.

6.2.2 Monte Carlo tuning

The previous section introduced some parameters of the Monte Carlo program. Most of these parameters are determined independently by direct measurements. Two parameters have to be tuned. They are not completely free, but have standard values and tunable ranges which are based on some measurements. They are:

1. the ratio of scattering and absorption.

   For long wavelength, infrared absorption is dominant. For short wavelength, scattering is dominant.

2. the collection efficiency of the PMTs.

   This parameter is constrained to be more than 70% which is the result of the direct measurement in Hamamatsu Co[36].

The ratio of scattering and absorption is determined using the event pattern of Nickel and LINAC calibration data. For example, Fig 6.8 shows the hit pattern of Nickel calibration around the center of the barrel PMT. Data and Monte Carlo agree very well.

The collection efficiency for PMTs was used to tune Monte Carlo in the last step. It is determined by adjusting the energy scale to measured data of LINAC calibration at various positions. The value used is 78%.

The tuned Monte Carlo as described in this section is consistent with the measured calibration data. It can be used to predict details of the characteristics of solar neutrino distributions with great confidence. Fig 7.15 shows the calculated energy distribution of Monte Carlo events. Fig 6.9 shows the distribution of the reconstructed direction of recoil electrons relative to the direction from the sun to the earth, for Monte Carlo events with reconstructed energy between 6.5MeV and 20MeV. We can see the clear peak towards the sun.

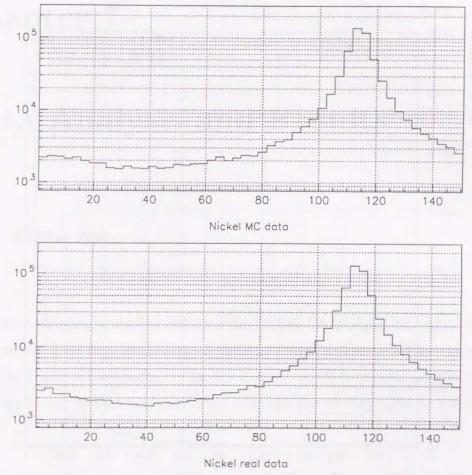

Figure 6.8: The number of hit-PMT belonging to the layer from 21st to 31st in the barrel as a function of phi angle of the PMT position. The source position is (30.3,-1555,0)cm. Phi is the location angle of the PMT in the X-Y plane. The Monte Carlo (top plot) is after the final tuning.

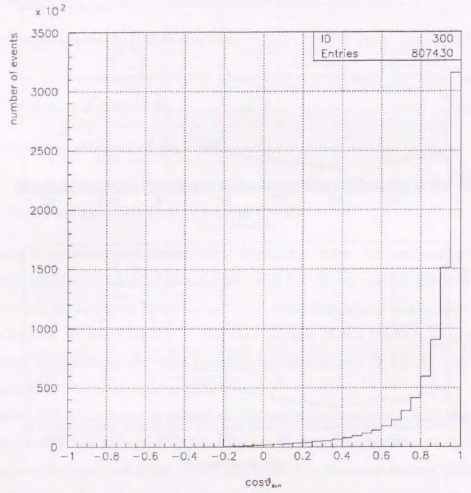

Figure 6.9: The distribution of the reconstructed direction of recoil electrons relative to the direction from the sun to the earth for the Monte Carlo sample.

Chapter 7

Data Analysis and Results

7.1 Data set

Super-Kamiokande started taking data on the 1st of April in 1996, but the water transparency in the first two months of the experiment as shown in Fig 4.14 was changing rapidly and did not have sufficient quality to allow an efficient solar neutrino search. The data used for the present analysis covers from the 31st of May, 1996 to the 23rd of June, 1997.

Data are taken in runs of at most approximately 24 hours. Each run further consists of 10 minutes subruns. We removed some runs or subruns as a bad "run" from the analysis if they did not satisfy the selection criteria. We will describe this in detail later. "Flash PMTs" described in the next section were the main reason for the rejection. The live time fraction is shown in Fig 7.1. It became more than 90% after October, 1996. The total analysis live time between the 31st of May, 1996, the first day of the present data, and the 23rd of June, 1997 was 297.4 days.

The "raw data" were $\sim 9.5 \times 10^5$ events/day which is equivalent to 10.9Hz. Since the expected observable solar neutrino event rate (assuming the BP95 SSM) is 46.4 events/day above 6.5MeV threshold, the signal to noise ratio (S/N) is $\mathcal{O}(10^{-5})$.

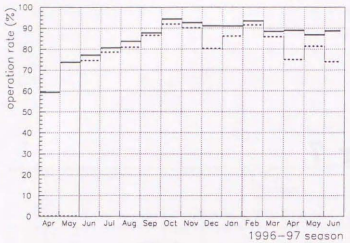

Figure 7.1: The efficiency of the experimental operation. The solid line shows the data acquisition live time, and the dashed line shows the solar neutrino analysis live time.

7.2 Data reduction

7.2.1 First reduction

Selection of low energy events

The first step of the reduction is to select the low energy events. Fig 7.2 shows the total charge of inner hit-PMT distribution for all events in one run. There are two peaks which are caused by muon events and low energy events. The following cut to select low energy events is applied,

(1) total charge of inner hit-PMT $\leq$ 1000 p.e.;
Here, 1000 p.e. is equivalent to about 100MeV. The inefficiency of this cut for solar neutrino events is negligible.

The decay electron events from stopping muons are a background to solar neutrino analysis because the energy range is close to solar neutrino event. To reject them, the time difference from the previous event is used. Fig 7.3 shows the time difference distribution.

(2) the time difference from the previous event $> 20\mu$sec.;
The dead time caused by this cut is calculated to be 1.8×10^{-4}. It is ignorable.

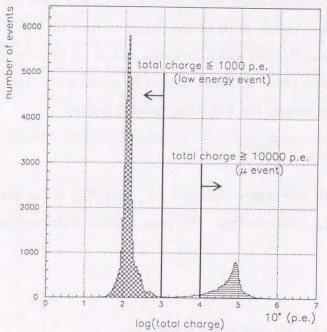

Figure 7.2: The total charge of inner hit-PMT distribution in one typical run. All events acquired by the online software are represented here. (No cuts are applied.)

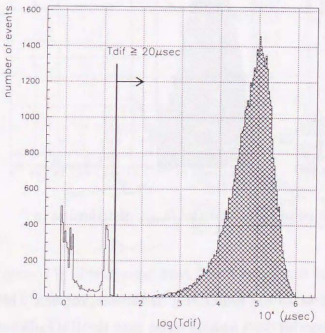

Figure 7.3: The distribution of the time difference from the previous event in one typical run. These are the same data as in the previous figure.

Reduction of noise events

Electronics sometimes pick up noise, for example, from turning on a fluorescent light. Fig 7.4 shows the typical electronics noise event. Most of the charge of each hit-PMT in this noise event is at the level of less than 0.5 p.e, and sometimes picked up by only one ATM board. Note that, this kind of noise event occurred especially in the early time of the experiment. In order to reject noise events, the following value is defined,

$$R_{noise} = \frac{N_{noise}}{N_{hit}},$$

where N_{noise} is the number of hits with the charge -0.5~0.5 p.e., and N_{hit} is the total number of hits. Fig 7.4 shows the R_{noise} distribution. We have applied following two cuts,

(3) $R_{noise} < 0.4$.

(4) if all channels in one ATM board are hit, the event is rejected.

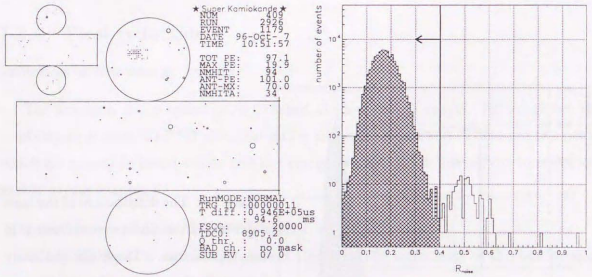

Figure 7.4: The typical electronics noise event and the R_{noise} distribution in one typical run.

In Super-Kamiokande, the phenomenon called "flash PMT" is serious problem. That is generally caused by electrical discharge due to a leak of water into the PMT. When a PMT is determined as a flash PMT it is disconnected. The rate of disconnection is 0.25 PMTs per day on average and is shown in Fig 7.5. The typical flash PMT event is

shown in Fig 7.6. There is a hit-PMT with high charge and many hit-PMTs around the flashing PMT. The flash PMT events occur continuously with high rate or sometimes intermittently, and some of them are hard to identify. In order to reject the flash PMT event, the relation between max charge of hit-PMT and the number of hit around the cable with max charge is used. Fig 7.6(a) shows the typical run including a lot of flash PMT events, and (b) shows a normal run, therefore,

(5) the region indicated in Fig 7.6(a) is rejected.

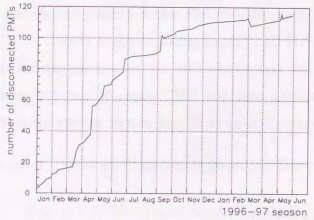

Figure 7.5: The number of disconnected PMTs as a function of time. At some times (for example, early March, 1997) some previously disconnected PMTs were reconnected after reanalysis.

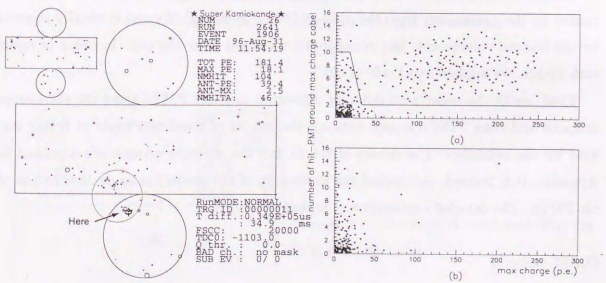

Figure 7.6: The typical flash PMT event and the relation between max charge of hit-PMT and the number of hit around the cable with max charge. (a) The typical run including a lot of flash PMT events. (b) The normal run. Events above and to the right of the cut shown in (a) are rejected.

Reduction related to reconstruction

After reconstruction (see Chapter 5), the following reductions are applied:

(6) Events with less than 10 hit-PMT are rejected.

(7) *goodness* ≥ 0.4 is required.

The events which have too few hit-PMT are not guaranteed to be reconstructed well, so they are not reconstructed. Fig 7.7 shows scatter plots of *goodness* and N_{hit}. Events with small *goodness* but large N_{hit} are flash PMT events which cannot be rejected by (5). (The typical event is shown in Fig 7.7) Cut (7) is applied to reject these.

Most of the remaining events after the above reduction are caused by gamma rays from radioactive elements in the surrounding rock and PMT glass, or very low energy background events. The following pre fiducial volume cut and energy cut are applied:

(8) the distance from the wall >1.5m and the energy >5.5MeV for events to be accepted.

Fig 7.8 shows a remaining noise event and it is a PMT adjoin noise. We suspect it is caused by the gamma ray from the glass of PMT. This kind of event is usually rejected by the fiducial volume cut, but occasionally remained after the cut. In order to reject such events, we applied two kinds of cut.

First, we fit the event with different algorithm to select PMTs using the correlation in space and time. The distance between the results of these two kinds of fitting was used for the reduction. The details of the fit and the selection criteria are described in Appendix B.4. Second, we checked the uniformity of the azimuthal angle distribution of hit-PMTs. The detailed explanation is in Appendix B.5.

Other criteria

Before the reductions explained above, we rejected the following events: the outer triggered events; events during ATM pedestal data taking; and any events that were not fully acquired by the online software.

The event rate of outer detector triggers is 2.1Hz, which is mostly caused by cosmic ray muons from outside of the detector.

Pedestals of the ATM modules are measured every 30 minutes taking approximately about 1 minute. During pedestal data taking, 1/8 of all the ATMs are not active, so we do not use events in this time for solar neutrino analysis. The dead time caused by the pedestal and incomplete data is calculated to be 2.66% totally.

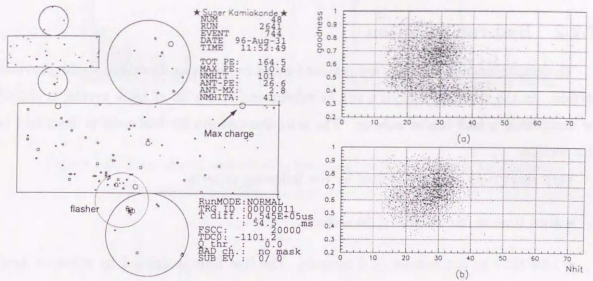

Figure 7.7: The typical event with small *goodness* and large N_{hit}. and scatter plots of *goodness* and N_{hit} for two runs. The data in (a) have many remaining flash PMT events. (b) is a normal run.

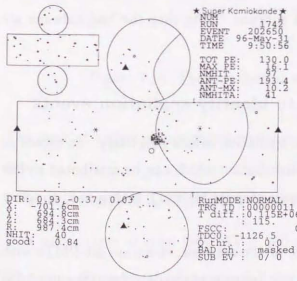

Figure 7.8: The typical event including the PMT adjoin noise.

Summary

Table 7.2 (page 115) summarizes the first reduction and the number of events remaining at each step. After first reduction, the number of remaining events is 1.298×10^6, which is equivalent to 0.0505Hz. Fig 7.15 shows energy distribution of those events.

7.2.2 Bad run selection

The events considered noise are removed event by event as described in the previous section. As the result of that, if a run or subrun includes a lot of noise events, it should be designated a bad run or subrun. The selection criteria for bad runs is described in this section.

Very short runs were first killed by the following criteria,

- Run time in one subrun $\leq$ 30 seconds.
- Live time in one subrun $\leq$ 0 seconds. The live time is defined by subtract dead time from run time.
- Total live time in one run $\leq$ 5 minutes.

Subruns including many electronics noise events or flash tube events are killed. For this purpose, we check the ratio of number of noise events to all events. Fig 7.9 shows the ratio distribution and the selection criteria. The number of subruns selected as bad subruns is 1550 out of a total or 30503 subruns. Note that the bad subruns are preferentially shorter than good ones.

7.2.3 Selection of muon events to identify spallation events

We have to select muon events to remove spallation events effectively. As shown in Fig 7.2, there are two peaks in total charge distribution which can be attributed to low energy events and muon events. The total charge of inner hit-PMT is thus used to select muon events.

Also since muon events enter from outside of the detector, there are hit-PMTs with very high pulse height around the entrance or exit position of the detector. (See Fig 5.13) Fig 7.10 shows the distribution of max charge of inner hit-PMT. There are two peaks.

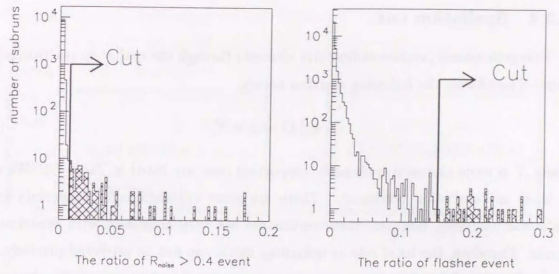

Figure 7.9: The ratio of number of noise events or flasher events to all events. The selection criteria for bad runs is also shown.

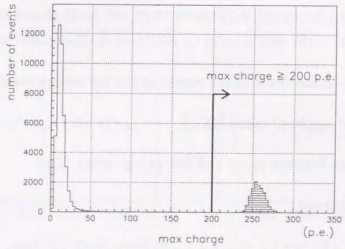

Figure 7.10: The distribution of max charge of inner hit-PMT.

The peak at higher charge represents through going muons. The cuts to select muons are:

- total charge of inner hit-PMT $\geq$ 10000 p.e.,
- max charge of inner hit-PMT $\geq$ 200 p.e..

The event rate after this selection is 1.88Hz. 96.4% of those events are reconstructed with sufficiently high quality.

7.2.4 Spallation cut

Energetic muons produce radioactive elements through the spallation reaction[50]. In Super-Kamiokande the following reaction occurs,

$$\mu + {}^{16}\mathrm{O} \rightarrow \mu + X, \tag{7.1}$$

where X is some radioactive element. Important ones are listed in Table 7.1. We refer to these as "spallation products". There are some calculations[51] to explain muon spallation processes, however, these results are not very consistent with experimental results. Therefore, the total rate or branching ratios can not be predicted precisely.

As shown in Table 7.1, the spallation products give β and/or gammas in the energy range between a few MeV and 20MeV, and the lifetime ranges from 0.01 to 10 seconds or more. This energy region is near the energy of solar neutrino events, so spallation events are one of the major backgrounds for solar neutrino analysis.

These events are correlated with muon track and total charge of muon event. The following correlation is checked in order to eliminate spallation events ("spallation cut"):

- distance from muon track to the vertex of the low energy event (ΔL),
- residual pulse height of muon (Q_{res}),
- time difference between muon and low energy event (Δt).

Q_{res} is defined as follows,

$$Q_{res}(p.e.) = Q_{tot}(p.e.) - 24.1(p.e./cm) \times L_{\mu}(cm), \tag{7.2}$$

where Q_{tot} is total pulse height of muon and L_{μ} is muon track length. In Q_{res}, the photons generated by muon itself are removed. The total charge per 1cm for a muon track was calculated to 24.1(p.e./cm) on average.

We used a likelihood method to remove spallation events. For the spallation events, ΔL and Δt are shorter, and Q_{res} is larger. Fig 7.11 shows ΔL distribution in various Q_{res} region. The peak caused by spallation events is clearly seen in the region of small ΔL, compared to the accidental distribution. The spallation likelihood function is expressed numerically using ΔL, Q_{res} and Δt. The detailed definition of the spallation likelihood is described in Appendix C.1.

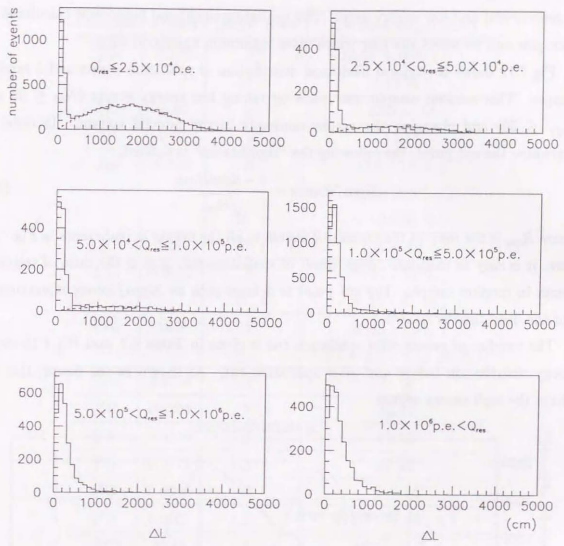

Figure 7.11: The distribution of the distance between the muon and low energy event in various residual charge regions. This low energy events are defined by $N_{eff} \leq 50$. The time difference between the muon and low energy event is less than 0.1sec. The dashed line is the expected accidental distribution.

All the muon events before 100sec from the each low energy event are considered to be candidates for the origin of the spallation events. Since the muon rate is 1.88Hz and the low energy event rate after the first reduction is 0.0505Hz, there are very many pairs of muon event and low energy event. The spallation likelihood function is calculated for each pair and we select the pair which gives maximum likelihood value.

Fig 7.12 shows the typical likelihood distribution of spallation events and a random sample. This random sample was made by taking low energy events ($N_{50} \leq 25$ and $N_{eff} \leq 30$) and changing the vertex randomly in the fiducial volume. In order to determine the cut point, the following the "significance" is defined,

$$Significance = \frac{1 - deadtime}{\sqrt{R_{spa}}} \tag{7.3}$$

where R_{spa} is the ratio of the remaining events to all the events in real events in Fig 7.12. Here, it is easy to calculate "dead time" of spallation cut, that is the ratio of rejecting events in random sample. The cut point is defined such as $Significance$ is maximum, and the dead time is 19.96%.

The number of events after spallation cut is given in Table 7.2, and Fig 7.15 shows energy distribution before and after spallation cut. As shown in the figure, this cut affects the high energy region.

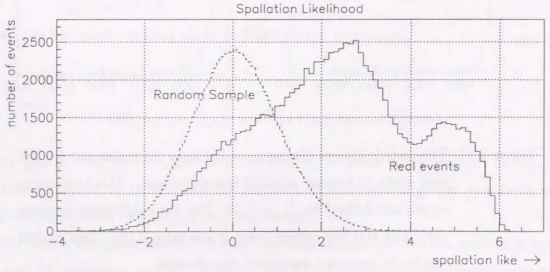

Figure 7.12: The typical likelihood distribution in case of including spallation events (solid line) and only random sample (dashed line).

Isotope	$\tau_{\frac{1}{2}}$(sec)	Decay mode	Kinetic Energy(MeV)
$^{8}_{2}$He	0.122	β^-	10.66 + 0.99 (γ)
		β^- n	(11 %)
$^{8}_{3}$Li	0.84	β^-	12.5 $\sim$ 13
$^{8}_{5}$B	0.77	β^+	13.73
$^{9}_{3}$Li	0.178	β^-	13.5 (75 %)
			11.0 + 2.5 (γ)
		β^- n	$\sim$ 10 (35 %)
$^{9}_{6}$C	0.127	β^+ p	3 $\sim$ 13
$^{11}_{3}$Li	0.0085	β^-	20.77 (31 %)
		β^- n	$\sim$ 16 (61 %)
$^{11}_{4}$Be	13.8	β^-	11.48 (61 %)
			9.32 + 2.1 (γ) (29 %)
$^{12}_{4}$Be	0.0114	β^-	11.66
$^{12}_{5}$B	0.0204	β^-	13.37
$^{12}_{7}$N	0.0110	β^-	16.38
$^{13}_{5}$B	0.0173	β^-	13.42
$^{13}_{8}$O	0.0090	β^-	8 $\sim$ 14
$^{14}_{5}$B	0.0161	β^-	14.07 + 6.09 (γ)
$^{15}_{6}$C	2.449	β^-	9.82 (32 %)
			4.51 + 5.30 (γ)
$^{16}_{6}$C	0.7478	β^-	$\sim$ 4
$^{16}_{7}$N	7.134	β^-	10.44 (26 %)
			4.27 + 6.13 (γ) (68 %)

Table 7.1: Summary of spallation products.

7.2.5 Fiducial volume cut and gamma ray cut

Fiducial volume cut

The gamma rays from the surrounding rocks became serious backgrounds for solar neutrino analysis. Fig 7.13 shows the vertex distribution. We applied the cut,

$$R_{wall} \geq 2m, \tag{7.4}$$

where R_{wall} is the distance from the wall, in order to remove these backgrounds. The fiducial volume is 22.5 kton.

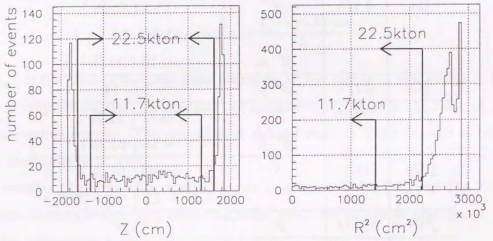

Figure 7.13: The vertex distribution of low energy events. The volume with the distance from the wall greater than 2m is 22.5kton. That is defined as the fiducial volume. The volume defined by making the cut 5m is 11.7kton.

Gamma ray cut

In Fig 7.14 where the vertex and directional cosine distribution of the events after fiducial volume cut are shown, one sees many of the events close to the wall are coming from the wall. To further reduce this background, the following cut is applied;

$$R_{eff} \geq 450cm, \tag{7.5}$$

where R_{eff} is the distance to the wall backward along the event direction. Fig 7.14 also shows the vertex and direction distribution after gamma ray cut.

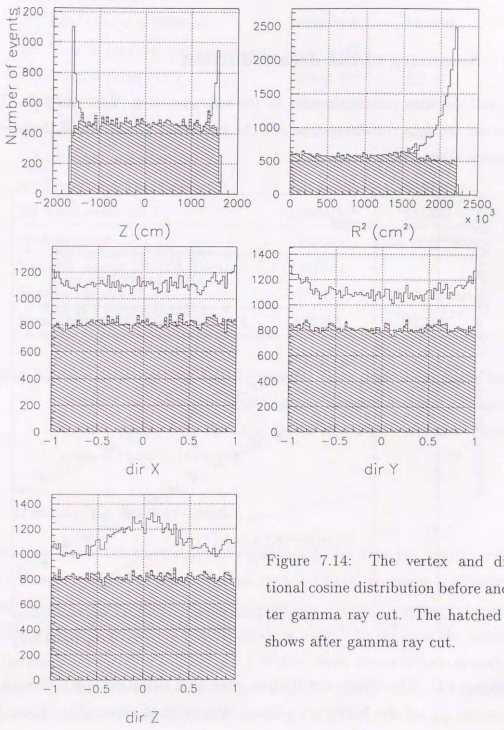

Figure 7.14: The vertex and directional cosine distribution before and after gamma ray cut. The hatched one shows after gamma ray cut.

Table 7.2 shows the number of events passing fiducial volume cut and gamma ray cut in various energy ranges, and Fig 7.15 shows the energy distribution before and after these cuts.

7.2.6 Summary of the data reduction

We call the data sample through all the reduction step "final sample". Table 7.2 summarizes the data reduction steps and the number of events. Fig 7.15 shows energy distribution at each reduction step.

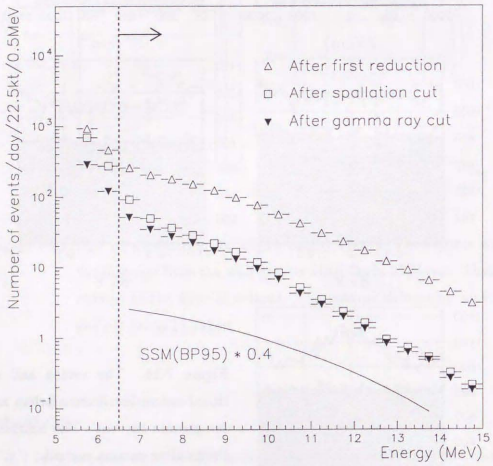

Figure 7.15: The energy distribution after each reduction step. The curve at the bottom is a direct calculation of expectation shown for comparison.

reduction step	number of events	
	Data	Monte Carlo
First reduction		
(1) Total charge $\leq$ 1000 p.e.	2.131×10^8	651310
(2) Time to previous event $> 20\mu$sec.	1.861×10^8	
(3)(4) Noise event cut 1	1.655×10^8	651271
(5) Flash tube cut	1.648×10^8	645770
(6) Very low energy event cut	1.036×10^8	645770
(7) Goodness cut	1.025×10^8	645769
(8) Pre fiducial and energy cut	2.383×10^6	645769
(9) Noise event cut 2	1.298×10^6	617487
Spallation cut	743517	20% dead time
Fiducial volume cut (22.5kton)	426658	
Gamma ray cut	198111	7.8% dead time
Final sample ($6.5 \leq E \leq 20$MeV)	52368	443282

Table 7.2: The reduction step and the results. Note that the numbers for Monte Carlo are after applying the 22.5kton fiducial cut and 6.5MeV energy cut. The numbers for the "First reduction" steps same as those in the text.

7.2.7 Remaining background

As shown in Table 7.2, the number of remaining events after the reduction steps is 52368. (176.1events/day) The signal to noise ratio is $\mathcal{O}(1/4)$ assuming the SSM(BP95) prediction. Many background events are still remaining. The most probable background source is electrons from β decay of ^{214}Bi originating from ^{222}Rn decay in the water tank. Though the end point energy of this decay is 3.26MeV, those events include in the sample above 6.5MeV threshold because of the energy resolution. The radon concentration in the water tank was actually measured[52] and shown in Fig 7.16. It is recently stable at the level of 5$\sim$10mBq/m^3 as shown in the figure. The estimation of the radon concentration from the event rate of very low energy events is 6.3$\pm$2.5mBq/m^3. These are consistent, however, we do not know whether all of the remaining backgrounds are explained only

by the radon or not. We are still studying the origin of the background.

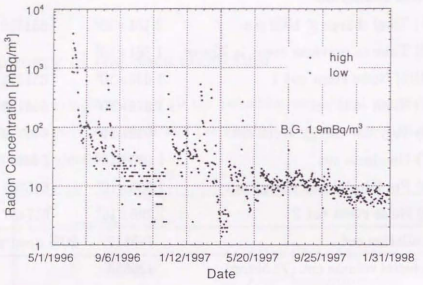

Figure 7.16: The radon concentratin as a function of time.

7.3 Results of solar neutrino analysis

7.3.1 Solar neutrino flux and energy spectrum

Solar neutrino signal extraction

In order to extract solar neutrino signal from the final sample, we make use of the directional correlation of electrons to the incident neutrinos in ν-e scattering. We define an angle θ_{sun}, the angle between the direction of low energy event and the directional vector from the sun. If the signal is coming from the sun, $\cos\theta_{sun}$ distributes around 1 with some angular resolution. Fig 7.17 shows θ_{sun} distribution of the final sample with the energy range from 6.5MeV to 20MeV. As shown in the figure, we can see a clear peak towards the sun above background.

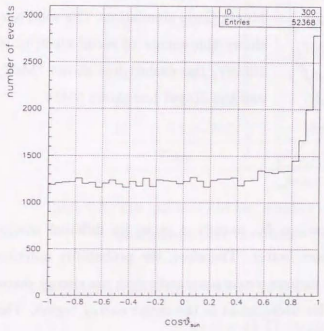

Figure 7.17: The distribution of the reconstructed direction of recoil electrons relative to the direction from the sun to the earth for the final sample.

In order to extract the solar neutrino flux, a maximum likelihood method was used. The probability function is defined as a function of recoil electron energy (E_e) and $\cos\theta_{sun}$;

$$P(E_e, \cos\theta_{sun}, x) = x \times P_{signal}(E_e, \cos\theta_{sun}) + (1-x) \times P_{bg}(E_e, \cos\theta_{sun}), \qquad (7.6)$$

where x is the ratio of number of solar neutrino events to all the events in the final sample. It consists of two parts: signal and background. The probability function for signal, $P_{signal}(E_e, \cos\theta_{sun})$ shown in Fig 7.18, was obtained by Monte Carlo simulation.

The probability function for background, $P_{bg}(E_e, \cos\theta_{sun})$, was obtained by the shape of $\cos\theta_{sun}$ distribution in the final sample in each energy regions. The gamma ray background has directionality because it goes from the wall. This directionality and the cylindrical shape of the detector geometry causes cosine Z distribution to be non-flat before gamma ray cut. (See Fig 7.14) The reason to use the shape of the final sample as background is that the systematic effects caused by this non-flat background can be reduced even after application of the gamma ray cut.

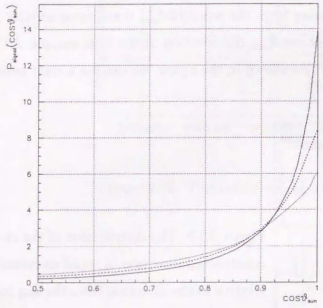

Figure 7.18: The probability function for solar neutrino signal obtained by Monte Carlo simulation. The solid line shows the energy of recoil electron is 10MeV, the dashed line shows 7MeV, and the dotted line shows 5MeV.

The signal to noise ratio differs in various E_e, namely x varies for different energy regions. If the energy is larger, it becomes better. Therefore, the probability function expressed as Eq(7.6) can be applied into various region separately with the energy shape constraint, in order to make use of smaller background in the larger energy region. The probability function is represented as follows,

$$P(E_e, \cos\theta_{sun}, x_i) = x_i(x) \times P_{signal}(E_e, \cos\theta_{sun}) + (1 - x_i(x)) \times P_{bg}(E_e, \cos\theta_{sun}), \quad (7.7)$$

$$x_i(x) = \frac{N}{N_i} \times \frac{N_i^{MC}}{N^{MC}} \times x, \quad (7.8)$$

where N and N_i is total number of events and number of events in each energy region in final sample, respectively. N_i^{MC} and N^{MC} is in expected signal using Monte Carlo simulation, so $\frac{N_i^{MC}}{N^{MC}}$ shows the expected energy shape, which is assumed to be the same as in the solar model of BP95. Results for this analysis are summarized in Table 7.3.

i	Energy(MeV)	N_i (final sample)	N_i^{MC}
1	6.5∼ 7.0	12536	75927
2	7.0∼ 7.5	9617	67694
3	7.5∼ 8.0	7867	59306
4	8.0∼ 8.5	6259	51070
5	8.5∼ 9.0	4818	43196
6	9.0∼ 9.5	3580	35428
7	9.5∼10.0	2597	28522
8	10.0∼10.5	1699	22194
9	10.5∼11.0	1132	17410
10	11.0∼11.5	751	13176
11	11.5∼12.0	509	9492
12	12.0∼12.5	326	6819
13	12.5∼13.0	206	4721
14	13.0∼13.5	166	3188
15	13.5∼14.0	107	1994
16	14.0∼20.0	198	3145
Total		$N = 52368$	$N^{MC} = 443282$

Table 7.3: The summary of the number of events in each energy bin for the final sample and the Monte Carlo sample.

The likelihood function is written as below,

$$L(x) = \prod_{i=1}^{16} \prod_{j=1}^{N_i} P_j(E_e, \cos\theta_{sun}, x_i), \quad (7.9)$$

or

$$\log L(x) = \sum_{i=1}^{16} \sum_{j=1}^{N_i} \log P_j(E_e, \cos\theta_{sun}, x_i). \quad (7.10)$$

We calculate x with the maximum likelihood value (x_{max}) and the number of solar neutrino events is simply

$$N_\nu = x_{max} \times N. \quad (7.11)$$

The statistical error is derived by

$$L(x_{error}) = \exp(-0.5) \times L(x_{max}) \quad (7.12)$$

Fig 7.19 shows the likelihood distribution as a function of x. The results are

$$\begin{aligned} x_{max} &= 0.0767, \\ x_{error} &= \pm 0.002. \end{aligned} \tag{7.13}$$

The number of recoil electron signals from ^{8}B solar neutrino was calculated to be

$$\text{Signal} = 4016.6 \ {}^{+104.7}_{-104.7}(stat.) \ {}^{+208.9}_{-144.6}(sys.) \ \text{events} \tag{7.14}$$

in 297.4 days. For this analysis, the fiducial volume is 22.5 kton and the energy threshold is 6.5MeV. The systematic errors are described in the next section.

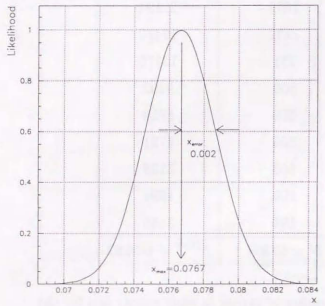

Figure 7.19: The distribution of the likelihood for extraction of solar neutrino signal. The horizontal axis shows the signal to noise ratio, which is a free parameter. The exact definitions of x_{max} and x_{error} are given in the text.

^{8}B solar neutrino flux

Compared to the expected number of signals obtained by Monte Carlo, we can obtain the observed ^{8}B solar neutrino flux. As described in Section 6.1, the predicted ^{8}B solar neutrino event rate arriving at Super-Kamiokande is 55.8events/day when the total flux is assumed 1×10^6 (cm^{-2} s^{-1}) as the unit flux. The number of total generated events is 4428360 and the number of events after several reduction is 443282. Therefore, the event rate which is expected to detect in Super-Kamiokande is calculated to be $55.8 \times 443282/4428360 = 5.59$ events/day. The total live time is 297.4days, so the expected number of event is $5.59 \times 297.4 = 1662.5$ events per unit flux 1×10^6 (cm^{-2} s^{-1}). The number of observed signal is 4016.6 events, so the observed ^{8}B solar neutrino flux is

$$2.42 \ {}^{+0.06}_{-0.06}(stat.) \ {}^{+0.13}_{-0.09}(sys.) \ [\times 10^6/cm^2/sec]. \tag{7.15}$$

Comparing the result to standard solar models, the ratio of data to SSMs prediction is

$$\frac{Data}{SSM} = 0.365 \ {}^{+0.010}_{-0.010}(stat.) \ {}^{+0.019}_{-0.013}(sys.) \ (BP95) \tag{7.16}$$

$$\frac{Data}{SSM} = 0.425 \ {}^{+0.011}_{-0.011}(stat.) \ {}^{+0.022}_{-0.015}(sys.) \ (BP92) \tag{7.17}$$

$$\frac{Data}{SSM} = 0.545 \ {}^{+0.014}_{-0.014}(stat.) \ {}^{+0.028}_{-0.020}(sys.) \ (TL93) \tag{7.18}$$

Fig 7.20 shows the solar neutrino flux obtained at the various intermediate analysis steps. This is for the systematic check of the solar neutrino flux calculation. From the figure, we find that the solar neutrino flux is consistent at each analysis step.

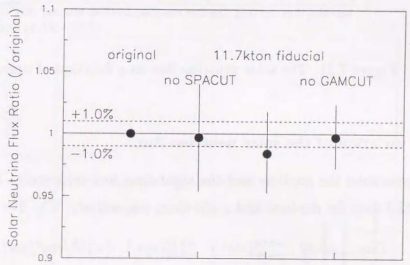

Figure 7.20: The calculated solar neutrino flux at the various intermediate analysis steps. The vertical axis shows the ratio of the flux at each step to the original one.

Stability of the solar neutrino flux

The present solar neutrino results cover over one year. Fig 7.21 shows the solar neutrino flux as a function of time. The orbital eccentricity of the earth causes about 7% flux variation. The measurement is consistent with the expected within the error. The same data can be used to study seasonal variation of the solar neutrino flux in which as shown in Fig 7.21 the just-so oscillation[25] can be studied. The current statistics is unfortunately not very sensitive to check the just-so oscillation, yet.

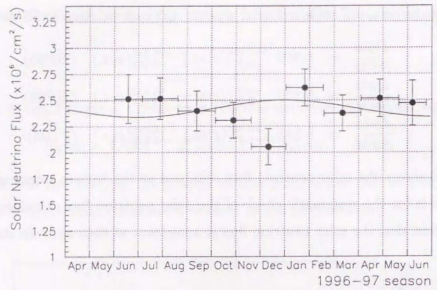

Figure 7.21: The solar neutrino flux as a function of time.

Day/Night variation of the solar neutrino flux

We have measured the daytime and the night-time flux separately. The live time is 145.1 days 152.3 days for daytime and night-time, respectively. The flux obtained is

$$\text{Day} : 2.39 \ ^{+0.09}_{-0.09}(stat.) \ ^{+0.10}_{-0.07}(sys.) \quad [\times 10^6/cm^2/sec]. \tag{7.19}$$

$$\text{Night} : 2.44 \ ^{+0.09}_{-0.08}(stat.) \ ^{+0.10}_{-0.07}(sys.) \quad [\times 10^6/cm^2/sec]. \tag{7.20}$$

The relative difference between the daytime and night-time flux is

$$\frac{Day - Night}{Day + Night} = -0.0104 \pm 0.0258(stat.) \pm 0.0135(sys.). \tag{7.21}$$

In the ratio Day/Night, many of the systematic errors are cancelled, (See Table 7.4). Moreover, the advantage of this analysis is independent from the absolute flux calculations. There is no evidence for the difference between daytime and night-time fluxes within the experimental errors. The implications of these flux measurements are described in the next chapter.

Energy spectrum

The measurement of the solar neutrino energy spectrum is important, because the shape is solar model independent and sensitive to neutrino oscillations, especially the

small angle solution of the MSW effect as described in Chapter 2. Fig 7.22 shows the ratio of data to SSM prediction in each energy bin. The statistics becomes large in Super-Kamiokande and the systematic errors have been reduced by LINAC calibration. Fig 7.22 also shows the expected energy shape if the typical small angle solution of MSW effect is assumed. ($\sin^2 2\theta = 9.12 \times 10^{-3}$ and $\Delta m^2 = 6.31 \times 10^{-6}$) It is hard to say that the spectrum distortion exists, but the small angle solution is more consistent with the measurement than a flat spectrum. ($\chi^2_{noosc}/\nu = 19.7/14, \chi^2_{MSW}/\nu = 18.7/14$) However it is not significant yet and more statistics is needed. Now, we also need further study the systematic error. The analysis will be very important in the future and we will discuss it in another paper.

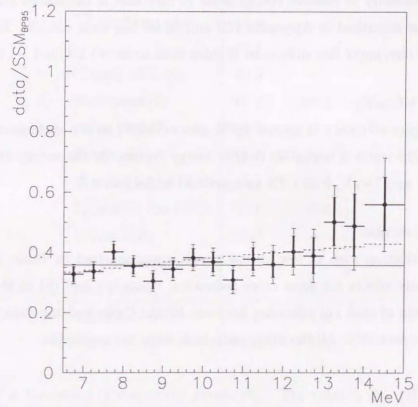

Figure 7.22: Energy spectrum observed in Super-Kamiokande. Inner and outer error bars shows the statistical and systematic errors, respectively. The dashed line shows the expected spectrum assuming the typical small angle solution of the MSW effect. ($\sin^2 2\theta = 9.12 \times 10^{-3}$ and $\Delta m^2 = 6.31 \times 10^{-6}$)

7.3.2 Summary of the systematic errors

The systematic errors for the solar neutrino analysis are summarized in Table 7.4.

- Energy scale and resolution.
  The systematic error of the absolute energy scale is ±1.5%. This is mainly caused by the variation in each LINAC energy point. (1.3% See Section 5.3) The energy resolution error, calculated by LINAC, is 4.7%. (See Section 5.3) The systematic error of solar neutrino flux caused by these errors is calculated to be +4.7% and −3.1%

  The uniformity of relative energy scale in direction is calculated using spallation events as described in Appendix C.2 and to be less than ±0.5%. The systematic error of day/night flux difference is calculated to be +1.2% and −1.1%

- Trigger efficiency.
  The trigger efficiency is almost 100% above 7MeV, so the systematic error of the trigger efficiency is negligible in this energy region. In the energy region between 6.5MeV and 7MeV, it is 1.2% as described in Section 4.6.

- Noise reduction.
  Each reduction step of low energy event is summarized in Table 7.2 The main systematic effects are from noise reduction, items (5) and (9) in the table. The differences of each cut efficiency between Monte Carlo and the data are 0.2% and 0.7%, respectively. All the other reduction steps are negligible.

- Direction.
  The difference of the angular resolution between Monte Carlo and the data is calculated by LINAC in Table 5.4. This difference is considered in the signal extraction.

- Vertex shift.
  As mentioned in Section 5.1, the systematic reconstructed vertex shift from the real point is 16cm at most. We estimated the systematic shift of the fiducial volume from the vertex shift. It is −1.3%.

- Calculation of ν-e cross section.
  The systematic error in the theoretical calculation of ν-e cross section to the solar neutrino flux is estimated to be 0.5% [34].

- Livetime calculation.
  Livetime is calculated by a few different methods, which use raw data, muon data or low energy data. The difference between these methods is 0.1% at most.

	Flux	Day/Night
Energy scale and	+4.7	+1.2
resolution	−3.1	−1.1
^{8}B spectrum error	+1.2	–
	−1.1	
Trigger efficiency	+0.2	–
Reduction (5)	±0.2	±0.1
Reduction (9)	±0.7	–
Direction	+1.7	–
Non-flat background	±0.1	±0.4
Spallation deadtime	<0.1	±0.6
Vertex shift	−1.3	–
ν-e cross section	±0.5	–
Live time	±0.1	±0.1
TOTAL	+5.2	+1.4
	−3.6	−1.3

Table 7.4: Summary of systematic errors (%). The total is the quadrature sum of the separate items. Currently, energy measurement and directional fitting errors dominate.

Chapter 8

Conclusions and Discussions

We have studied 297.4 days of the solar neutrino data measured in Super-Kamiokande. The observed ^{8}B solar neutrino flux,

$$2.42 \ {}^{+0.06}_{-0.06}(stat.) \ {}^{+0.13}_{-0.09}(sys.) \ [\times 10^6/cm^2/sec], \tag{8.1}$$

has small statistical ($\pm 2.5\%$) and systematic errors (${}^{+5.2\%}_{-3.6\%}$) which can be compared to those of Kamiokande results with error of $\pm 6.8\%$ (stat.) and $\pm 11.8\%$ (sys.)[20].

In this chapter, we discuss the implication of the results of the measurements of the absolute flux and of the separately measured daytime and night-time fluxes.

8.1 Implication of the absolute flux measurement

The comparison of the results in Super-Kamiokande to SSM

There are several different predicted values of solar neutrino flux as shown in Table 2.3. It was already shown that the fluxes of BP92 and TL93 were basically same when the input parameters were taken to be same[11]. The difference of BP95 with BP92 or TL93 is the inclusion of the effect of heavy element diffusion or not. It was shown that the sound speeds of the solar model which include the diffusion effect agree with helioseismological measurement with less than 0.2% discrepancy. It is better than the models not including diffusion effect (the discrepancy is less than 1%)[13].

The flux ratios of Super-Kamiokande to these models are summarized in Eq(7.16) $\sim$ (7.18). The ratio to BP95 which includes the diffusion of the heavy element and now

believed to be the best is,

$$\frac{Data}{SSM(BP95)} = 0.365 \ {}^{+0.010}_{-0.010}(stat.) \ {}^{+0.019}_{-0.013}(sys.). \tag{8.2}$$

This shows that the deficit is very significant (30σ) if only the experimental errors are taking into account. Careful examination on uncertainties of the solar neutrino flux calculations is indeed needed.

The standard solar models are constrained by the recent precise helioseismological measurement. Then we are able to build a solar model which is constrained by the measurement. For example, B.Ricci et al[54] calculated the solar core temperature (T) and its uncertainty in the helioseismologically-constrained solar model. This model used the same equations as SSM, and they calculated the range of allowed value of T by tuning input parameters (e.g. the radiative opacity, the ratio of heavy elements) to become consistent with helioseismological data. The central value of T calculated by them is 1.58×10^7 K, which is consistent with BP95 ($T = 1.57 \times 10^7$ K). Its uncertainty is $\Delta T/T = \pm 1.4\%$ and becomes smaller than that quoted error in BP95 ($\Delta T/T = \pm 2.7\%$). As a result, the uncertainty of the neutrino flux from the uncertainty of the solar core temperature becomes also smaller.

However, there are other sources of flux uncertainty, for example, the astrophysical S-factor, especially S_{17} for ^{8}B solar neutrinos. Recently, the new experiment of the cross section has been done[15] and it is discussed in Section 2.1. B.Ricci et al considered S_{17} has larger errors (30%) than that in SSM (9.3%). This large error corresponds to a 3σ uncertainty in S_{17}, which is $0.0224(1 \pm 0.093)$ (keV·barn)[14].

After all, the total uncertainties in solar neutrino flux calculation by them becomes larger than that in BP95. The lowest ^{8}B neutrino flux within their errors is $\phi(^8\mathrm{B}) = 2.97 \times 10^6$ (cm^{-2} sec^{-1}), (the central value is 5.96×10^6 (cm^{-2} sec^{-1})) which can be compared to 6.62×10^6 (cm^{-2} sec^{-1}) in BP95. The ratio of the data in Super-Kamiokande to the flux predicted by the lowest ^{8}B neutrino model is

$$\frac{Data}{Prediction} = 0.815 \ {}^{+0.020}_{-0.020}(stat.) \ {}^{+0.042}_{-0.029}(sys.). \tag{8.3}$$

As described above, the standard solar model is recently supported by helioseismology. However, since there are several parameters which are not entirely constrained by the helioseismology like the nuclear cross section, the neutrino production rate is still

on the debate. In order to avoid those argument we need the solar model independent analysis to solve the solar neutrino problem.

The comparison of the results in Super-Kamiokande to Homestake

We compared the results of Super-Kamiokande and Homestake. The sensitivity of solar neutrinos in each detectors is shown in Fig 8.1. From the calculation of the BP95, 1.94 SNU of ^{7}Be, pep and CNO solar neutrinos should be observed in Homestake in addition to the contribution of $2.69 \pm 0.07 \ {}^{+0.14}_{-0.10}$ SNU of ^{8}B solar neutrinos, corresponding value to the result of the measurement of Super-Kamiokande. (ref. Eq(8.1) and (8.2)) However, the observed value in Homestake was $2.54 \pm 0.14 \pm 0.14$ SNU, so there is a strong indication that other neutrinos especially ^{7}Be solar neutrinos are missing. ($\phi_{others} < 0.23$ SNU (90% C.L.))

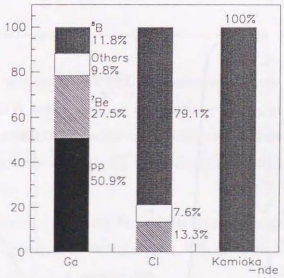

Figure 8.1: Individual solar neutrino contributions in various experiments, which is calculated by BP95.

If we assume the neutrino oscillation, the missing of ^{7}Be solar neutrinos can be naturally explained because of neutral current contribution to Super-Kamiokande data and/or non monotonic suppression of neutrinos. (See Fig 2.14)

Homestake experiment can detect only ν_e, while Super-Kamiokande can detect ν_μ and ν_τ through the neutral current interaction although the cross section is approximately

1/6 of ν_e. (See Fig 3.2) Therefore, if ν_e, generated in solar core, changes other type of neutrino by neutrino oscillation, it can be observed in Super-Kamiokande but not in Homestake. It makes as if the solar neutrino flux observed in Super-Kamiokande is larger than in Homestake.

When the typical value of oscillation parameters, for example, $\sin^2 2\theta = 1.1 \times 10^{-2}$ and $\Delta m^2 = 5 \times 10^{-6}$, are assumed, the expected flux observed in each detectors are non monotonic as shown in Fig 8.2 and calculated to be

$$\phi_{osc}^{SK} = 2.56 \times 10^6 (\mathrm{cm}^{-2}\mathrm{sec}^{-1}) = \begin{cases} \phi_{CC} = 1.81 \times 10^6 \\ \phi_{NC} = 0.75 \times 10^6 \end{cases}$$

$$\phi_{osc}^{Cl} = 2.34 \text{ SNU},$$

where ϕ_{CC} and ϕ_{NC} are expected flux from the charged current and the neutral current interaction, respectively. These are consistent with both two experimental results within the errors.

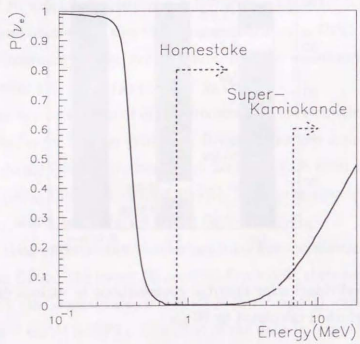

Figure 8.2: The survival probability of ν_e state by MSW effect as a function of Energy, when $\sin^2 2\theta = 1.1 \times 10^{-2}$ and $\Delta m^2 = 5 \times 10^{-6}$. The threshold energy of Super-Kamiokande and Homestake are also shown.

Summary

The absolute solar neutrino flux observed in Super-Kamiokande is significantly smaller than the expected flux from SSMs, and the experimental errors become particularly small. Even though the theoretical uncertainty is considered to be still large, this results suggests the neutrino oscillation. The comparison with the result in Homestake are consistent with a hypothesis of neutrino oscillation.

8.2 Neutrino oscillation study using day-night flux difference

Introduction

In this section, we will study the flux measured separately for daytime and night-time in detail. The MSW effect through the earth – the ν_e regeneration described in Section 2.4.3 create flux difference between day and night. If we take the ratio of night-time flux to daytime flux, the analysis for neutrino oscillations becomes independent on solar model calculations.

With the current statistics the total flux of daytime and night-time agree within the experimental errors as described in Section 7.3.1. We are able to evaluate the excluded regions of the neutrino oscillation parameters.

We have divided the night-time into five bins in terms of the angle (δ_{sun}) between the sun and the Z-axis of the detector as shown in the next page. We call each bin as N1, N2, N3, N4, and N5 ($\Delta \cos\delta_{sun} = 0.2$). By using this division, we are able to make a sensitive check on the MSW effect which depend on the distance through the earth and the different electron density. Table 8.1 and Fig 8.3 shows the solar neutrino flux in the daytime and the five night-time bins. Fig 8.3 also shows the expected solar neutrino flux in each bin for the two typical MSW parameters, corresponding to large and small angle regions. In the large angle region, the flux difference of daytime and average night-time is larger than in small angle region.

all	$2.42^{+0.06}_{-0.06}$	
day	$2.39^{+0.09}_{-0.09}$	
night	$2.44^{+0.09}_{-0.08}$	
N1	$2.52^{+0.22}_{-0.22}$	
N2	$2.17^{+0.20}_{-0.19}$	Combined
N3	$2.53^{+0.18}_{-0.17}$	$2.42^{+0.10}_{-0.09}$
N4	$2.51^{+0.20}_{-0.20}$	
N5	$2.61^{+0.21}_{-0.21}$	

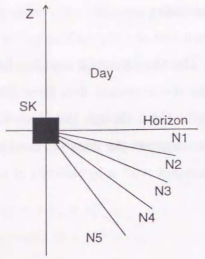

Table 8.1: The solar neutrino flux in the daytime, the five night-time bins and the combined value between N1 and N4. The definition of them are also shown.

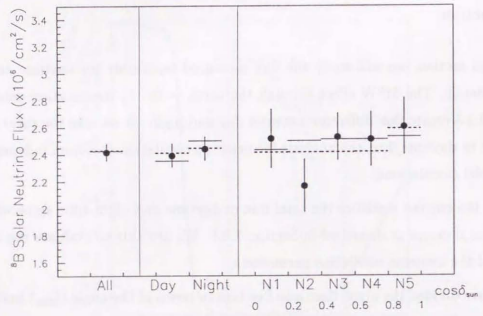

Figure 8.3: The solar neutrino flux in the daytime and the five night-time bins observed in Super-Kamiokande. The expected solar neutrino flux in each day-night bin for the two typical MSW parameters are also shown. The solid line shows $\sin^2 2\theta = 0.631$ and $\Delta m^2 = 3.16 \times 10^{-5}$. The dashed line shows $\sin^2 2\theta = 6.31 \times 10^{-3}$ and $\Delta m^2 = 6.92 \times 10^{-6}$.

The calculation method

For the analysis of MSW effect, the expected number of solar neutrinos for the various neutrino oscillation parameters, $(\sin^2 2\theta, \Delta m^2)$ were calculated, and compared with those for no MSW effect. The parameter regions considered were $10^{-4} \leq \sin^2 2\theta \leq 1, 10^{-7.5} \leq \Delta m^2 \leq 10^{-3.5}$, and the 201×81 points uniformly distributed are picked up from the region for the calculation.

The generated position of neutrinos is shown in Fig 2.2 [10], and the propagation of neutrinos through the sun was calculated by the numerical integration of Eq(2.23) from the center to the surface of the sun. The electron density used in this calculation is shown in Fig 2.1[10]. From the surface of the sun to the earth, the neutrinos follow the equation of the vacuum oscillation in Eq(2.18). The neutrino propagation in the earth was calculated by the similar way in the case of the sun. The electron density used was shown in Fig 2.15[31].

In order to obtain the confidence level contours for the day-night effect, the following χ^2 is defined:

$$\chi^2 = \sum_{i=1}^{6} \frac{(R_i - R_i^{MSW} \times \alpha)^2}{\sigma_i^2}, \tag{8.4}$$

where i runs each bin of daytime and five night-time divisions. R_i is the ratio of the data to SSM in i-th day-night bin and R_i^{MSW} is the expected ratio between those with and without MSW effect. σ_i is the quadratic sum of the statistical error of R_i and the systematic error of day/night flux shown in Table 7.4. α is the normalization factor which is free and determined so as to give a minimum χ^2.

The calculation results and discussion

Fig 8.4 shows the contour of the 95% C.L.. The inside region is excluded from the result for Super-Kamiokande. This figure also shows the result for Kamiokande. As can be clearly seen, Super-Kamiokande extended the excluded region of the Kamiokande.

As described in Section 2.4.4, if we assume a absolute flux predicted from a solar model, we can obtain the allowed parameter region of the MSW effect. In Fig 8.4 we also show the allowed region from this kind of analysis for all the past four solar neutrino experiment results assuming BP95. We can exclude about half of the large angle solution from the result of only 297 days of the day-night flux in Super-Kamiokande.

Fig 8.4 also shows the exclude region if the flux difference in daytime and night-time does not exist in 2 years and 5 years statistics. We can sense all the parameter region in large angle solutions in 5 years.

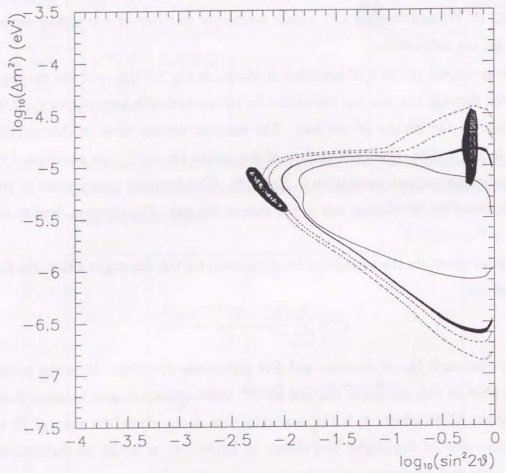

Figure 8.4: The 95% C.L. contour of the MSW analysis. The inside region of a thick line is excluded from the result of day/night flux variation in Super-Kamiokande. This figure also shows the excluded region from the day/night flux variation in Kamiokande (a thin line) and the allowed region from the current solar neutrino experiments. (See Section 2.4) The dashed lines show the exclude region expected from 2 years (inside) and 5 years (outside) statistics.

The study of earth core effect in MSW analysis

As shown in Fig 8.3, the study on the day-night effect is not sensitive to the small angle solution except the N5 bin, because this bin is corresponding to the high density of core in the earth. The boundary between core and mantle is 3480km deep in the earth, and $\cos\delta_{sun} = 0.8376$. Therefore, neutrinos in N1 to N4 go through only mantle, while neutrinos in N5 go through both core and mantle. It is pointed out by Petkov et al[55] that the small angle region can be precisely studied by the analysis of this core effect. We separately consider the solar neutrino flux combined from N1 to N4 term (Mantle term) and N5 term (Core term) in order to see clearly the core effect. We define the following parameters;

$$A^N = \frac{Day - Night}{Day + Night},$$
$$A^M = \frac{Day - Mantle}{Day + Mantle},$$
$$A^C = \frac{Day - Core}{Day + Core}.$$

Table 8.2 shows the expected value for typical two couple of MSW parameters. In small angle region, the difference between A^M and A^C becomes large as shown in the table.

	$\sin^2 2\theta$	Δm^2	A^N	A^M	A^C	$\frac{A^C}{A^M}$
1	0.631	3.16×10^{-5}	-0.0307	-0.0294	-0.0370	1.26
2	6.31×10^{-3}	6.92×10^{-6}	-0.00725	-0.00108	-0.0356	32.96

Table 8.2: The asymmetry defined in the text.

Fig 8.5 and Table 8.1 shows the experimental results in Super-Kamiokande. The asymmetries are

$$A^N = -0.0104 \pm 0.0258(stat.) \pm 0.0135(sys.),$$
$$A^M = -0.0069 \pm 0.0273(stat.) \pm 0.0135(sys.),$$
$$A^C = -0.0432 \pm 0.0443(stat.) \pm 0.0135(sys.).$$

Fig 8.5 also shows calculate value for the typical MSW parameters in large angle and small angle region. From the figure, small angle solution seems good, ($\chi^2_{large}/\nu = 1.32/4, \chi^2_{small}/\nu = 0.076/4$) but it is not conclusive yet, and need more statistics.

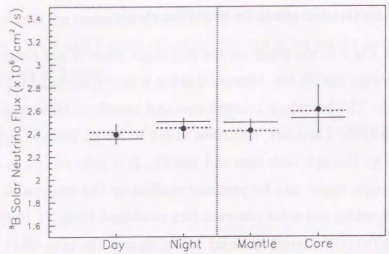

Figure 8.5: The observed flux in each time region in Super-Kamiokande. The expected flux assuming the typical MSW parameters as described in Table 8.2. The solid line shows the large angle and the dashed line shows the small angle region.

8.3 Summary

We summarize the results and the implication of solar neutrino flux observation in Super-Kamiokande.

1. We have measured solar neutrinos in Super-Kamiokande. The deficit of the observed flux from the predicted by SSMs was seen, and the ratio is

$$\frac{Data}{SSM(BP95)} = 0.365^{+0.010}_{-0.010}(stat.)^{+0.019}_{-0.013}(sys.).$$

   The significance of ^{8}B neutrino flux deficit in Super-Kamiokande is stronger than the result in Kamiokande because the statistics and the quality of the data were improved.

2. The results of Super-Kamiokande and Homestake are difficult to be explained by changing solar models but are natural by neutrino oscillation.

3. The flux of daytime and night-time agree within the experimental errors. From the result of day-night flux measurement, we calculated the excluded regions of the neutrino oscillation parameters of MSW effect. It also restricts the large angle solutions obtained from the combined results of solar neutrino flux in the past experiments assuming the absolute flux.

4. By considering future increases of statistics, we can extend on sensitivity in the entire large angle solution.

5. The analysis of the core effect in the earth is sensitive to the small angle solutions. The result of core effect in Super-Kamiokande suggests that the small angle solution is better than the large angle solution, but it is not conclusive yet.

In the MSW analysis, the analysis of day-night flux difference is sensitive to the large angle solutions, and the small angle solutions if the core effect in the earth is considered. The energy shape is sensitive to the small angle solutions. These analyses are complementary. Further, the analysis of the seasonal flux variation is sensitive to the vacuum oscillation. Therefore, when the statistics become larger and the analysis is more precise in future, we can conclude the neutrino oscillation definitely.

Appendix A

Electronics

In this chapter the electronics in Super-Kamiokande is described in detail. The electronics for the inner detector consists of TKO(TRISTAN/KEK Online) modules[56] and VME modules. The logic diagram of the electronics system is shown in Fig A.1. These are arranged in 4 separate electronics huts, each with 12 TKO system crates and 2 VME crates, for a total of 48 and 8 crates, respectively.

The front-end electronics uses 934 modules called "ATM" (Analog Timing Module) which process the signals from the PMTs. In general 20 ATM modules are arranged in an each TKO crate. Each crate also contains one interface module called "SCH" (Super Control Header), one trigger signal distribution module called "GONG" (GO/NoGo), and one summing circuit. In the VME crates, there are 6 data buffer modules called "SMP" (Super Memory Partner) and one SBus-VME Interface.

Fig A.2 shows the block diagram of the circuit in the ATM. First, each ATM handles 12 PMT channels, and a signal from each PMT is divided into four. One of these four, after amplification by a factor of 100, goes through a discriminator the threshold of which is set to 100mV, equivalent to about 0.32 p.e.. When the pulse height of a PMT signal exceeds this threshold,a rectangular pulse (200nsec in width and 11 mV in height) is generated. The pulses from each 12 PMT channels are summed and output as the "HITSUM" signal. A rectangular pulse with 900nsec duration is generated as a HIT signal simultaneously. For this 900nsec, any subsequent PMT signal is rejected. This discriminator pulse starts the charging of "TAC" (time-to-analog converter), and it will end when the global trigger signal arrives. Another signal from the PMT is sent to the "QAC" (charge-to-analog converter) which accumulates charge for 400nsec after each

discriminator hit. If the global trigger does not arrive within 1.3μsec after the PMT hit, the TAC/QAC are flushed. While the global trigger arrives, an ADC begins digitizing the voltages stored in the TAC/QAC capacitors. The ADC outputs are stored in the 1024 word "FIFO"(first-in first-out) memory with event number. It spends 5.5μsec to do Analog-Digital conversion and store into memory, and the signal is not processed in this period. Therefore, the TAC/QAC has 2 channels, so that if the one is not available, the other channel can be used instead. This reduces the dead time, which is especially useful for observation of the decay electron signal from stopping muons. The timing chart of signals in the ATM is shown in Fig A.3.

Pedestals for ATMs are measured every 30 minutes. This takes about 1 minute. In order to reduce dead time for our super nova search, pedestal data taking is done for 1/8 of all the ATM, and normal data taking is operated to the remaining ATM. For solar neutrino analysis, data taking is dead during all pedestal measurements.

The trigger condition was already described in Section 3.2.4. The trigger signal is fed to the "TRG" module. This module has a 16 bit event counter, and an internal clock which runs at 50 MHz, so the relative time of the event is determined with 20nsec resolution. This event information is stored in the FIFO memory of the TRG module. The global trigger signal and event counter is distributed to 48 GONG modules in each TKO crate. GONG modules distribute the trigger signal and event counter to the ATM modules. The timing chart of the trigger is also shown in Fig A.3.

Data acquisition system and Offline computer facilities

The 20 ATM data are read out via SCH to the SMP (VME module), and stored in it. The data stored in SMP are sent via SBus-VME Interface to the online computer. In each electronics hut, there are two Sun SPARClassic (S4/CL) for inner data acquisition (total 8), and each S4/CL reads out and collects the data of 6 SMP modules. This is shown in Fig A.1. These data are transferred to a Sun SPARCstation 10 (S4/10) as a online host computer via FDDI which is a network for transferring data at very high speed. After the data format is changed in the reformat machine (S4/CL, described below), they are sent to the offline computer which is outside of the mine via an optical fiber cable.

In the online host computer (S4/10), all the information of hit PMTs including inner

and outer detector belonging to one global trigger is concatenated and recorded. This is regarded as one event. Next, the format of this data is changed to "ZEBRA" format, by what we call the "reformat" process. ZEBRA is a tool for data management which is developed in CERN which we use because it is convenient for storage and handling of large quantities of data, and it is also standard in high-energy physics experiment. After reformat, the ZEBRA format data is sent to offline host computer (VPX210/10S) every ten minutes. The size of this file corresponding to ten minutes is about 70MByte. This host computer saves all the data in a tape library and converts the data of ADC and TDC counts to units of photo electron and nano second, respectively. These data are stored in buffers on 1GByte memory temporarily, and distribute to SPARCstation 20 (S4/20), with a total of 20 CPUs connected by the network called "UltraNet1000". In these machines, all events are reconstructed by various algorithms for different energy ranges. There are also 10 work stations for analysis (S4/10) with 2 CPU in each machine, connected via FDDI to VPX210/10S and S4/20.

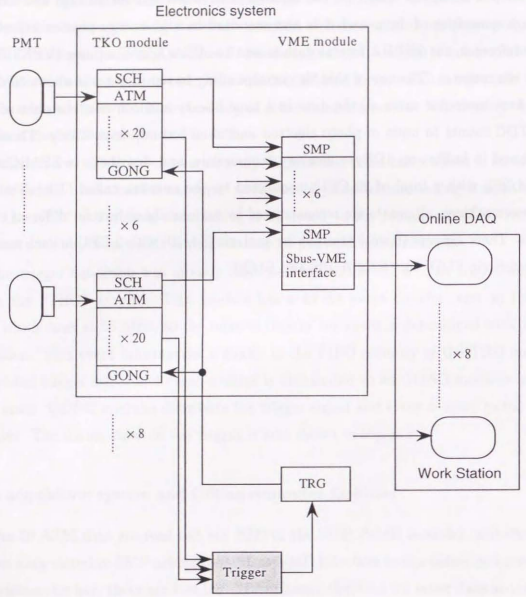

Figure A.1: The logic diagram of the electronics system used in Super-Kamiokande.

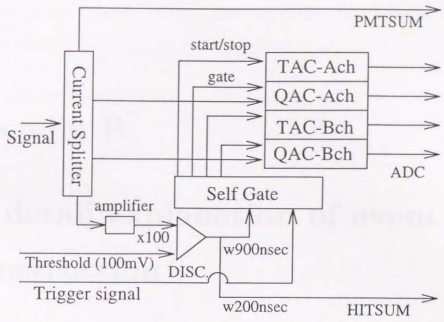

Figure A.2: The ATM block diagram.

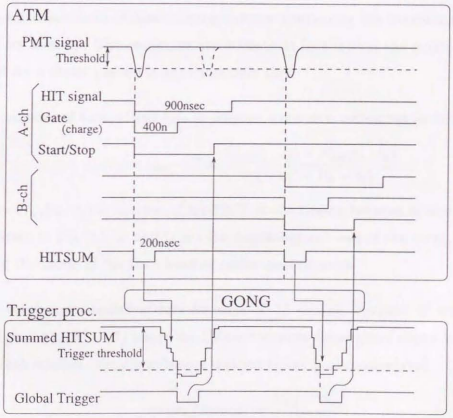

Figure A.3: The timing chart for signal and trigger.